Development and application of semi-empirical interatomic potentials to study interface faceting and fracture

Md. Masud Alam

Development and application of semi-empirical interatomic potentials to study interface faceting and fracture

Dissertation
zur Erlangung des akademischen Grades
Doktor der Naturwissenschaften (Dr. rer. nat.)
vorgelegt dem
Department Physik der Fakultät für Naturwissenschaften
an der Universität Paderborn

Md. Masud Alam

Promotionskommission

Chairperson	Prof. Dr. Jörg Lindner
Referee	Prof. Dr. Jörg Neugebauer
Referee	Prof. Dr. Wolf Gero Schmidt
Member	Dr. Matthias Reichelt

Tag der Einreichung: 16 May, 2022

Tag der Verteidigung: 30 Aug, 2022

Abstract

Development and application of semi-empirical interatomic potentials to study interface faceting and fracture

Interfaces have a strong impact on the properties of materials. These include optoelectronic and mechanical properties. Multi- (mc-) and poly-crystalline Silicon is a prototype system that demonstrates the importance of interfaces, such as grain boundaries (GBs), on the material's electronic properties as well their technological implications. GBs as well as their interaction with impurities are one of the major limiting factors of the efficiency of mc-Si based solar cell devices. As the interface over volume ratio increases, such as in nano-crystalline materials, interfaces and interface faceting and reconstruction get an even more central role in the stage of materials' properties. In this case, these properties are governed by a complex interplay between microstructure, facet and impurity segregation energies, and long-range strain interactions.

In structural materials, surfaces and interfaces control materials' strength and fracture. For example, the energy release rate by the formation of an extra free surface upon crack propagation is a decisive parameter that controls brittle fracture. Likewise the electronic properties, impurities have a strong impact on the mechanical properties as well. The *rhenium effect* can be considered as a characteristic example that highlights the aforementioned: Creep and fatigue properties of Ni-based superalloys are considerably improved by the addition of a few wt% Re. However, a deep understanding of this effect is still under debate.

With the rapid increase in computational power, atomistic simulations have become an indispensable tool to investigate and understand the properties of materials. These calculations can provide insight and an on-atomic-scale understanding of the mechanisms underlying the materials' properties and information that is not straightforwardly accessible by experiment. However, a common characteristic of the mechanisms underlying, grain boundary reconstructions, nano-faceting, and fracture is that they span a wide range of length scales: From bond bending, stretching, and breaking at the nm scale to dislocation nucleation and strain field interaction in the sub-μm scale.

First principle calculations can accurately describe the aforementioned phenomena at all relevant length scales. However, they are restricted by the available computational power, to systems consisting of a few thousand atoms. Nevertheless, to describe faceting at the experimentally relevant length scale or fracture through crack propagation supercells consisting of ten or hundred thousand atoms are required. Semi-empirical interatomic potentials on the other hand can be regularly employed in large-scale atomistic simulations. However, a challenge and a prerequisite to employing semi-empirical interatomic potentials is their transferability, i.e., their ability to quantitatively or qualitatively describe the interatomic interactions in a wide range of different environments.

In the present thesis, second nearest-neighbor modified embedded atom method (2NN-MEAM) potentials have been developed to describe (i) GBs and GB faceting in Si, (ii) topology and strain effects in impurities segregation at facet junctions in Si, and (iii) fracture in low Re content $\mathrm{Ni}_{1-x}\mathrm{Re}_x$ alloys. In order to parametrize and evaluate these potentials, a software tool called "Potitr" has been developed, and first principle calculations within the density functional theory (DFT) have been employed.

Employing these newly developed potentials the energetics, structure, and strain of flat and faceted $\Sigma3$ tilt GBs in Si with the $\langle 110 \rangle$ rotation axis have been investigated. These GBs constitute up to 80% of GBs in Si and hence they are a system of GBs with special fundamental and technological interest. Based on these, a phase diagram has been constructed which indicates the energetically most favorable facet and line junction reconstructions as a function of the facet length and inclination angle. This diagram reveals that faceting is intrinsic to these GBs' family and the properties of the faceted GBs are controlled by the interplay between GB energies and long-range strain interactions. Moreover, it demonstrates that higher energy GBs can be stabilized by thermodynamics rather than kinetics when these constitute facets at line junctions. Therefore, it highlights the crucial role of microstructure such as the grain size on the GB properties.

Next, we focus on the interaction of faceted $\Sigma3$ GBs in Si with C. C is homovalent to Si, i.e., its interactions with the planar and line defects are predominantly induced by strain. Hence, strain and electronic effects underlying these interactions can be decoupled. In agreement with recent experimental evidence, we find strong asymmetric line segregation of C at only one of the two junctions at $\Sigma3$ faceted GBs in Si. Inspection of the strain

field around the line junctions revealed the presence of partial edge type dislocations of opposite Burgers vectors at the two line junctions. Hence, the facet junctions are accompanied by regions of tensile and compressive strain. These insights demonstrate that the origin of the aforementioned novel segregation behavior is the local differences in the atomic geometry at the cores of the line junctions and the presence of tensile and compressive regions around the latter. Furthermore, they highlight the role of interface and line junction topology on the segregation mechanisms.

In the last part of the thesis, mode I fracture in Ni and low Re content $\mathrm{Ni}_{1-x}\mathrm{Re}_x$ alloys has been investigated. The investigations involved both linear elastic fracture mechanics as well as large scale atomistic fracture calculations of crack propagation in the $\langle 112 \rangle / \{111\}$ fcc slip system. These calculations revealed that the $[1\bar{1}2]/(1\bar{1}\bar{1})$ crack system has the lowest critical stress intensity factor. Moreover, they demonstrated a ductile fracture, i.e., crack propagation through the nucleation and emission of dislocations. The fracture remained ductile after the addition of Re with contents that did exceed a few at.%. However, in agreement with the aforementioned rhenium effect, it was found that Re increases the critical stress intensity factor.

In summary, 2NN-MEAM potentials for Si, C, SiC, Ni, Re, and NiRe have been developed. Employing these potentials, interfaces, and C segregation at line junctions in Si and fracture in Ni and $\mathrm{Ni}_{1-x}\mathrm{Re}_x$ alloys have been investigated. These works successfully address hitherto open questions and provide new insights on the mechanisms governing GB faceting and segregation.

This thesis has been done in the Computational Materials Design Department of the Max-Planck-Institut für Eisenforschung GmbH and part of the work has been motivated by and conducted in collaboration with experimental groups from the same Institute.

Zusammenfassung

Grenzflächen haben einen starken Einfluss auf die Eigenschaften von Materialien. Dazu gehören optoelektronische und mechanische Eigenschaften. Multi- (mc-) und polykristallines Silizium ist ein Prototypsystem, das die Bedeutung von Grenzflächen wie Korngrenzen (GBs) für die elektronischen Eigenschaften des Materials sowie deren technologische Implikationen demonstriert. GBs sowie ihre Wechselwirkung mit Verunreinigungen sind einer der Hauptbegrenzungsfaktoren der Effizienz von Solarzellenvorrichtungen auf mc-Si-Basis.

Wenn das Verhältnis von Grenzfläche zu Volumen zunimmt, wie z. B. in nanokristallinen Materialien, erhalten Grenzflächen und Grenzflächenfacettierung und -rekonstruktion eine noch zentralere Rolle im Zustand der Materialeigenschaften. In diesem Fall werden diese Eigenschaften durch ein komplexes Zusammenspiel zwischen Mikrostruktur, Facetten- und Verunreinigungssegregationsenergien und langreichweitigen Dehnungswechselwirkungen bestimmt.

Bei Strukturmaterialien steuern Oberflächen und Grenzflächen die Festigkeit und den Bruch der Materialien. Beispielsweise ist die Geschwindigkeit der Energiefreisetzung aufgrund der Bildung einer zusätzlichen freien Oberfläche während der Rissausbreitung ein entscheidender Parameter, der den Sprödbruch steuert. Ebenso wie die elektronischen Eigenschaften haben auch Verunreinigungen einen starken Einfluss auf die mechanischen Eigenschaften. Der *Rhenium-Effekt* kann als ein charakteristisches Beispiel betrachtet werden, das das zuvor Genannte betont: Kriechen und Die Ermüdungseigenschaften von Superlegierungen auf Ni-Basis werden durch die Zugabe von einigen Gew.-% Re deutlich verbessert. Ein gründliches Verständnis dieses Effekts wird jedoch noch diskutiert.

Mit dem schnellen Anstieg der Rechenleistung sind atomistische Simulationen von Materialien zu einem unverzichtbaren Werkzeug geworden, um die Eigenschaften von Materialien zu untersuchen und zu verstehen. Diese Berechnungen können Einblicke und ein Verständnis auf atomarer Ebene liefern der Mechanismen, die den Materialeigenschaften zugrunde liegen, und sie können Informationen liefern, die experimentell nicht ohne weiteres zugänglich sind. Ein gemeinsames Merkmal der Mechanismen, die Korngrenzenrekonstruktionen, Nanofacettierung und Bruch zugrunde liegen, ist jedoch, dass sie einen weiten Bereich von Längenskalen abdecken: von

Bindungsbiegung, -dehnung und -bruch auf der nm-Skala bis hin zu Versetzungskeimbildung und Spannungsfeldwechselwirkung in der Sub-μm-Skala.

First-Principle-Rechnungen können die oben genannten Phänomene auf allen relevanten Längenskalen genau beschreiben. Allerdings sind sie durch die verfügbare Rechenleistung auf Systeme beschränkt, die aus einigen tausend Atomen bestehen. Um dennoch Facettierung auf der experimentell relevanten Längenskala oder Bruch durch Rissausbreitung zu beschreiben, bestehen Superzellen aus zehn- oder hunderttausend Atomen. Semi-empirische interatomare Potentiale hingegen können regelmäßig in atomistischen Simulationen im großen Maßstab verwendet werden. Eine Herausforderung und Voraussetzung für den Einsatz halbempirischer interatomarer Potentiale ist jedoch ihre Übertragbarkeit, d. h. ihre Fähigkeit, die interatomaren Wechselwirkungen in einer Vielzahl unterschiedlicher Umgebungen quantitativ oder qualitativ genau zu beschreiben.

In der vorliegenden Dissertation wurden Potenziale der Second-Next-Neighbour-Modified-Embedded-Atom-Methode (2NN-MEAM) entwickelt, um (i) GBs und GB-Facettierung in Si, (ii) Topologie und Spannungseffekte bei der Segregation von Verunreinigungen an Facettenübergängen in Si und zu beschreiben (iii) Bruch in $\mathrm{Ni}_{1-x}\mathrm{Re}_x$-Legierungen mit niedrigem Re-Gehalt. Um diese Potentiale zu parametrisieren und auszuwerten, wurde ein Softwaretool namens "Potitr" entwickelt und erste prinzipielle Berechnungen innerhalb der Dichtefunktionaltheorie (DFT) durchgeführt.

Unter Verwendung dieser neu entwickelten Potentiale wurden die Energetik, Struktur und Dehnung von flachen und facettierten GBs mit $\Sigma 3$-Neigung in Si mit der Rotationsachse $\langle 110 \rangle$ untersucht. Diese GBs machen bis zu 80daher sind sie ein System von GBs mit besonderem fundamentalem und technologischem Interesse. Darauf aufbauend wurde ein Phasendiagramm konstruiert, das die energetisch günstigste Facetten- und Linienübergangsrekonstruktionen in Abhängigkeit von Facettenlänge und Neigungswinkel. Dieses Diagramm zeigt, dass die Facettierung der Familie dieser GBs eigen ist und Die Eigenschaften der facettierten GBs werden durch das Zusammenspiel zwischen GB-Energien und langreichweitigen Dehnungswechselwirkungen gesteuert. Darüber hinaus zeigt es diese höhere Energie GBs können eher durch Thermodynamik als durch Kinetik stabilisiert werden, wenn diese Facetten an Linienübergängen bilden. Daher wird die entscheidende Rolle der Mikrostruktur wie der Korngröße für die GB-Eigenschaften hervorgehoben.

Als nächstes konzentrieren wir uns auf die Wechselwirkung von facettierten

$\Sigma 3$ GBs in Si mit dem Kohlenstoff. Kohlenstoff ist zu Si homovalent, d. h. seine Wechselwirkungen mit den Planar- und Liniendefekten werden überwiegend durch Dehnung induziert. Daher können Dehnungs- und elektronische Effekte, die diesen Wechselwirkungen zugrunde liegen, entkoppelt werden. In Übereinstimmung mit neueren experimentellen Befunden finden wir eine starke asymmetrische Linienseigerung von C nur an einem der beiden Übergänge bei $\Sigma 3$ facettierten GBs in Si. Die Untersuchung des Dehnungsfeldes um die Linienübergänge herum zeigte das Vorhandensein von partiellen Kantenversetzungen von entgegengesetzten Burgers-Vektoren an den beiden Linienübergängen. Daher werden die Facettenverbindungen von Zug- und Zugbereichen begleitet Druckbelastung. Diese Erkenntnisse zeigen, dass der Ursprung des zuvor erwähnten neuartigen Segregationsverhaltens die lokalen Unterschiede in der atomaren Geometrie an den Kernen der Linienübergänge und das Vorhandensein von Zug- und Druckregionen um letztere herum sind. Darüber hinaus heben sie die Rolle der Schnittstellen- und Leitungsübergangstopologie für die Segregationsmechanismen hervor.

Im letzten Teil der Arbeit wurde der Modus-I-Bruch in Ni- und $\mathrm{Ni}_{1-x}\mathrm{Re}_x$-Legierungen mit niedrigem Re-Gehalt untersucht. Die Untersuchungen umfassten sowohl lineare elastische Bruchmechanik als auch großmaßstäbliche atomare Bruchberechnungen der Rissausbreitung im $\langle 112 \rangle / \{111\}$ fcc-Gleitsystem. Diese Berechnungen ergaben, dass das Risssystem $[1\bar{1}2]/(1\bar{1}\bar{1})$ den niedrigsten kritischen Spannungsintensitätsfaktor aufweist . Darüber hinaus zeigten sie einen duktilen Bruch, d. h. eine Rissausbreitung durch Keimbildung und Emission von Versetzungen. Der Bruch blieb duktil nach der Zugabe von Re mit Gehalten, die einige at.% überstiegen. In Übereinstimmung mit dem oben erwähnten Rheniumeffekt wurde jedoch gefunden, dass Re den kritischen Spannungsintensitätsfaktor erhöht.

Zusammenfassend wurden 2NN-MEAM-Potentiale für Si, C, SiC, Ni, Re und NiRe entwickelt. Unter Verwendung dieser Potentiale wurden Grenzflächen und C-Seigerung an Linienübergängen in Si und Bruch in Ni- und $\mathrm{Ni}_{1-x}\mathrm{Re}_x$-Legierungen untersucht. Diese Arbeiten adressieren erfolgreich bisher offene Fragen und liefern neue Einblicke in die Mechanismen, die GB-Facettierung und -Segregation steuern. Diese arbeit wurde in der Abteilung Computational Materials Design des Max-Planck-Instituts für Eisenforschung GmbH durchgeführt und ein Teil der Arbeit wurde von experimentellen Gruppen desselben Instituts motiviert und in Zusammenarbeit mit ihnen durchgeführt.

Acknowledgements

Directly, indirectly there are lots of minds involved with this thesis, without whom, I could never be in such a position. I am grateful to all those people and would like to show my gratitude from my deepest heart.

The foremost name that comes to my mind is Prof. Dr. Jörg Neugebauer. I am thankful to him for giving me the opportunity to work in such a world-renowned place. This institute is known as one of the best places of its kind, and I am really privileged to have such an opportunity. Furthermore, his time to time guidance through semiconductor meeting discussions was of immense help. Apart from the scientific guidance, his greatness in transferring my scholarship to a job contract will be remembered.

Secondly, I am in debt to my direct supervisor and group leader of the growth modeling group, Dr. Liverios Lymperakis, without whom I could never finish my thesis. He was exemplary by giving me time for discussion almost every day. A special thanks to him for giving me access to his office anytime I wanted. His hearty guidance, mentoring helped me to overcome a lot of obstacles during my work at MPIE. Furthermore, I learn the way of doing research properly from him, which helped me to solve a problem faster than before I joined the MPIE.

I am in debt to all my teachers I met from class one to till my PhD, but some names I should mention here. The guidance, love of Prof. Dr. Jens Kortus from TU Bergakademie, Freiberg is special. Without his direct supervision, advice, guidance, love I won't be in such a position today. The description of his love cannot be finished in two lines. I am further thankful to my other teacher Dr. Sébastien Groh who supported me both in scientific and non-scientific issues since my first day in Germany.

A special thanks to my wife Nusrat Jahan for her care and love in the

course of my PhD research. Her patience is really appreciable when I made her bored by working and talking about my work all the time. Special love to my loving son Muntahin, whose born has changed my attitude towards life and its ever-changing. I am in debt to my parents for their sacrifice and support. Without their encouragement, support, love I won't be at this stage.

Finally, I would like to acknowledge the financial support of Max-Planck-Society for conducting the research.

Contents

Chapter 1

Introduction

Interfaces, such as grain boundaries (GBs), constitute a family of extended defects with a dominant role in the properties of materials. In optoelectronic materials, GBs may contain broken and/or highly bent or stretched bonds. These introduce swallow or deep states in the fundamental band gap which act as recombination centers and reduce the device's efficiency. The efficiency of the devices is also strongly affected by the segregation of impurities at GBs. Nevertheless, segregation of impurities at GBs is not only of immediate technological importance due to e.g., the deep intergap states the former may introduce or their effect on GB mobility and cohesion. Segregation of impurities is also strongly connected with the thermodynamics of the interfacial states, often called complexions, a field of materials research that has been rapidly developed in recent years [1].

The situation of impurity-containing interfaces phases becomes puzzling when faceting and line junctions are considered. Line junctions can be considered as 1D extended defects, per se. Indeed as it will be demonstrated in Chapter 4, line junctions at $\Sigma 3$ GBs in Si pose a character of partial edge type dislocations. These dislocations have a core region and a long-range strain field and both have a strong impact on impurities segregation. Nevertheless, the density of the line junctions is related to the microstructure in terms of grain size: Fine grains reduce the faceting length and hence increase the density of these 1D interfacial defects.

In structural materials, GBs and the grain size play an important role in strength via the Hall–Petch relation [2–4]: The materials yield strength is inverse proportional to the square root of the average grain diameter. However, for diameters smaller than a few tens of nm, due to the onset of GB sliding the material gets softer with the decreasing grain size (inverse Hall-Petch effect) [4]. The mechanical properties of materials are also strongly affected by the impurities segregation and precipitation at interfaces. Segregated impurities may weaken cohesion at GBs and result in the so-called solute induced embrittlement [5, 6].

Apart from interfaces, surfaces and dislocations and their interaction with impurities have a strong impact on the mechanical properties as well: In fracture through crack propagation the critical stress intensity factor, which describes the material's strength, depends on (i) the nucleation and emission of dislocations which is related to the stacking fault energies and (ii) the surface energy release rate caused by the crack propagation. These control the nature of the fracture, i.e., ductile vs brittle, as well. Therefore, surface and generalized stacking fault energies are also key material parameters.

1.1 The need for interatomic potentials

A common characteristic of the aforementioned phenomena, i.e., interface reconstructions, GB faceting, impurity segregation, and fracture, is that the underlying mechanisms span a wide range of length scales. e.g., bond breaking is taking place at the nm scale, while elastic strain interactions are at the μm scale. Atomistic calculations which are based on the interactions between the smallest structural units in condensed matter, i.e., the atoms, can provide insights into the mechanisms underlying the materials' properties and information that is not straightforwardly accessible by experiment.

First principles calculations nowadays constitute the working horse in computational solid-state research and are well established for describing many-body systems at the quantum mechanical level. Although they have been successfully and extensively used to study a vast variety of systems and properties, they are still suffering from the available computational power.

Systematic and regular investigations by employing *ab-initio* calculations are limited to systems consisting of a few thousand atoms. However, this is at least an order of magnitude smaller than the system sizes necessary to capture and investigate the aforementioned phenomena.

Semi-empirical interatomic potentials have been developed and have been regularly employed in large-scale atomistic simulations. Therefore, they emerge as an alternative route that can address the small system size challenge. To get an understanding of these models, let us first focus on one of the oldest and simplest interatomic potentials, the Lennard–Jones (LJ) potential. The LJ potential includes pair interactions and the energy of a system is written as:

$$V_{LJ}\left(r_{ij}\right) = 4\epsilon\left[\left(\frac{\sigma}{r_{ij}}\right)^{12} - \left(\frac{\sigma}{r_{ij}}\right)^{6}\right] \tag{1.1}$$

here, ϵ is a constant equal to the binding energy at the equilibrium distance σ. r_{ij} is the distance between the atoms i and j. As it is apparent from the simple form of Eq. (1.1), the LJ potential is an approximation based on a crude assumption: The atoms are considered as balls and their interactions depend on the interatomic distances alone, while the crucial role of electrons is not explicitly considered. Nevertheless, this assumption is not completely arbitrary. The Born-Oppenheimer approximation, i.e., the motions of nuclei and electrons can be decoupled, offers some sort of justification. Moreover, the functional form in Eq. (1.1) is structured on physical arguments: At short distances the positive and hence repulsive $(1/r)^{12}$ term dominates. This term is related to the Pauli principle. At large interatomic distances, the negative and hence attractive $(1/r)^{6}$ dominates. This term is related to the attractive van-der-Waals interactions. Nevertheless, using Eq. (1.1), the forces on each atom i can be evaluated using the gradient: $F_i = -\nabla_i V_{LJ}$.

However, in most cases, more complex than the pair interactions of Eq. (1.1) have to be considered. For example and as has already been mentioned, the LJ potential does not account for the role of electrons in bond formation and bond directionality. Moreover, the pair interactions are affected by the presence of other neighboring atoms. Therefore, simple models, such as the LJ potential, may show critical shortcomings in the description of the more complex chemical or structural environments such as e.g., in the core of extended defects and/or in the presence of impurities. To address these, more complex and sophisticated interatomic models have been developed, where many-body interactions are explicitly considered. These models consist of a large number of fitting parameters, which are obtained by fitting to experimental and/or ab-initio calculated properties. In the present thesis, we have developed methodologies to accurately parametrize second nearest-neighbor modified embedded atom method (2NN-MEAM) interatomic potentials. These potentials are by now well established and widely applied to study a wide range of materials and material properties and phenomena. Furthermore, their formalism considers that the atoms are embedded in an electron gas that consists of both spherical and angular symmetric electron densities and hence angular forces are explicitly included. They also include many-body screening. These enhance the transferability of the potential.

1.2 Aim and Structure of this work

The newly developed 2NN-MEAM potentials were applied to study interface reconstructions, GB faceting, and C segregation at line junctions in Si as well as fracture properties in Ni and low Re content $\text{Ni}_{1-x}\text{Re}_x$ alloys.

Silicon is the most technologically important and widely studied semiconducting material. This indirect bandgap (1.1 eV) [7] semiconductor is extensively used in the electronics, optoelectronics, and chemical industry, as well as in several casting and steel industries [8–10]. Thanks to its abundance in the earth's crust [11], it is a cost-effective material.

Since the first report on the Si solar module in 1941 [12], Si solar cell has seen a surge in efficiency from ≈1% to ≈25% [12]. Due to these high efficiencies and low production costs, today's photovoltaic market is dominated by the presence of Si solar modules [13]. Nevertheless, there is still significant interest in lowering the production cost and increasing efficiency.

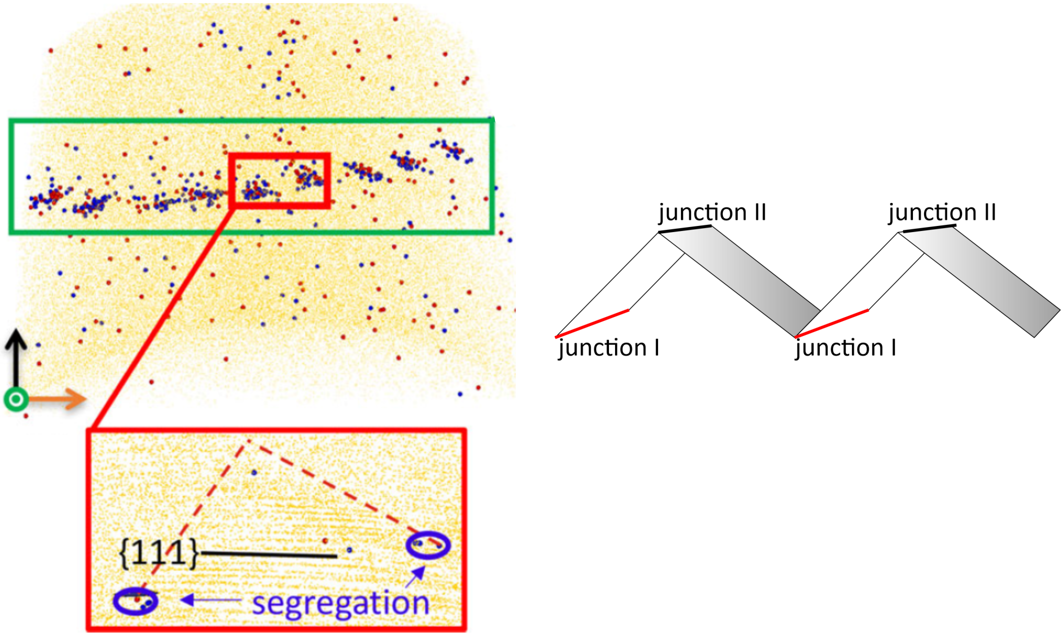

FIGURE 1.1: Right: Asymmetric line segregation of C (red dots), FeN (blue dots), and Si (yellow dots) at a faceted Σ 3 Si tilt GB as observed in 3D atom probe tomography. Left: Schematic representation of the faceted GB. The red line segments indicate the facet junctions where impurities predominantly segregate. Adopted from Ref. [16].

Single-crystal Si solar cells have the highest efficiency in comparison to Si heterostructure and multi-crystalline Si (mc-Si) modules [13, 14]. Although less efficient than single crystal Si, mc-Si solar cells have the advantage of lower production cost [15].

Mc-Si solar cells are manufactured by directional solidification [17]. These modules are characterized by the presence of dislocations, GBs, point defects, stacking faults, etc. [18]. The presence of these defects strongly affects the properties of mc-Si. Moreover, impurities such as C, N, Cu, Fe, P, or O are being attracted by the 1D and 2D extended defects and may significantly reduce the minority carrier lifetime [19, 20]. The source of these impurities is from the natural sources with the ore and others added during the solidification process. Nevertheless, these impurities may introduce deep intragap states which trap carriers and lower the efficiency of the solar modules [21].

Recently a unique segregation mechanism at Si GBs, that goes beyond classical McClean theory, has been reported [16]. More specifically, 1D segregation of C and Fe impurities has been observed at the junction of faceted GBs instead of 2D segregation at planar interfaces (see Fig. 1.1). Moreover, this segregation has a strong anisotropy character: Impurities preferentially segregate at one of the two facet junctions. However, the origin of this anisotropy could not be resolved from the experiment nor could be identified if the anisotropic segregation is the route cause of faceting or vice versa. Therefore, understanding interfaces and their interaction with impurities has both fundamental and technological interest.

Ni and Ni-based superalloys are an indispensable materials system for jet engine turbine blades. They are chosen due to their excellent high-temperature ductility, improved creep, and fatigue resistance. The addition of a few at.% Re into Ni significantly improves the creep resistance and fatigue properties, a phenomenon often called the *"rhenium effect"*. Although these alloys were/are under intensive investigations, the origin of the *rhenium effect* is still under debate (see Ref. [22] and refs therein).

The main aim of this thesis is to parametrize 2NN-MEAM interatomic potentials and apply them to investigate (i) GBs and GB faceting in Si, (ii) topology and strain effects in impurities segregation at GBs and line junctions in Si, and (iii) mode I fracture in low Re content $\mathrm{Ni}_{1x}\mathrm{Re}_x$ alloys. The structure of the thesis is as follows:

- In Chapter 2 a short introduction to the methods employed is given.
- The 2NN-MEAM potentials' formalism and the methodology developed and applied to parametrize these potentials, are presented in Chapter 3.
- In Chapter 4, faceting of $\Sigma 3$ GBs in Si is investigated. Based on DFT and large-scale 2NN-MEAM potential calculations a phase diagram of the facets and line junctions is derived. This diagram provides the energetically most favorable facet and line junction reconstructions as a function of the faceting geometric properties, i.e., the inclination angle and facet period. A key finding that emerges from this diagram is that

higher energy GBs can be stabilized by thermodynamics rather than kinetics when these constitute facets at line junctions.

- In Chapter 5, C segregation at the faceted GBs investigated in Chapter 4 is studied. Interatomic potential for C and SiC were developed and employed to perform atomistic calculations at the experimentally relevant length scale. Based on these calculations the C content distribution is calculated and the origin of the asymmetric impurities' segregation at one of the two line junctions is revealed.
- In the last Chapter (Chapter 6), a new interatomic potential for Ni, Re, and Ni-Re binary is developed. The new potential overcomes the current limitations and artifacts in describing generalized stacking fault energies and traction vs separation profiles. Based on these potentials, the critical stress intensity factor of Ni and low content NiRe alloys is evaluated by employing both linear elastic fracture mechanics and large-scale atomistic calculations of crack propagation in the $\langle 112 \rangle / \{111\}$ Ni fcc slip system. These calculations reveal that fracture in this slip system is ductile. Moreover, in agreement with the *"rhenium effect"*, the addition of a small amount of Re increases the critical stress intensity factor, though the fracture mode remains ductile.

Chapter 2

Methods

First principles and 2NN-MEAM potential calculations are employed in the present thesis to investigate interfaces, interface faceting, and mechanical properties of materials. Density functional theory calculations constitute nowadays the working horse in the field of atomistic calculations in solid-state. Nevertheless, these calculations are restricted by the available computational power to systems consisting of a few thousand atoms. Semi-empirical approaches, such as the 2NN-MEAM potentials, allow for calculating systems that extend to considerably larger and longer length and time scales, respectively. However, this comes at a price of limited transferability. In the following, a short introduction to DFT is given and popular empirical potentials that have been used in the present thesis are briefly presented.

First-principles calculations on a many-body system consist of solving the many-body Schrödinger equation:

$$\hat{H}\psi_j\left(\{\boldsymbol{r}_i\},\{\boldsymbol{R}_I\}\right) = \varepsilon_j\psi_i\left(\{\boldsymbol{r}_i\},\{\boldsymbol{R}_I\}\right) \qquad . \tag{2.1}$$

Here, $\{\boldsymbol{r}_i\}$ denotes the positions of the electrons and $\{\boldsymbol{R}_I\}$ are the positions of the nuclei. $\psi_j(\boldsymbol{r}_i, \boldsymbol{R}_I)$ is the eigenfunction of eigenstate j. ε_j is the eigenvalue.

The Hamiltonian $\hat{H}$ of a system containing N_e electrons and N_I ions can be expressed through the following equation:

$$\begin{aligned}\hat{H} = & \sum_{i}^{N_e}\left[-\frac{1}{2}\nabla_i^2\right] + \sum_{I}^{N_I}\left[-\frac{1}{2M_I}\nabla_I^2\right] + \frac{1}{2}\sum_{I}^{N_I}\sum_{I'}^{N_I}\left[\frac{Z_I Z_{I'}}{|R_I - R_{I'}|}\right] \\ & - \sum_{i}^{N_e}\sum_{I}^{N_I}\left[\frac{Z_I}{|r_i - R_I|}\right] + \frac{1}{2}\sum_{i}^{N_e}\sum_{i'}^{N_e}\left[\frac{1}{|r_i - r_{i'}|}\right]\end{aligned} \tag{2.2}$$

The first two terms on the right-hand side of the above equation are the kinetic energy of the electrons and the ions respectively. M_I is the mass of *I-th* nuclei with respect to the mass of the electron. In the above equation atomic units are used, i.e., $\hbar = 1$, $m_e = 1$, and $\frac{e^2}{4\pi\epsilon_0} = 1$, where m_e and e are the electronic mass and charge, respectively, ϵ_0 is the vacuum dielectric constant, and $\hbar$ is the Planck's constant divided by 2π. r_i and R_I are the positions of i-th electron and I-th nucleus, respectively. Z_I is the atomic number of the nucleus I. The third, fourth, and fifth terms represent the nucleus-nucleus, nucleus-electron, and electron-electron interactions, respectively. The final term is the electrostatic Coulomb repulsion between electrons.

In principle solving Eqs. (2.4) and (2.2) can provide a full description of the many-body system without any approximation. However, due to its complexity and restricted available computational resources, it is not possible to solve these equations directly and approximations have to be implemented. A first approximation is the Born-Oppenheimer approximation [23, 24] which decouples the electronic and the ionic motions. Indeed, the nucleus mass is much higher than the electronic mass, e.g., M_I is at least equal to $1835m_e$. Therefore, the nuclei can be considered to be nearly fixed with respect to electronic motion. This allows to write the wavefunction as a product of the electronic, ψ_e, and ionic, ψ_I wavefunctions:

$$\psi\left(\{\boldsymbol{r}_i\},\{\boldsymbol{R}_I\}\right) = \psi_e\left(\{\boldsymbol{r}_i\};\{\boldsymbol{R}_I\}\right)\psi_I\left(\{\boldsymbol{R}_I\}\right) \quad . \tag{2.3}$$

This allows to solve two problems independently: The electronic wavefunction is calculated by solving the Schrödinger equation for the electronics in a static array of nuclei:

$$\hat{H}_e \psi_e \left(\{\boldsymbol{r}_i\};\{\boldsymbol{R}_I\}\right) = \varepsilon \psi_e \left(\{\boldsymbol{r}_i\};\{\boldsymbol{R}_I\}\right) \quad , \tag{2.4}$$

where $\hat{H}_e = \hat{T}_e + \hat{V}_{ext} + \hat{V}_{int}$ and $\hat{T}_e$, $\hat{V}_{ext}$, and$\hat{V}_{int}$ are the electronic kinetic energy operator, the external potential operator which accounts for the electrons-nuclei interactions, and the operator for the electron-electron interactions. The ionic Hamiltonian is written in a similar form, where the nuclei experience a smeared out potential from the electrons.

2.1 The Hartree-Fock Approximation

Even with explicitly considering the BO approximation, the solution of the many body problem still requires some approximations to make it easily tractable. One of the earliest solution methods is by Hartree-Fock approximation. In Hartree-Fock approximation [25], the wavefunction is written as a Slater determinant of single particle wavefunctions:

$$\psi_{HF} = \frac{1}{\sqrt{N_e!}} \begin{vmatrix} \phi_{\lambda_1}(r_1, s_1) & \phi_{\lambda_2}(r_1, s_1) & ... & \phi_{\lambda_{N_e}}(r_1, s_1) \\ \phi_{\lambda_1}(r_2, s_2) & \phi_{\lambda_2}(r_2, s_2) & ... & \phi_{\lambda_{N_e}}(r_2, s_2) \\ . & . & & . \\ . & . & & . \\ . & . & & . \\ \phi_{\lambda_1}(r_{N_e}, s_{N_e}) & \phi_{\lambda_2}(r_{N_e}, s_{N_e}) & ... & \phi_{\lambda_{N_e}}(r_{N_e}, s_{N_e}) \end{vmatrix}$$

Here, $\phi_{\lambda_i}(r_i, s_i)$ is the single-electron wave function of the λ_i state, having spatial coordinates r_i and spin direction s_i. The single electron wavefunctions form an orthonormal set, i.e., $\langle \phi_{\lambda_i} | \phi_{\lambda_j} \rangle = \delta_{ij}$. The sign of the HF wavefunction will change when any two rows or columns are exchanged. This satisfies the anti-symmetry principle. Moreover, any two rows cannot be the same so that the determinant doesn't become zero, which in turn is consistent with Pauli's exclusion principle. Nevertheless, the electron correlation effects are neglected in the Hartree-Fock approximation which may result in a poor description of the electronic structure

2.2 Density Functional Theory

Density functional theory (DFT) is an alternative, in principle exact, and computationally more efficient to the HF method. In DFT, the many-body problem is formulated in terms of the electron density $n(r)$ instead of the many-body wave function. As a consequence, the computational cost is drastically reduced: The charge density depends only on the 3 spatial coordinates whereas the wavefunction depends on 3N spatial coordinates (or 4N for spin configuration), where N is the number of particles. The original DFT is traced back to the Thomas-Fermi model [26, 27], where the kinetic energy is an explicit function of the electron density. In the Thomas-Fermi model, the electron cloud is assumed to be homogeneously distributed and non-interacting. Although the Thomas-Fermi model was the first building block of modern-day DFT, it didn't account for electron correlation in kinetic energy and didn't include exchange-correlation energies.

Hohenberg-Kohn theorems

DFT is formulated in terms of the two Hohenberg-Kohn theorems and the Kohn-Sham equations. Let us consider the following Hamiltonian for the electronic system:

$$\hat{H}_{\mathrm{e}} = \hat{T}_{\mathrm{e}} + \hat{V}_{\mathrm{e-e}} + \hat{V}_{\mathrm{ext}} \qquad . \tag{2.5}$$

where $\hat{T}_e$ is the kinetic energy term, $\hat{V}_{e-e}$ is the term of the electron-electron interactions, and $\hat{V}_{\mathrm{ext}}$ is the term for the external potential.

The first theorem states that the external potential, $\hat{V}_{ext}(r)$ of the system of interacting particles can be solely determined, within a trivial additive constant, from the electron charge density. If $\Psi\,(\boldsymbol{r})$ is the wavefunction of the

N_e electrons then the charge density is written as:

$$n\left(\boldsymbol{r}\right)=\left\langle \Psi \left| \sum_{i}^{N_e} \delta\left(\boldsymbol{r}-\boldsymbol{r_i}\right) \right| \Psi \right\rangle \tag{2.6}$$

As a consequence, the many-body wave function can be determined by the charge density. This allows to write an energy functional $E\left[n\left(\boldsymbol{r}\right)\right]$ in terms of the elctronc density:

$$E\left[n\left(\boldsymbol{r}\right)\right]=T\left[n\left(\boldsymbol{r}\right)\right]+V_{e-e}\left[n\left(\boldsymbol{r}\right)\right]+\int V_{ext}\left(\boldsymbol{r}\right)n\left(\boldsymbol{r}\right)d\boldsymbol{r} \tag{2.7}$$

The second Hohenberg-Kohn theorem provides the variational principle, i.e., only the ground state charge density minimizes the energy:

$$E\left[\tilde{n_0}\right]\geq E\left[n\right] \qquad , \tag{2.8}$$

where n_0 and $\tilde{n}$ are the ground state and a trial charge density, respectively. The direct consequence of these theorems is that if the functional form $T\left[n\left(\boldsymbol{r}\right)\right]+V_{e-e}\left[n\left(\boldsymbol{r}\right)\right]$ is known, it is sufficient to minimize the $E\left[n\left(\boldsymbol{r}\right)\right]$ functional with respect to n to obtain the ground state of the system.

The Kohn-Sahm equations

Although, the Hohenbrg-Kohn theorem states that all the physical quantities can be obtained from the charge density, obtaining the kinetic energy functional in terms of density is challenging due to the many-body interactions. In the Kohn-Sham approach, the original many-body interacting system is replaced by an auxiliary non-interacting system [28]. Further, it is assumed that the ground state charge density of the interacting system is equal to that of the non-interacting system. If $\phi_i(\boldsymbol{r};s)$ denote the single-particle wavefunctions then the charge density is written as:

$$n(r)=\sum_{i}^{N_{\text{occ}}}|\phi_i(r)|^2 \qquad , \tag{2.9}$$

where the sum runs over all the N_{occ} occupied states. It is also assumed that the single particle wavefunctions are orthogonal:

$$\langle \phi_i | \phi_j \rangle = \delta_{ij} \qquad . \tag{2.10}$$

Based on the aforementioned the Schrödinger equation can be reformulated as:

$$\left[-\frac{\nabla^2}{2} + V_{KS}\left[n(r)\right] \right] \phi_i(r) = \epsilon_i \, \phi_i(r) \qquad . \tag{2.11}$$

Here, $V_{KS}[n(r)]$ is the single electron Kohn-Sham potential which is a functional of electron density $n(\boldsymbol{r})$:

$$V_{KS}\left[n(r)\right] = V_{ext}\left[n(r)\right] + V_H\left[n(r)\right] + V_{xc}\left[n(r)\right] \tag{2.12}$$

Here, V_{ext} is the external potential , V_H is the Hartree potential, and V_{exc} is the exchange-correlation potential. The exchange-correlation potential is calculated from the functional derivative of the exchange-correlation energy:

$$V_{xc}(r) = \frac{\delta E_{xc}}{\delta n(r)} \tag{2.13}$$

The standard procedure to solve the above equations is to solve them self-consistently. The corresponding flow chart is shown in Fig. 2.1.

2.2.1 Exchange and Correlation Functional

Several approximations for the exchange-correlation functionals have been developed [Ref]. In the present thesis, DFT calculations employed the local density approximation (LDA) and the generalized gradient approximation (GGA). These are briefly presented in the following.

Local Spin Density Approximation

LDA is the simplest approximation for the exchange-correlation [28]. In LDA, the exchange-correlation energy per electron at each point, $\boldsymbol{r}$, is equal to that of a homogeneous electron gas that has the same density at the same

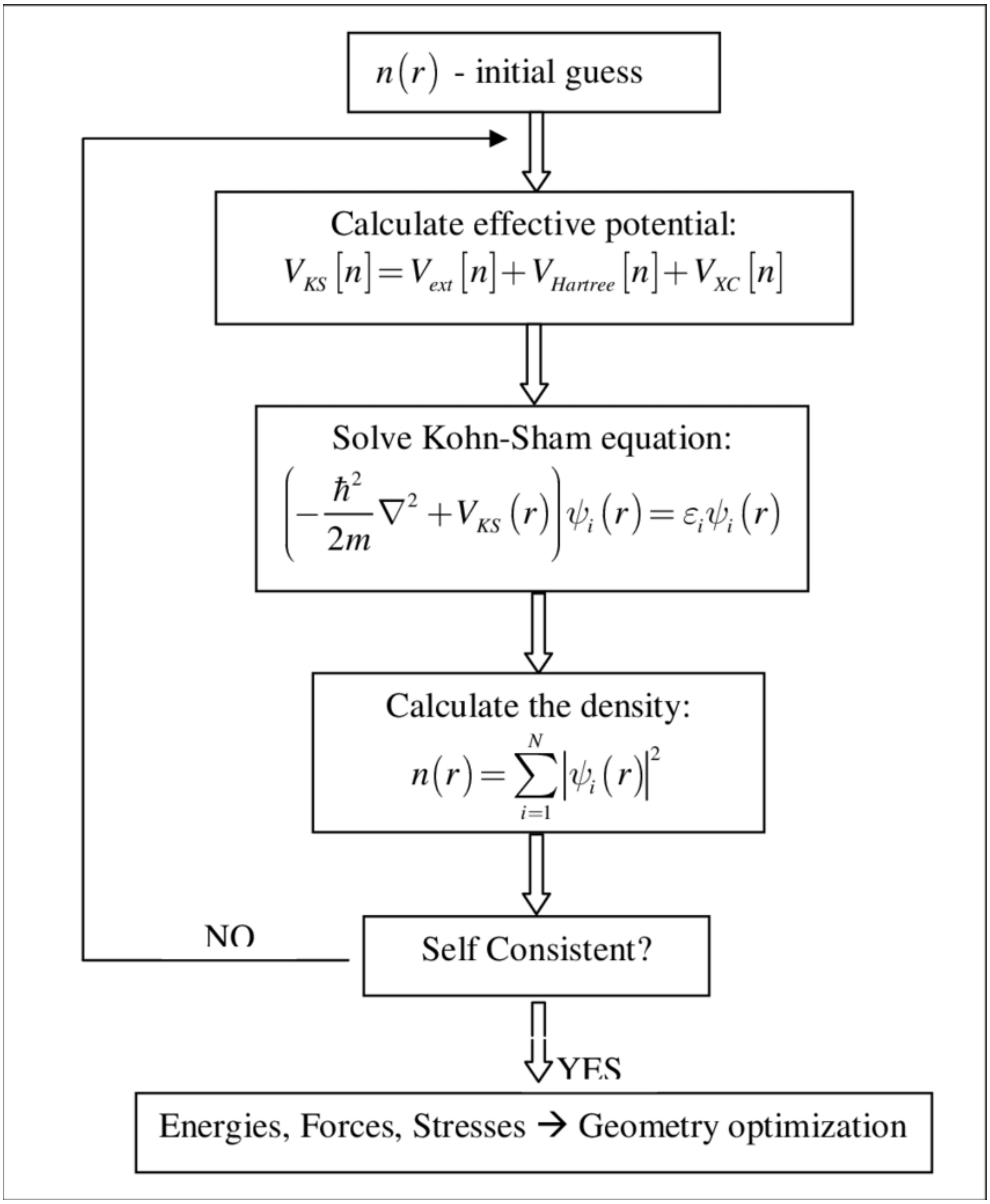

FIGURE 2.1: Flow chart for solving Kohn-Sham problem self consistently

point, $\epsilon_{\mathrm{xc}}^{\mathrm{hom}}$. The exchange-correlation energy is given by:

$$E_{\mathrm{xc}}^{\mathrm{LDA}}[n]=\int d^3\boldsymbol{r}\, n(\boldsymbol{r})\ \epsilon_{\mathrm{xc}}^{\mathrm{hom}}(\boldsymbol{r}) \qquad . \tag{2.14}$$

$\epsilon_{\mathrm{xc}}^{\mathrm{hom}}$ can be split into the exchange and the correlation parts:

$$\epsilon_{\mathrm{xc}}^{\mathrm{hom}}=\epsilon_{\mathrm{x}}^{\mathrm{hom}}+\epsilon_{\mathrm{c}}^{\mathrm{hom}} \tag{2.15}$$

For the exchange part the Dirac exchange functional of the homogenous electron gas is used [29]:

$$\epsilon_{\mathrm{x}}^{\mathrm{hom}} = -\frac{3}{4}\left(\frac{3}{\pi}\right)^{1/3} n\left(\boldsymbol{r}\right)^{1/3} \quad . \tag{2.16}$$

The exact form of the correlation energy is unknown. Nevertheless, the widely used correlation functional is due to Perdew and Zunger [30]. The results are obtained from Quantum-Monte Carlo by fitting the analytical form of $\epsilon_{\mathrm{c}}(r_s)$ with $r_s = \frac{4\pi\, n(r)}{3}^{-1/3}$ being the Weigner Zeitz radius [31]:

$$\epsilon_{\mathrm{c}}^{\mathrm{hom}} = \begin{cases} \gamma/(1+\beta_1\sqrt{r_s}+\beta_2\, r_s) & r_s \geq 1 \\ B+(A+Cr_s)\ln(r_s)+Dr_s & r_s \leq 1 \end{cases} \quad , \tag{2.17}$$

where γ, β_1, β_2, A, B, C, and D are parameters. Despite its overwhelming popularity, LDA has some drawbacks. LDA tends to overbind and underestimate the lattice constants (≈1-3%).

Generalized Gradient Approximation

Although LDA gives correct properties of materials in many cases, it tends to fail in the cases where the charge density in space changes rapidly, e.g., in the case of molecules. The bonding charge density of atoms changes rapidly between atoms. Such a problem can be overcome by considering the exchange-correlation energy not only as a function of charge density but also considering the gradient of charge density. This approximation is called the generalized gradient approximation (GGA). In the framework of GGA, the exchange-correlation energy is written as,

$$E_{\mathrm{xc}}^{\mathrm{GGA}}[n] = \int n(\boldsymbol{r})\ \epsilon_{\mathrm{xc}}\left(n\left(\boldsymbol{r}\right); |\nabla n\left(\boldsymbol{r}\right)|\right)\ d^3\boldsymbol{r} \tag{2.18}$$

The correlation energy is calculated from the local correlation energy with an additive term H_c [32].

$$E_\mathrm{c}^\mathrm{GGA}\left[n\right] = \int n\left(\boldsymbol{r}\right)\ \left(\epsilon_\mathrm{c}^\mathrm{hom}(r_s) + H_\mathrm{c}(r_s,t\right)\ d^3\boldsymbol{r} \qquad , \tag{2.19}$$

where, r_s is the local Seitz radius, t is a dimensionless gradient. $A = \frac{\beta}{\gamma}\frac{1}{exp(-\epsilon_c^\mathrm{hom}/\gamma)-1}$ and $\gamma = \frac{1-\ln 2}{\pi^2}$. β is a constant. The H_c term is written as:

$$H_c(r_s,t) = \gamma \ln\left[1 + \frac{\beta t^2}{\gamma}\left(\frac{1+At^2}{1+At^2+A^2t^4}\right)\right] \tag{2.20}$$

The exchange part is given by:

$$E_\mathrm{x}^\mathrm{GGA}\left[n\right] = \int n\left(\boldsymbol{r}\right) \epsilon_\mathrm{x}^\mathrm{hom}\left[n\right]\left(1 + \kappa - \frac{\kappa}{1+\mu s^2/\kappa}\right) d^3\boldsymbol{r} \tag{2.21}$$

where, κ is chosen to satisfy the Lieb-Oxford bound, μ is chosen to recover linear response from local approximation and $s = |\nabla r_s| \,/\, \left(2(2\,\pi/3)^{(1/3)} r_s\right)$. GGA tends to perform better than LDA in the case of atomization energies, energy barriers, and structural energy differences [33–35]. However, in solids "underbinds" and hence provides higher lattice constants and smaller elastic constants. Nevertheless, both LDA and GGA underestimate the bandgap of semiconducting materials.

2.2.2 Plane Wave Approach

Periodic boundary conditions (PBC) are based on the symmetry of the system and allow to use of a "minimum representation", i.e., a supercell. The translational symmetry of the supercell is defined by the three linear independent vectors $\boldsymbol{a}_1$, $\boldsymbol{a}_2$, and $\boldsymbol{a}_3$.

In a system with a translational invariance, the external potential is periodic ($V\left(\boldsymbol{r}\right) = V\left(\boldsymbol{r}+\boldsymbol{R}\right)$, where $R = n_1\boldsymbol{a}_1 + n_2\boldsymbol{a}_2 + n_3\boldsymbol{a}_3$ and n_i is integer). In such system the Bloch's theorem allows to write the one electron wavefunctions, $\psi_{k,n}(r)$ as:

$$\psi_{\boldsymbol{k},n}\left(\boldsymbol{r}\right) = \mathrm{e}^{i\boldsymbol{k}\cdot\boldsymbol{r}} u_{\boldsymbol{k},n}\left(\boldsymbol{r}\right) \qquad , \tag{2.22}$$

where $\boldsymbol{k}$ is the wave vector which lies in the first Brillouin zone and n is the band index. The function $u_{\boldsymbol{k},n}(\boldsymbol{r})$ has the same periodicity, i.e., $u_{\boldsymbol{k},n}(\boldsymbol{r}) = u_{\boldsymbol{k},n}(\boldsymbol{r}+\boldsymbol{R})$ and can be written as a Fourier series:

$$u_{\boldsymbol{k},n}(\boldsymbol{r}) = \frac{1}{\sqrt{\Omega}} \sum_{\boldsymbol{G}} \tilde{u}_{\boldsymbol{k},n}(\boldsymbol{G})\, \mathrm{e}^{i\boldsymbol{G}\cdot\boldsymbol{r}} \tag{2.23}$$

and

$$\tilde{u}_{\boldsymbol{k},n}(\boldsymbol{G}) = \frac{1}{\sqrt{\Omega}} \int_{\text{cell}} u_{\boldsymbol{k},n}(r)\, e^{-i\boldsymbol{G}\cdot\boldsymbol{r}} d\boldsymbol{r} \tag{2.24}$$

where Ω is the unit cell's volume. $\boldsymbol{G}$ is a reciprocal lattice vector: $\boldsymbol{G} = m_1\boldsymbol{b}_1 + m_2\boldsymbol{b}_2 + m_3\boldsymbol{b}_3$. $\boldsymbol{b}_i$ denotes the primitive reciprocal lattice vectors.

From Eqs. (2.22) and (2.23) the Kohn-Sham wavefunctions can be expanded by planewaves (PW):

$$\psi_{\boldsymbol{k},n}(\boldsymbol{r}) = \sum_{\boldsymbol{G}} C_{\boldsymbol{k},n} \mathrm{e}^{i(\boldsymbol{k}+\boldsymbol{G})\cdot\boldsymbol{r}} \quad . \tag{2.25}$$

In practice, the planewaves are expanded up to a maximum value of the kinetic energy $\frac{1}{2}|\boldsymbol{k}+\boldsymbol{G}|$ which is referred to as the cut of energy.

2.2.3 Pseudopotentials and the Projector Augmented Wave Method

A PW basis set allows for easy implementation of the total energy and Hamiltonian expressions. Moreover, it allows for efficiently evaluating the $H|\psi\rangle$ action by using a fast Fourier transform (FFT). Nevertheless, near the nucleus, the wavefunctions have rapid oscillations. Hence, the number of PWs required to represent satisfactory core electrons becomes cumbersome. A common solution to this is to use pseudopotentials.

The concept underlying the pseudopotential approach is to remove the core electrons and replace the strong ion-electron interactions with a weak pseudopotential. The core electrons are stronger bound, i.e., have much lower energy, and they extend to shorter distances than the valence electrons. Moreover, the bonding is mainly determined by the valence electrons. These allow treating the core electrons as inner (frozen-core approximation). To achieve this, the electrostatic interactions of the valence electrons with the cores are described by pseudopotentials. Within the pseudopotentials description, the depth of the nucleus potential is artificially reduced in order to reproduce the valence electrons' eigenvalues and eigenfunctions outside the core region.

In the present thesis, the Vienna Ab initio Simulation Package (VASP) is used for all DFT calculations. In VASP, the projector augmented-wave (PAW) scheme is implemented. PAW scheme combines PWs in the interstitial region with spherical waves around the core. This allows describing the oscillations of the valence electron wave functions without the computational demand for a large basis set. More information regarding the PAW method can be found in Refs. [36, 37].

2.3 Interatomic potentials

Although very accurate, due to high computational demand DFT calculations are nowadays limited to simulation cells consisting of a few thousand atoms. Therefore, to study phenomena that extend to longer length scales, e.g., GB faceting, fracture [38], and dislocation mobility [39], *ab-initio* calculations may not be sufficient. An alternative approach is to employ interatomic force fields to calculate the total energy and forces. These calculations can treat systems consisting of millions of atoms and in many cases can address phenomena at the experimental relevant length scales. However, interatomic force fields often lack transferability.

Some of the most popular interatomic force field models that have been used in the present thesis are the Stillinger-Weber potential (SW) [40], the Tersoff type bond order potential [41], and the modified embedded atom method potential [42]. We have evaluated these potentials in modeling Si GBs, C segregation in Si GBs, and low Re content NiRe alloys. In the following sections, the formalism of the SW and the analytical bond-order potentials is provided. In the next chapter, a detailed description of the MEAM

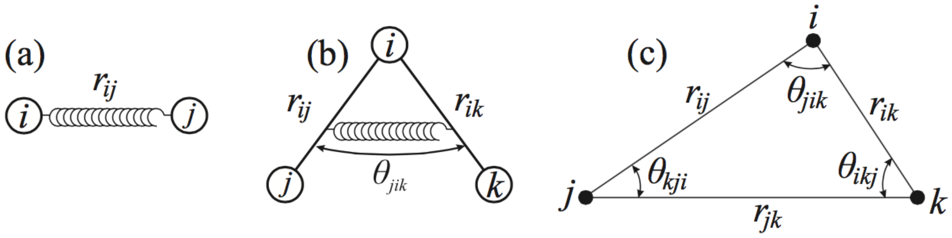

FIGURE 2.2: Schematic representation of (a) bond stretching and (b) bond bending. (c) Triplet of atoms and geometric parameters used in the SW 3-body angle term. The Figure has been adopted from Ref. [43].

potentials and a methodology to systematically parametrize them are given.

2.3.1 Stillinger Weber potentials

One of the most widely used interatomic potentials for tetrahedrally coordinated semiconductors like Si is the Stillinger-Weber potential (SW) [40]. Unlike pair potential, such as the Lennard-Jones potential where stabilizing diamond structure is challenging, the SW potential consists of 2- and 3-body terms. The total energy of the system in the SW framework is written as:

$$E = \sum_i \sum_{j \leq i} \phi_2 \left(r_{ij} \right) + \sum_i \sum_{j \neq i} \sum_{k \geq j} \phi_3 \left(r_{ij}, r_{ik}, \theta_{ijk} \right) \quad . \tag{2.26}$$

Here the first term is the pair potential and the second term is for the 3-body interactions. r_{ij} is the distance between atoms i and j. The pair potential describes forces against bond stretching and has the following form:

$$\phi_2(r_{ij}) = \begin{cases} \varepsilon A \left(B r_{ij}^{-p} - r_{ij}^{-q} \right) \exp \left[\left(r_{ij} - a \right)^{-1} \right], & \text{if } r_{ij} < a \\ 0, & \text{if } r_{ij} \geq a \end{cases} \quad , \tag{2.27}$$

where the parameters A, a, B, and p take positive values. ε has energy units. At the cutoff radius, a, the potential convergences smoothly to zero. The cut off distance defines the range of interactions.

The 3-body term describes the forces against bond bending and it is written as a function of the interatomic distance as well as an angular dependent term:

$$\phi_3\left(r_{ij}, r_{ik}, \theta_{jik}\right) = \varepsilon\lambda \exp\left[\gamma\left(r_{ij}-a\right)^{-1} + \gamma\left(r_{ik}-a\right)^{-1}\right]\left(\cos\theta_{jik} + \frac{1}{3}\right)^2 \quad . \tag{2.28}$$

γ and λ take positive values. θ_{jik} is the angle between the vectors $\boldsymbol{r}_{ij}$ and $\boldsymbol{r}_{ik}$.

Despite the success of SW potentials in describing bulk ground-state phases, elastic constants, and liquid phases [40], it still poses challenges in calculating surface reconstructions, generalized stacking fault energies, etc. (see e.g., Table 4.3).

2.3.2 Analytical Bond Order Potentials

In the present thesis, a Tersoff-Brenner type bond order potential developed by Erhart *et al.* [41] has been used in the calculations of C segregation in Si GBs. The total energy in the framework of Tersoff-Brenner potential is written as a sum of attractive and repulsive interactions [44] as follows:

$$E = \sum_{i \geq i} f_c(r_{ij}) \left[V_R(r_{ij}) - \frac{b_{ij}+b_{ji}}{2} V_A(r_{ij})\right] \quad , \tag{2.29}$$

where, $V_R(r)$ and $V_A(r)$ are the repulsive and attractive terms, respectively, and are written as Morse-type potentials:

$$V_R\left(r\right) = \frac{D_0}{S-1}\exp\left[-\beta\sqrt{2S}\left(r-r_0\right)\right] \tag{2.30}$$

and

$$V_A\left(r\right) = \frac{SD_0}{S-1}\exp\left[-\beta\sqrt{2/S}\left(r-r_0\right)\right] \quad . \tag{2.31}$$

Here, D_0 is the dimer binding energy, r_0 is the equilibrium nearest neighbor distance in the reference structure, r is the distance between two atoms, β is related to the ground state dimer frequency, and S is calculated from the

Pauling plot. $f_c\left(r\right)$ is the hopping integral and has the following form:

$$f_c\left(r\right)=\begin{cases}1 & \text{if } r\leq R-D\\ \frac{1}{2}-\frac{1}{2}\sin\left(\frac{\pi(r-R)}{2D}\right), & \text{if } \left|R-r\right|\leq D\\ 0 & \text{if } R+D\leq r\end{cases}, \tag{2.32}$$

where R, and D are the position and width of the hopping integral cutoff function. The bond order parameter, b_{ij}, is written in terms of the angular dependent term ζ_{ij}:

$$b_{ij}=\left(1+\zeta_{ij}\right)^{-1/2}, \tag{2.33}$$

where,

$$\zeta_{ij}=\sum_{k(\neq i,j)} f_c\left(r_{ik}\right)\exp\left[2\mu-\left(r_{ij}-r_{ik}\right)\right]g\left(\theta_{ijk}\right) \tag{2.34}$$

and

$$g\left(\theta\right)=\gamma\left(1+\frac{c^2}{d^2}-\frac{c^2}{d^2+\left(h+\cos\theta\right)^2}\right). \tag{2.35}$$

Here, the parameters γ, μ, c, d, and h are obtained from the fitting of the potential.

As can be seen in Tables 4.3, 5.3, and 5.4, the potentials developed by Erhart *et al.* [41] gave an excellent description of the energy differences between different crystal phases, the elastic constants, and the vacancy formation energies in Si, C, and 3C-SiC. However, they failed to describe the generalized stacking fault energies.

Chapter 3

Modified Embedded Method Interatomic Potential

3.1 Introduction

MEAM interatomic potentials are nowadays well established and widely applied to study a wide range of materials and material properties and phenomena such as GBs, phase transformations, dislocations, fracture, thermal properties, etc. [38, 45–49]. The MEAM potentials are unique in that they are the first interatomic potentials that with a single formalism can be and have been applied to successfully describe a wide and diverse range of elements encompassing various bonding characteristics. These include materials in various crystal structures such as fcc, bcc, hcp, diamond, or even gas phases [42].

The MEAM potentials [42] constitute an extension of the embedded atom method (EAM) potentials developed by Daw and Baskes [50, 51]. Compared to EAM potentials, MEAM interatomic interactions include angular contributions similar to spherical harmonics to the electron density [see Eqs. (3.8)-(3.11) in the next Section]. The success of MEAM potential over the other interatomic potentials can be attributed to the following facts: The MEAM potential formalism considers that the atoms are embedded in an electron gas that consists of both spherical and angular symmetric electron densities [42]. Furthermore, the formalism of MEAM potential includes many-body screenings. These, i.e., the inclusion of angular forces and many-body screening, constitute these potential robust and enhance their transferability in a wide range of deformation conditions in solid-state.

Nevertheless, MEAM potentials show shortcomings in calculating properties of bcc metals such as the inadequate description of low index surfaces or predicting ground state crystal phases other than bcc for Fe, Cr, or Mo (see Ref. [52] and refs therein). The MEAM formalism considers only nearest-neighbor interactions. However, in bcc materials, the second nearest-neighbor interactions may not be negligible. Indeed, in bcc, the second nearest neighbor distance is only ≈15% larger than the first nearest neighbor distance. To address the aforementioned shortcomings, B.-J. Lee and Baskes extended the MEAM formalism to partially include second nearest interactions by adjusting the many-body screening (2NN-MEAM) [52].

In this thesis, interatomic potentials are employed to investigate GBs, lines junctions, and fracture. In both cases, areas of highly strained material are present, and/or the coordination of the atoms may differ strongly from the coordination in the ground state crystal structure. Therefore, in order to provide both good qualitatively and quantitatively descriptions, 2NN-MEAM potentials have been developed and applied. The formalism of the 2NN-MEAM potential is described in detail in the next Section and in Section 3.3, the methodology developed and employed to parametrize the potential is discussed.

3.2 MEAM potential formalism

3.2.1 Unary system

As has already been mentioned, the MEAM potentials constitute an extension of the EAM potential. In the EAM potentials, the total energy is written as the sum of the short-range pair energy and the embedding energy. The latter depends on the electron density which has spherical symmetry. Nevertheless, MEAM potentials further include the angular dependency of the electron density. The original formulation considered only the first nearest neighbor (1NN-MEAM) interactions of atoms. The 1NN formulations were later extended to include second nearest neighbor (2NN-MEAM) interactions [53]. In 2NN-MEAM potential, the total energy is written as [42]:

$$E = \sum_i \left[F_i(\bar{\rho}_i) + \frac{1}{2}\sum_{j\neq i}\phi_{ij}(r_{ij})\right] \quad . \tag{3.1}$$

In the above equation, the first term, i.e., $F_i(\bar{\rho}_i)$, is the embedding energy of atom i. The embedding energy is a function of the background electron density $(\bar{\rho}_i)$ at site i [42, 54]. The pair energy, $\phi(r_{ij})$ is written as a function of the interatomic distance, r_{ij} between atoms i and j. The energy required to place an atom at the site i having the background electron density $\bar{\rho}_i$ is called embedding energy. The functional form of the embedding energy is:

$$F_i(\bar{\rho}_i) = \begin{cases} A_i\ E_i^0\ \bar{\rho}_i\ \ln(\bar{\rho}_i) & \text{if } \bar{\rho}_i \geq 0 \\ -A_i\ E_i^0\ \bar{\rho}_i & \text{otherwise} \end{cases} \quad , \tag{3.2}$$

where E_i^0 is the negative of cohesive energy or the sublimation energy and A_i is the embedding parameter. The value of A_i depends on the element type.

The background electron density, $\bar{\rho}_i$ is written as following,

$$\bar{\rho}_i = \frac{\rho_i^{(0)}}{\rho_i^0} G(\Gamma_i) \tag{3.3}$$

where,

$$\Gamma_i = \sum_{k=1}^{3} t_i^{(k)} \left(\frac{\rho_i^{(k)}}{\rho_i^{(0)}}\right)^2 \tag{3.4}$$

and

$$G(\Gamma_i) = \begin{cases} \sqrt{1+\Gamma_i}, & \text{if } \Gamma_i \geq -1 \\ -\sqrt{|1+\Gamma_i|}, & \text{if } \Gamma_i < -1 \end{cases} \tag{3.5}$$

The density of electron of order, k i.e $\rho_i^{(k)}$ is described below by the Eqs. (3.8)-(3.11). In Eq. (3.3), ρ_i^0 is the reference electron density. The reference electron density is given as,

$$\rho_i^0 = \rho_{i0}\; Z_{i0}\; G(\Gamma_i^{ref}) \qquad . \tag{3.6}$$

ρ_{i0} is used to scale the electron density. The first nearest neighbor coordination, Z_{i0}, is calculated from the reference structure. For diamond and zincblende crystals the nearest neighbor coordination is 4, and for hcp, and fcc crystals it is 12. The parameter Γ_i^{ref} in the reference electron density is calculated from the following equation

$$\Gamma_i^{ref} = \frac{1}{Z_{i0}^2}\sum_k^3 t_i^{(k)} s_i^{(k)} \qquad . \tag{3.7}$$

The shape factor of atom i, $s_i^{(k)}$, is calculated based on the crystal structure and can be obtained from the work of Baskes *et al.* [42].

By superimposing the atomic densities, the electron densities are obtained as in Eqs. (3.3)-(3.5). Nevertheless, the atomic densities are further screened by applying the screening function S_{ij} as follows,

$$\rho_i^{(0)} = \sum_{j\neq i} \rho_j^{a(0)}(r_{ij})\; S_{ij} \tag{3.8}$$

$$(\rho_i^{(1)})^2 = \sum_{\alpha}\left[\sum_{j\neq i}\rho_j^{a(1)}\frac{r_{ij\alpha}}{r_{ij}}S_{ij}\right]^2 \tag{3.9}$$

$$(\rho_i^{(2)})^2 = \sum_{\alpha,\beta}\left[\sum_{j\neq i}\rho_j^{a(2)}\frac{r_{ij\alpha}r_{ij\beta}}{r_{ij}^2}S_{ij}\right]^2 - \frac{1}{3}\left[\sum_{j\neq i}\rho_j^{a(2)}(r_{ij})S_{ij}\right]^2 \tag{3.10}$$

$$(\rho_i^{(3)})^2 = \sum_{\alpha,\beta,\gamma}\left[\sum_{j\neq i}\rho_j^{a(3)}\frac{r_{ij\alpha}r_{ij\beta}r_{ij\gamma}}{r_{ij}^2}S_{ij}\right]^2 - \frac{3}{5}\sum_{\alpha}\left[\sum_{j\neq i}\rho_j^{a(3)}(r_{ij\alpha})S_{ij}\right]^2 \tag{3.11}$$

The α-th component of the displacement vector is given as $r_{ij\alpha}$ where the value of α ranges between 1-3. The screening function between atoms i and j is given as S_{ij} and is discussed in the following Section 3.2.3. The background electron densities including higher-order terms are provided by Eqs. (3.8)-(3.11).

While EAM potentials are based on linear superposition of spherical average electron densities [42], in the MEAM formalism higher-order electron density terms are included. The background electron densities are constructed as in the in Eqs. (3.8)-(3.11), and those can be considered as s, p, d, and f electron densities [42]. The unscreened electron density, $\rho_i^{a(k)}$, in the Eqs. (3.8)-(3.11), is given as an exponential decay function as:

$$\rho_i^{a(k)}(r_{ij}) = \rho_{i0}\, exp\Big[-\beta_i^k\Big(\frac{r_{ij}}{r_i^0}-1\Big)\Big] \tag{3.12}$$

Here, the nearest neighbor distance, r_i^0, is for the reference structure. $\beta^{(k)}$ is a fitting parameter. The weighting factor for the electron density is written as:

$$t_i^{(k)} = \frac{\sum_{j\neq i} t_{0,j}^k \rho_j^{a(0)} S_{ij}}{\sum_{j\neq i} (t_{0,j}^k)^2 \rho_j^{a(0)} S_{ij}} \tag{3.13}$$

The pair interactions are screened using the same screening function formalism as in the electron density. The screening in the pair interactions is introduced as follows:

$$\phi_{ij}(r_{ij}) = \bar{\phi}_{ij}(r_{ij}) S_{ij} \qquad , \tag{3.14}$$

where $\bar{\phi}_{ij}(r_{ij})$ has the following form:

$$\bar{\phi}_{ij}(r_{ij}) = \frac{1}{Z_{ij}}\Big[2E_{ij}^u - F_i\Big(\frac{Z_{ij}}{Z_i}\rho_j^{a(0)}(r_{ij})\Big) - F_j\Big(\frac{Z_{ij}}{Z_i}\rho_j^{a(0)}(r_{ij})\Big)\Big] \qquad . \tag{3.15}$$

The $E_{ij}^u(r_{ij})$ energy term in the above equation is considered from the Rose universal equation of state with an exponential decay function [55]:

$$E_{ij}^u(r_{ij}) = -E_{ij}(1 + a_{ij}^*(r_{ij}) + \delta a_{ij}^{*3}(r_{ij}))\; e^{-a_{ij}^*(r_{ij})} \qquad , \tag{3.16}$$

where a_{ij}^* is the scaled interatomic distance with respect to the equilibrium interatomic distance in the reference structure. The parameter a_{ij}^* is obtained by scaling the interatomic distance, r_{ij} as following:

$$a_{ij}^* = \alpha\Big(\frac{r_{ij}}{r_{ij}^0} - 1\Big) \tag{3.17}$$

The dimensionless parameter, α is related to bulk modulus, B, the cohesive energy, E_c, and the equilibrium lattice volume, Ω [42]:

$$\alpha = \sqrt{\frac{9B\Omega}{E_c}} \tag{3.18}$$

3.2.2 Binary system

For a system having two species, the interatomic potential is constructed using the individual element parameters as well as additional parameters to describe the interactions between the different species. In this case, the total energy per atom, $E^u_{ij}(R)$, is written as:

$$\begin{aligned} E^u_{ij}(R) = \frac{1}{2}\Big[F_i(\bar{\rho}_i) + F_j(\bar{\rho}_j) + Z^{ij}_1\ \phi_{ij}(R) + \\ \frac{1}{2}Z^{ij}_2 S_{ii}\ \phi_{ii}(aR) + S_{jj}\ \phi_{jj}(aR)\Big] \end{aligned} \tag{3.19}$$

In the above equation, R is the nearest neighbor interatomic distance in the binary system. F_i and F_j are the embedding energy terms for species i and j. The first nearest neighbor coordination is denoted as Z^{ij}_1 and the second nearest neighbor coordination as Z^{ij}_2. a is the ratio of second and first nearest neighbor distances. The pair energy of two different species is calculated as:

$$\begin{aligned} \phi_{ij}(R) = \frac{1}{Z^{ij}_1}\Big[2E^u_{ij}(R) - F_i(\bar{\rho}_i) - F_j(\bar{\rho}_j) - \\ \frac{1}{2}Z^{ij}_2 S_{ii}\ \phi_{ii}(aR) + S_{jj}\ \phi_{jj}(aR)\Big] \end{aligned} \tag{3.20}$$

3.2.3 Many-Body Screening

A unique characteristic of the 2NN-MEAM formalism with respect to other valence force field models is the introduction of many-body screening. This is implemented by modifying the interatomic interactions between a pair of atoms i and j in presence of a third atom k. Let us first consider S_{ij} to be a screening function between atoms i and j. S_{ij} is the product of a radial cutoff

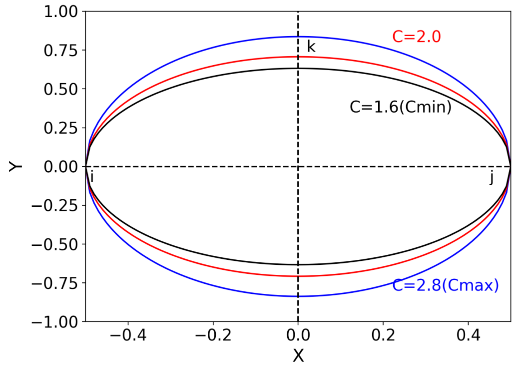

FIGURE 3.1: Schematic representation of screening between two neighboring atoms *i* and *j* by a third atom *k* [see Eq. (3.26)]. If the atom *k* lies outside (inside) of the blue (black) ellipse which corresponds to $C > C_{\text{max}}$ ($C < C_{\text{min}}$), the pair interaction *i* - *j* is unscreened (fully screened), respectively. If atom *k* lies in between the blue and black ellipses, e.g. on the red ellipse, then $C_{\text{min}} < C < C_{\text{max}}$ and the interaction is partially screened. The units in both axes are arbitrary.

function, f_c, and a three-body term, $\bar{S}_{ij}$:

$$S_{ij} = \bar{S}_{ij}\, f_c\left(\frac{r_c - r_{ij}}{\Delta r}\right) \quad . \tag{3.21}$$

Δr and r_c are the smoothing and the cut-off distances, respectively. The smooth cut off function is defined as:

$$f_c(x) = \begin{cases} 1 & \text{if } x \geq 1 \\ -[1-(1-x)^4]^2, & \text{if } 0 \geq x \leq 1 \\ 0 & \text{if } x \leq 0 \end{cases} \tag{3.22}$$

and the three body term is obtained as following,

$$\bar{S}_{ij} = \prod_{k \neq i,j} S_{ijk} \tag{3.23}$$

with

$$S_{ijk} = f_c\Big(\frac{C_{ijk} - C_{min,ijk}}{C_{max,ijk} - C_{min,ijk}}\Big) \tag{3.24}$$

The functional form of C_{ijk} is as follows,

$$C_{ijk} = \frac{2(X_{ij} + X_{jk}) - (X_{ij} - X_{jk})^2 - 1}{1 - (X_{ij} - X_{jk})^2} \tag{3.25}$$

Where $X_{ij} = (r_{ij}/r_{ik})^2$ and $X_{kj} = (r_{kj}/r_{ij})^2$. C_{min} and C_{max} are the limiting values of C.

Let us consider an ellipse that passes through atoms i and j with the major axis along the y direction and the minor axis connecting the two atoms [see Fig. 3.1]. The equation of this ellipse can be written as:

$$X^2 + \frac{Y^2}{C} = \frac{1}{4} \tag{3.26}$$

When atom k is outside the ellipse given by $C = C_{max}$ then this atom doesn't screen the interaction between i and j and $S_{ijk} = 1.0$. When, however, atom k is inside the ellipse given by $C = C_{min}$ then this atom completely screens the interaction between i and j and $S_{ijk} = 0.0$. In all other cases, the interaction is partially screened and the value of S_{ijk} is between 0 and 1 [see Eq. (3.23)].

The minimum and maximum screening parameters, C_{min} and C_{max}, strongly influence various calculated physical properties. It has been shown that lowering the value of C_{min} improves the thermal expansion coefficient of Ni [56], yields the correct ordering of surface energies of low index surfaces in bcc Li [38], and improves the GSFE for bcc [39] and diamond Si [57]. It has been further demonstrated that the values of C_{min} play a significant role in improving the GSFE, and the GB energies. Large values of C_{min} result in oscillatory behavior of the GSFE profiles. However, lower values of C_{min} result in overestimation of the GB energies and in over- or under-coordinated structures in Si during annealing. Hence, as it will be discussed later, the value of C_{min} to be implemented is a compromise between GSFE and GB energies on the one hand and the structural properties of Si on the other.

3.2.4 MEAM parameters

In summary, for a unary system, the 2NN-MEAM potential consists of 16 parameters. These are the cohesive energy, E_c, the equilibrium nearest neighbor distance, r_e, the four parameters for the decay of the electron density, β_i, $i = 0 - 3$, three parameters for the weighting of the electron density, t_i, $i = 1 - 3$, α that correlates with Rose's universal equation of state, A that scales the embedding energy, the screening parameters, C_{min} and C_{max}, the cutoff distance of the interatomic interactions, r_c, the smoothing distance, Δr, and the parameter δ that is used in Rose's universal equation of state.

For a binary system consisting of elements A, and B the potential has 32 parameters for the individual elements. Apart from these, the following parameters are required to describe the binary potentials. These are the cohesive energy of the binary, $E_c(A, B)$, the equilibrium nearest neighbor distance, $r_e(A, B)$, the bulk modulus related parameter, $\alpha(A, B)$, and the smoothing and cutoff distances, Δr and r_c, respectively. Furthermore, there are eight screening parameters, four C_{min} and four C_{max}, for the different combinations of A and B atoms at the triplet. Furthermore, the ratio of mixing of the electron density (ρ_A/ρ_B) is used to parametrize a binary potential. Nevertheless, in the present thesis, only the reference electron density of the individual element is used to fit the potential, i.e., this parameter is not tuned in the binary system.

3.3 Parametrization of MEAM Potentials

The parametrization of a MEAM potential is not straightforward. However, parametric studies that identified the relation between MEAM parameters and materials' properties, revealed that in the MEAM framework, some parameters are confined to a few properties only [38, 39, 42]. Therefore, a parametric study that provides the relation between the MEAM parameters and the properties constitutes an important ingredient in the strategy to parametrize MEAM potentials.

A first step toward the parametrization of a MEAM potential is to perform a parametric study and construct the correlation table, i.e., a table that maps and quantifies the influence of each potential parameter on the material's properties. This is achieved by calculating the relative change in a property caused by the relative change in a parameter. As it will be described next, employing the correlation table, the potential can be parametrized by an iterative trial and error approach. This approach can be easily generalized to parametrize the interatomic potentials irrespective of the ground state crystal structure.

Applying a parametric study on the 2NN-MEAM potential, the correlation of each parameter to the target properties has been obtained. These are listed in Table 3.1. Using this Table the 2NN-MEAM potential for Si can be parametrized following the aforementioned trial and error iterative approach. The potential was fitted on the GSFE for shear along $[1\bar{1}0]$ and $[11\bar{2}]$ in the $\{111\}$ shuffle plane, the cohesive energy differences between the Si in the diamond structure and in the β-tin, bcc, and fcc structures, and the elastic constants (C_{ij}).

The correlation table was obtained by changing each parameter by 10%, 20%, and 30%. If the change in the property was less than 1%, the correlation is noted as N, i.e., no correlation. If however, the change in the property was between 1% and 7% then it is noted as M, i.e., mild correlation and if the change was larger than 7%, then it is termed S, i.e., strong correlation. For example, in the Table cell that depicts the correlation between parameter α and the bulk modulus B the values are written as SSS, i.e., the bulk modulus changes by more than 7% even if parameter α is changed by 1%. In all cells, the first, second, and third character indicates the correlation for 10%, 20%, and 30% change in the parameter, respectively.

TABLE 3.1: Correlation table between the properties of Si and 2NN-MEAM parameters. S indicates strong correlation (properties change more than 7%), M indicates mild correlation (properties change between 1% - 7%) and N indicates no correlation (properties change less than 1%). B is the bulk modulus, E is the surface energy, C_{ij} is the elastic constant. For example, in column α and row, B the values are written as SSS. Among these three S, the first S means, the 10% change of the values α shows more than 7% change in the value of bulk modulus, B, i.e, the change yields a strong correlation. The other two S indicate also strong correlation if the parameter α is changed by 20%, and 30%.

	α	β_0	β_1	β_2	β_3	A	t_1	t_2	t_3	r_c	δr	C_{min}	C_{max}
B	SSS	NNN	NNN	NNN	NNN	NNN	NNN	NNN	NNN	NNN	NNN	NNN	NNN
$E_{\{100\}}$	SSS	MSS	SSS	SSS	SSS	SSS	MSS	MMS	MSS	NNN	NNN	SSS	NNN
$E_{\{110\}}$	NNN	NMM	NNN	MMM	NNN	MMM	MSS	MMS	MMM	NNN	NNN	NNN	NNN
$E_{\{111\}}$	NNN	NNN	NNN	NNN	NNN	MMM	MSS	MMS	MMM	NNN	NNN	NNN	NNN
$tin-dia$	MSS	SSS	SSS	SSS	SSS	SSS	SSS	SSS	SSS	NNN	NNN	NNN	NNN
$fcc-dia$	SSS	SSS	SSS	SSS	SSS	SSS	SSS	SSS	SSS	NNN	NNN	NNN	NNN
$bcc-dia$	SSS	SSS	MMM	MMM	MMM	SSS	MMM	MMM	SSS	NNN	NNN	NNN	NNN
$sc-dia$	SSS	SSS	MMM	MMM	NMS	SSS	MMM	MMM	SSS	NNN	NNN	NNN	NNN
C_{11}	SSS	NNN	NNN	NNN	NNN	MMS	NNN	NMM	MMM	NNN	NNN	NNN	NNN
C_{12}	SSS	NNN	NNN	NNN	NNN	MSS	NNN	MMM	MSS	NNN	NNN	NNN	NNN
C_{44}	MMM	MMS	MMS	MMM	MMM	SSS	SSS	NNN	MMM	NNN	NNN	NNN	NNN
E_v	SSS	SSS	MMM	MMM	MMM	SSS	MSS	NNN	MMM	NNN	NNN	NNN	NNN
$U_{unstable}$	NNN	MSS	NMM	NNN	NNN	SSS	MSS	MMM	MSS	NNN	NNN	SSS	NNM
GSFE shape	NNN	MSS	NMM	NNN	NNN	SSS	MSS	MMM	MMS	NNN	NNN	SSS	NMM
GB energy	NNN	MSS	NNN	NNN	NNN	SSS	MSS	MMM	MSS	NNN	NNN	SSS	MSS

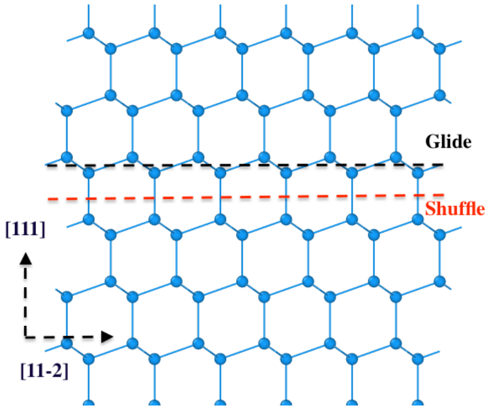

FIGURE 3.2: Two inequivalent {111} cuts of the basal plane in the diamond crystal. In the shuffle cut (red dashed line) one bond per atom is broken and in the glide cut three bonds per atom are broken.

The iterative parametrization procedure can vary depending on the target properties. Nevertheless, considering the correlation Table it can be easily generalized. In the following, this procedure is described for the parametrization of the 2NN-MEAM potential for Si with the aim of accurately describing GBs and GB faceting. The parametrization of the 1NN-MEAM potential for Si by Baskes is used as the basis for the present potential [42].

- In the first step, the cohesive energy, E_c, is set to the experimental value. Moreover, the choice of the pair energy function, see Eq. (3.16), and of the electron density functional, see Eq. (3.5), is made in this step.

- In the second step, the bulk modulus is fitted by changing the parameter α. This parameter scales proportionally with the square root of the bulk modulus and depends on the atomic volume, Ω, and the cohesive energy, E_c [see Eq. (3.18)]. Therefore, this parameter can be initially fixed. However, as the atomic volume, cohesive energy, and bulk modulus are correlated with other parameters as well (see Table 3.1) parameter α may have to be adjusted in subsequent iteration step/s. In this case the bulk modulus can be recovered by setting a new value of $\alpha = \alpha_{current}\sqrt{B_{target}/B_{current}}$, where $\alpha_{current}$ and $B_{current}$ are the current values of the parameter and the calculated bulk modulus [39]. B_{target} is the targeted value of the bulk modulus.

- Next, the GSFE for shear along $[1\bar{1}0]$ in the $\{111\}$ plane is fitted. The parameter β_0 was used to adjust the unstable stacking fault energy and C_{min} was used to remove possible discontinuities in the GSFE profile. As can be seen in Table 3.1, the GSFE curve is correlated strongly not only to β_0 and C_{min} but to A as well. However, only β_0 and C_{min} were used to iterate over GSFE. Furthermore, first-principle calculations revealed that the ideal shear strength is strongly related to the valence charge distribution and the directionality of the bonds [58]. Since the GSFE is related to the ideal shear strength, it is more intuitive to correlate the electron density with the GSFE through parameter β_0. The diamond crystal has two inequivalent cuts of the {111} plane [59]. The shuffle where one bond per interface atom is deformed or broken and the glide cut where three bonds per atom are deformed or broken (see in Fig. 3.2). In the present work, we considered the shuffle cut to parametrize the potential.

- Parameter A was used to adjust the cohesive energy difference between diamond and fcc crystals.
- Parameter t_3 was used to adjust the cohesive energy differences between diamond and β-tin, sc, and bcc structures.
- The parameters (t_2 and β_2 were used to adjust the energies of the {100}, {110}, and {111} surfaces, $E_{\{100\}}$, $E_{\{110\}}$, and $E_{\{111\}}$, respectively and the elastic constants, C_{ij}.

The above procedure was repeated until the properties of the material are no longer improved. During the change of each parameter, the change in the target as well as in all other properties is simultaneously monitored. A change is applied only if the target properties are improved while the other properties are almost not affected. Otherwise, the change is not applied and the next step is followed. This is schematically shown in Fig. 3.3. In the first step parameter, α is fitted. In the second step, the GSFE is improved by changing parameters β_0 and C_{min}. However, as is depicted in Table 3.1, these two parameters strongly influence the {100} surface energy, the vacancy formation energy, the C_{44} elastic constant as well as the phase transitions energies. Therefore, these two parameters are varied in such a way that the GSFE is improved and the effect on all other aforementioned properties is minor and

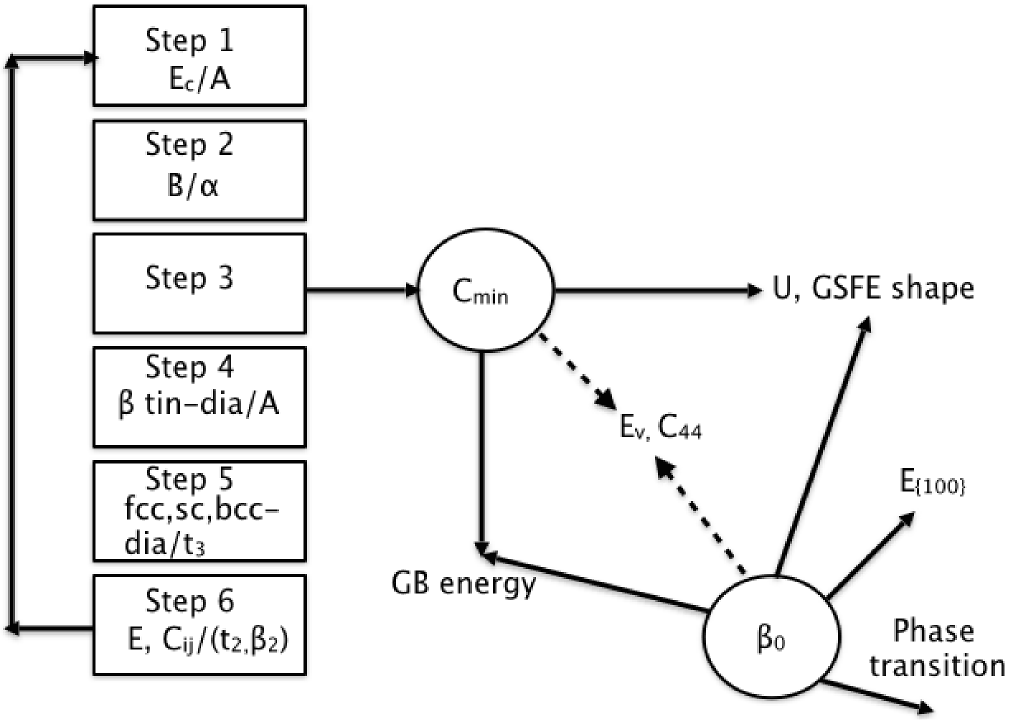

FIGURE 3.3: Schematic diagram highlighting the dependence of material properties on the parameters C_{min}, and β_0. These parameters strongly influence the GSFE energy and the GSFE profile, the GB energies. However, they have a small impact on the vacancy formation energy and the elastic constants. These parameters are iterated in such a way that small changes in C_{min} and β_0 improve the GSFE energy but don't significantly alter the elastic constant and the vacancy formation energy. If the latter are significantly changed, the iterations were not applied and we move to the next step.

they can be recovered in the next step. The six-step procedure depicted in Fig. 3.3 is repeated until no further improvement of the properties can be achieved. Similar parametrization strategies of an interatomic potential have been applied by Groh *et al.* [38] and Alam *et al.* [39] in bcc Li.

For a binary system, the same procedure is applied for the potential parameters. The cohesive energies and the equilibrium nearest neighbor distances are chosen from the binary reference structure. The bulk modulus of the reference structure was correlated with parameter α. The screening parameters are correlated to the GSFE energy and the elastic constants of the binary system, the substitutional and interstitial energies, the segregation energies, etc.

3.3.1 Automation of MEAM potentials parametrization

For the efficient parametrization of the interatomic potentials, 'Potitr' (https://github.com/alammasud/Potitr) software package has been developed. The tool is written in C and bash scripting. The key component of the package is the automation of material properties' calculations of a large number of material properties. Currently, the code can calculate material properties for fcc, bcc, diamond, and hcp crystal structures, as well as for many binary structures such as B1, B2, D1a, i4-mmm. The calculated properties are cohesive energies, elastic constants, surface energies for low index surfaces, point defect formation energies, GSFEs for different directions of shear and glide plane, and tensile stress for surface cleavage. All the properties are organized in subdirectories and the calculations are executed from a bash script. In the first step, cohesive energies and lattice parameters are calculated. Then and using these lattice parameters all other properties are evaluated.

3.4 Summary

In the present Chapter, the formalism of the 2NN-MEAM potential has been introduced. By performing a parametric study, the correlation of each parameter to the physical properties of the material has been identified and a correlation Table has been constructed. In this Table, the sensitivity of the material properties on the potential parameters has been quantified by varying each parameter. The parametric study revealed that the GB formation energies and the GSFEs are strongly correlated with the C_{min}. Increasing the value of C_{min}, the GB energy decreases while the GSFE increases. Furthermore, reducing the value of C_{min} results in smooth GSFE profiles, i.e., eliminates the discontinuities. A smaller value of C_{min} smoothly screens the many-body interactions. Parameter α was used to adjust the bulk modulus, B. A combination of the parameters β_0 and C_{min} was used to adjust the GSFE while the combination of parameters t_2, and $\beta 2$ was used to adjust the elastic constants, C_{ij}. Parameter A was used to iterate over the transitions energies of different crystal phases. Overall, in the present chapter, the parameterization methodology of a new 2NN-MEAM potential has been described. Based on this approach, 2NN-MEAM interatomic potentials for Si, C, 3C-SiC, Ni, Re, and NiRe alloys have been parametrized. These are described in Chapters 4, 5, and 6.

Chapter 4

Phase diagram of grain boundary facet and line junctions in Silicon

4.1 Introduction

The presence of point, line, and planar defects has a strong impact on the structural, mechanical, electronic, and optical properties of materials [43, 60–64]. For example, point defects play a prominent role in determining phase transformations, heat and electronic conductivity, as well as the electronic properties and the strength of materials [20, 65]. Line defects such as dislocation have a profound effect on the intrinsic ductility [62, 66] as well as on the electronic properties of materials [67–69]. 2D planar defects such as GBs also play a decisive role in determining the materials' mechanical, electronic, and optical properties [2, 64, 70–73]. These interfaces separate two grains of different orientations.

At the GBs the translational symmetry of the crystal is broken and the atomic structure at and near the boundary plane differs from the bulk crystal [74]. GBs have a critical role in determining a large variety of material properties: The presence of low coordinated atoms and/or highly distorted bonds may introduce deep states into the band gap of semiconductors. Deep states may also be introduced by the preferential decoration of the GBs by impurities. These interfaces are often preferred sites for segregation and formation of precipitations [75, 76]. The latter is also known to affect the mechanical properties of materials such as the solute induced embrittlement.

GBs introduce barriers to dislocation propagation. These barriers arise due to the misorientation and the disorder at and near the interface. Dislocations propagate when they experience a critical value of shear stress (Peierls stress) [77, 78]. However, when a dislocation reaches a GBs it experiences a barrier that hinders propagation and a pile up of dislocation is built at the GB. As the number of dislocations in the pile up increases, the repulsive forces among the dislocations reduce the barrier and dislocations can diffuse across the interface. Nevertheless, grains of smaller size induce smaller pile ups. Hence, larger shear strains are necessary to move the dislocation across the boundary. The inverse dependence of the yield strength on the grain size is called the Hall–Petch effect [2, 3] and is described by the following equation: If the average diameter of the grains is d, the yield strength, σ_y, is obtained as:

$$\sigma_y = \sigma_0 + \frac{k_y}{\sqrt{d}} \tag{4.1}$$

where σ_0 is the friction stress and k_y is the strengthening coefficient. Nevertheless, below a critical grain size (grain diameters typical in the order of a few tens of nm, i.e., nanocrystalline materials) the material gets softer. This inverse Hall–Petch effect arises from GB sliding which resolves the applied shear stress [79].

The aforementioned discussion indicates that both GBs and grain sizes play an essential role in the mechanical properties of the materials. However, as will be demonstrated in this Chapter, the properties of GBs such as the GB reconstruction can be strongly connected to and controlled by the microstructure in terms of grain sizes. In the present Chapter, the interplay between microstructure and GB properties is highlighted by investigating faceting in Si GBs.

4.1.1 GBs in Silicon

GBs in Si is of particular technological interest. More than 90% of the annual sales of solar cells are made of crystalline Si. Among these, more than half of the solar cells are made of mc-Si due to their low production cost and easier

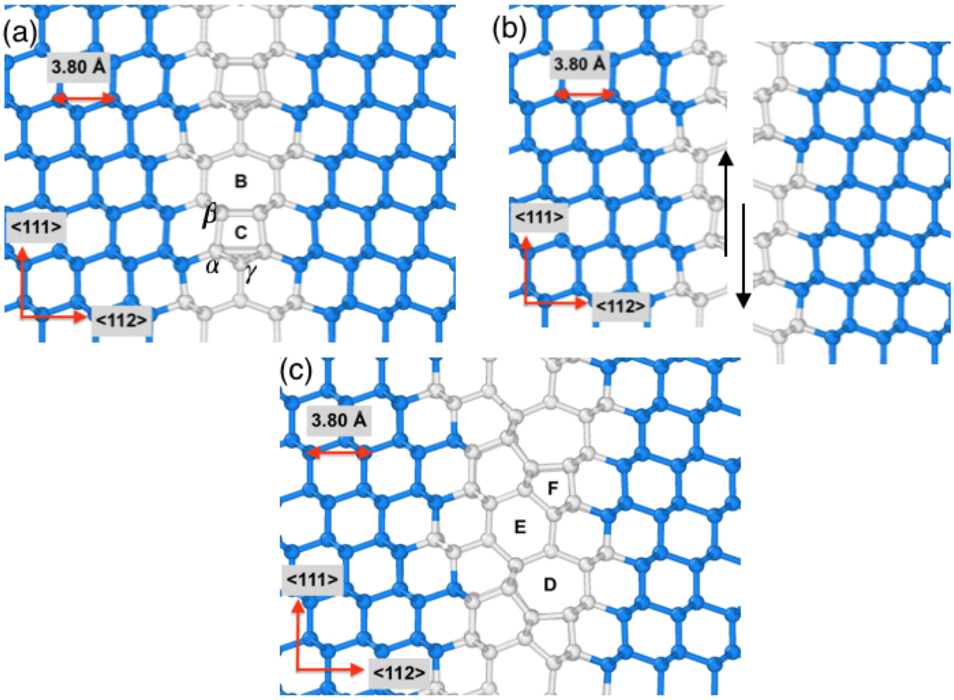

FIGURE 4.1: Schematic representation in ball and stick of the construction of the A-{112} (c) from the S-{112} GB (a). In (a), A and B represent the 5- and 7- atom rings, respectively. α and β indicate the atoms that has been removed to create the A-{112} GB. In (b) the applied shift of the one grain with respect to the other is shown. In (c) the 5-, 6- and 7- atom rings are presented by F, E, and D, respectively

fabrication process [80]. This mc-Si solar cell has a conversion efficiency of 12%–16%. Nevertheless, mc-Si has a density of 10^4 cm^{-1} GBs [81]. As has already been discussed, these planar defects as well as their interaction with impurities may introduce deep states into the fundamental bandgap. Due to the presence of over- or undercoordinated atoms and/or highly distorted bonds, GBs are often decorated or act as strong gettering centers for impurities such as O, C, Fe, or P [82]. The above mentioned states would act as recombination centers and reduce the efficiency of Si based devices [83].

Up to 80% of the GBs in Si are of type $\Sigma 3$. Experimentally these GBs are observed as dissociated into {111} and {112} facets [16]. Among these, $\Sigma 3$ {111} are the twin boundaries. They have very low boundary energies and are electrically inactive. $\Sigma 3$ {112} boundaries on the other hand have two stable/metastable states. The lower energy boundary is known as the asymmetric (A-Σ3 {112}) boundary and the higher energy boundary is known as the symmetric (S-Σ3 {112}) boundary [57, 84]. While the S-Σ3 {112} boundary is commensurate to the coincident site lattice geometry (see Section 4.2.1), the A-Σ3 {112} is characterized by the removal of two atoms per interface unit cell, and a shift of the one grain with respect to other (see Fig. 4.1). The S-Σ3 {112} [see Fig. 4.1(a)] has a five fold coordinated atom per 1 × 1 interface cell and highly strained bonds. These introduce deep states into the bandgap [21]. On the other hand, the A-Σ3 {112} [see Fig. 4.1(c)] has no deep states into the bandgap. Moreover, both boundaries show different site selectivity for solute segregation [16, 21].

Faceting is in principle described by Herring thermodynamic arguments and it is the result of the minimization of the interfacial free energy. As has already been mentioned, Σ3 boundaries in Si facet towards {112} and {111}. However, it is not clear if faceting is an intrinsic property of these boundaries, i.e., driven by the anisotropy in the boundary energies or it is solute driven, i.e., minimization of the interfacial free energy via preferential segregation of impurities at the S- or A-{112} facets or at their line junctions with the {111} facets.

Furthermore, at the {111} and A-{112} line junctions partial dislocations are introduced to accommodate the misfit and strain induced by the aforementioned rigid shift and the removal of atoms from the GB. This is expected to influence the energetics of faceted Σ3 GBs. Indeed, the interaction energy per unit length W_{12}/L between two parallel dislocations with Burgers vectors $\mathbf{b_1}$ and $\mathbf{b_2}$ is [85]

$$\begin{aligned}\frac{W_{12}}{L} = -&\frac{\mu\left(\mathbf{b_1}\cdot\xi\right)\left(\mathbf{b_2}\cdot\xi\right)}{2\pi}\ln\left(\frac{R}{R_o}\right)\\ &-\frac{\mu}{2\pi\left(1-\nu\right)}\left[\left(\mathbf{b_1}\times\xi\right)\cdot\left(\mathbf{b_2}\times\xi\right)\right]\ln\left(\frac{R}{R_o}\right)\\ &-\frac{\mu}{2\pi\left(1-\nu\right)R^2}\left[\left(\mathbf{b_1}\times\xi\right)\cdot\mathbf{R}\right]\left[\left(\mathbf{b_2}\times\xi\right)\cdot\mathbf{R}\right]\end{aligned} \tag{4.2}$$

where μ and ν are the shear modulus and Poisson ratio, respectively, $\mathbf{R}$ is the

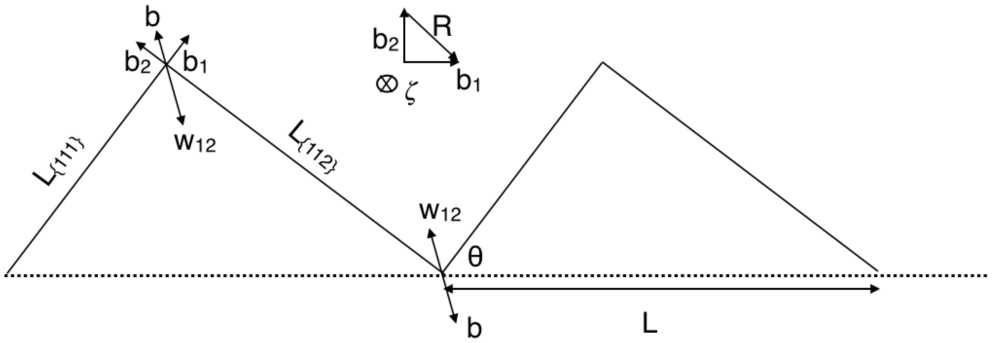

FIGURE 4.2: Schematic representation of a faceted GB in Si. The dashed line represents the flat Σ3 GB . {111} and {112} are the facets with $L_{\{111\}}$ and $L_{\{112\}}$ being their lengths, respectively. θ is the angle between the boundary plane and the {111} facets. w_{12} is the force acting on the line junction and b denotes the Burger's vector that predominantly accounts for discontinuity of the displacements along the {111} plane in the case of A-{112} facets (see text).

vector connecting the two dislocations, R_0 is the core radius, and ξ is the dislocation sense. In order to shed light on how these interactions influence the interfacial energetics let us consider the line junctions schematically demonstrated in Fig. 4.2. The dislocations at the junctions are of edge type and hence the first term on the right hand side of Eq. 4.2 vanishes. The other two terms comprise positive contributions to the interfacial energy. Furthermore, their magnitude depends on the geometric characteristics of the faceted GB, i.e., the lengths of the {111} and A-{112} facets.

The aforementioned discussion reveals that the faceting of Σ3 GBs in Si is governed by a complex interplay between facet energies, the presence of impurities as well as long range dislocation interactions. The interaction of impurities with these GBs is addressed in Chapter 5. In the present Chapter, we focus on the properties of faceted Σ3 GBs in pristine Si. Specifically, we derive a phase diagram that describes the facet junction reconstructions as a function of the geometric properties of faceted GBs, i.e., the inclination angle and the facet period.

In order to simulate faceted GBs and line junctions, large simulations cells are required such that the long-range strain interactions are explicitly included in the calculations. Simulations at the experimentally relevant length scale require simulations cells that consist of at least a few tens of thousands of atoms. Performing calculations on these large systems is beyond the scope of DFT due to limited computational resources. Therefore, a new MEAM potential is developed and employed to large scale atomistic calculations of Σ3 GBs in Si. DFT calculations have been conducted to construct a material's database to fit the potential. Section 4.2.1 discusses the coincidence site lattice concept and how this can be applied to construct simulation cells for GB atomistic calculations with periodic boundary conditions. In Sections 4.3 and 4.4 the aforementioned material's database and the MEAM potential parametrization are presented. In Section 4.5 insights into the energetics of GB faceting are discussed and based on that, a phase diagram of GB facet and line junction is constructed.

4.2 Modelling Grain Boundaries

In general, five macroscopic degrees of freedom are required to define a GB: Three degrees of freedom are necessary to identify the misorientation of the two adjacent grains and two degrees of freedom to define the boundary plane orientation. GBs are categorized into different classes according to their misorientation angle, the rotation axis as well as the symmetry across the boundary plane (see Fig. 4.3). A rotation axis in the boundary plane creates tilt GBs whereas if it is normal to the plane a twist boundary is formed. In all other cases, mixed GBs are created. Furthermore, if the two adjacent grains are mirror symmetric the GB is symmetric and asymmetric otherwise. Regarding the misorientation angle, the GBs are categorized into low and high angle GBs. Low angle GBs consists of a dislocations array. The largest misorientation angle of a low angle GB is defined by symmetry allowed minimum separation distance between the dislocations and it is less than $\lesssim 15°$ [86]. The large angle GBs can be further categorized as low Σ value Coincidence Site Lattice (CSL) boundaries and random GBs. The CSL is the superlattice

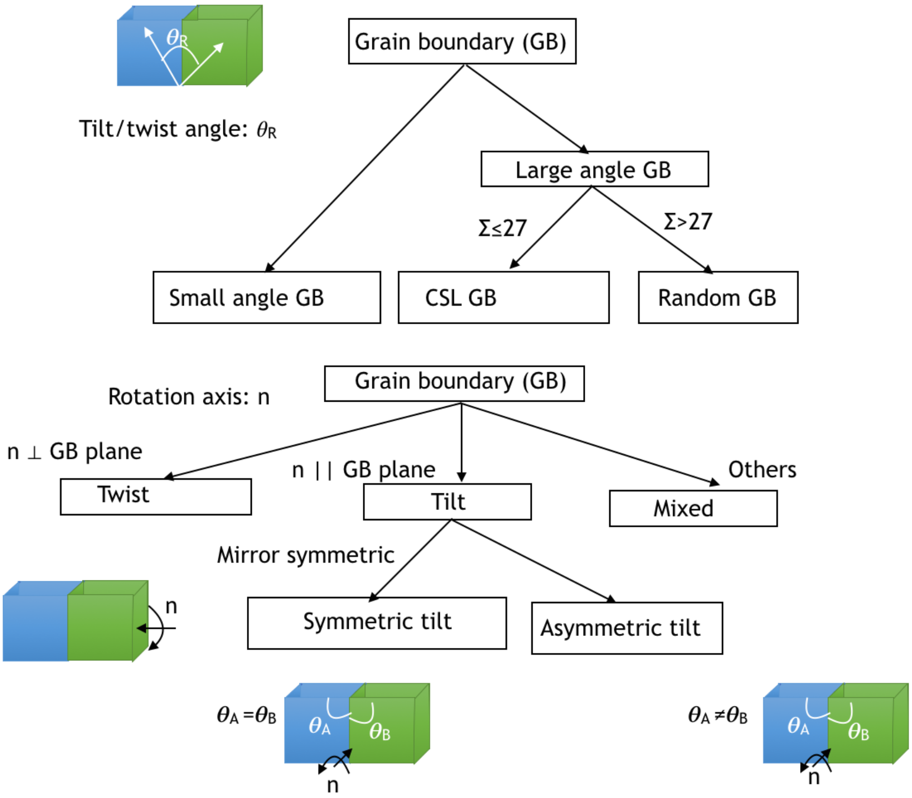

FIGURE 4.3: Classification of GB based on misorientation angle, GB plane orientations and mirror symmetry.

that consists of the interpenetrating lattices of the two adjacent grains when these coincide.

The concept of the CSL and its implication on GB energies and properties is described in detail in Section 4.2.1. Nevertheless, let us first provide a short discussion on the different geometries that can be applied to model a GB in atomistic simulations. A GB can be formed by bringing two crystals together across a plane with respect to a certain axis. One approach to model a GB is to implement a slab [57], or a cluster [87] geometry [see Figs. 4.4(b) and (c)]. In both cases, the supercell contains a single GB which is introduced in the middle of the cell. In the slab geometry [see Fig. 4.4(b)] periodic boundary conditions are applied only in the two directions parallel to the boundary plane. The thickness of the slab is large enough to decouple the GB from the two free surfaces. Furthermore, a vacuum slab with a thickness large enough to eliminate interaction between the free surfaces is also introduced if PBC is

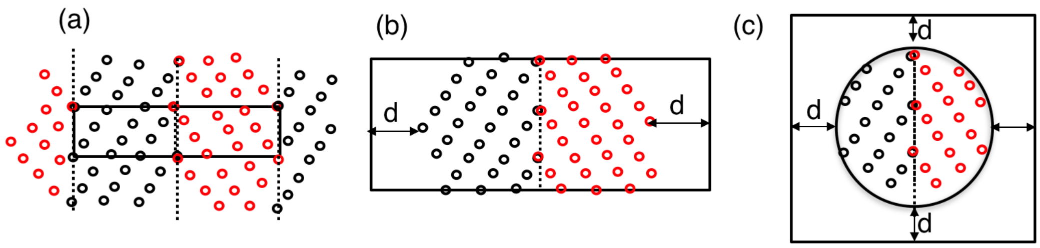

FIGURE 4.4: Schematic constructions of different approaches to model GBs. (a) Simulation cell with PBC in all directions. (b) Slab geometry. (c) Spherical cluster geometry. For the sake of clarity, only a single atomic layer cutting a sphere's equator is shown. The dashed lines indicate the GB/s and the rectangles the supercells. *d* is the vacuum thickness. Blue and red circles denote atoms at the opposite grains. In (a) the atomic geometry is extended beyond the supercell to highlight the PBCs.

inherent to the simulation code and/or the methodology, e.g., in plane wave based DFT calculations.

The slab and the cluster geometries have the advantage of containing a single GB in the supercell. Hence, there are no interactions between GBs to be considered. However, the presence of free surfaces and their interactions with the GB is a major drawback of these approaches. This can be addressed by the application of PBC in all directions. Nevertheless, the latter requires that the simulation cell is translationally symmetric in all directions. In order to restore translation symmetry, it is necessary to include a pair of compensating extended defects in our supercell. Although this is straightforward for special cases of high symmetry GBs, such as the Σ3 {111} GBs, the situation becomes cumbersome for low angle or arbitrary misorientation GBs or for GBs that are lacking mirror symmetry. Nevertheless, this can be circumvented by exploiting the translational symmetry of the CSL.

4.2.1 Coincidence Site Lattice

Fig. 4.5(a) shows the Moiré pattern formed by the interpenetrating lattices of two grains with the same origin and with one of the grains rotated relative to the other. For a rotation by an arbitrary angle, no points from both lattices coincide within a radius of tens of lattice constants from the rotation axis.

However, for certain special rotation angles, there will be some lattice sites from both lattices that coincide [see Fig. 4.5(b)]. The newly formed superlattice which consists of both interpenetrating lattices is the CSL. The CSL has a translational symmetry defined by two primitive vectors. The ratio of the volume of the unit cell of CSL to the volume of the regular crystal lattice is the Σ value of the CSL. It can be shown that the Σ values are always odd. The smallest Σ CSL, i.e., $\Sigma1$ corresponds to the perfect crystal.

Once the CSL, i.e, the Σ value is defined, the three macroscopic degrees of freedom associated with the misorientation of the two grains are uniquely defined. The remaining two degrees of freedom are associated with the GB plane. Due to the translational symmetry of the CSL, any two parallel CSL planes will correspond to two identical GBs. Thus, a supercell with a pair of equivalent GBs can be constructed [see Fig. 4.5(b)].

Apart from constructing supercells, the CSL is a valuable tool that allows drawing some general guidelines regarding the GB energies based on symmetry arguments. Nevertheless, symmetry alone is not adequate to describe GB energetics. In principle, a larger density of CSL points at the boundary plane, i.e., lattice points of the bicrystal that belong to both grains, increase the coherency at the interface. As has already been mentioned the Σ value is the relative size of the CSL unit cell with respect to that of the crystal lattice. Hence, small Σ values and CSL planes that maximize the density of CSL points at the GB are expected to result in lower boundary energies. Indeed, as has already been discussed, the tilt $\Sigma3$ {111} GB has smaller energy than the S-{112} as well as any other high index $\Sigma3$ GB. Fig. 4.6 shows the boundary energy against the misorientation angle of tilt Si GBs with the [110] rotation axis [88]. As can be seen the GB energy as a function of misorientation angle shows cusps. These cusps correspond to CSL GBs with a low Σ value.

4.3 Material database

The aim of the present study is to establish the phase diagram of the $\Sigma3$ GB line and facet junctions in Si. As has already been mentioned in Section 4.1.1

and revealed by Eq. (4.2) a prerequisite to investigate faceting in these planar defects is to correctly describe both the long range strain interactions between the line junctions and the highly strained core of the latter. DFT calculations can accurately describe both the long range interactions as well as the localized region of the cores. Nevertheless, DFT calculations are still restricted by their computational cost to systems consisting of $\approx 10^3$ atoms. However, in order to model GBs at the experimentally relevant length scale and/or correctly describe long range strain interactions, simulation cells consisting of $\approx 10^5$ atoms are required.

Semi-empirical interaction models allow treating systems consisting of a few million atoms. Furthermore, they can accurately describe the long range strain interactions [67, 89]. However, in order to perform large scale atomistic calculations of GBs using empirical potentials, the transferability of the interatomic potentials has to be evaluated in the first step. There is a large number of valence force fields (VFF) for Si. These include the Tersoff [90] and Stillinger-Weber (SW) [40] potentials, the bond-order potentials [41], and the MEAM potentials [42], to mention a few of the most widely applied VFF models. Nevertheless, common artifacts with VFF models for fcc, bcc, hcp, and diamond materials are that they yield incorrect ordering of surface energies and erroneous oscillations in the GSFE profiles [38, 39, 57].

In order to evaluate these potentials, a thorough investigation was conducted with a special focus on those properties that are expected to influence and/or control the properties of GBs. Specifically, the cohesive energies of the ground state diamond structure and the higher energy fcc, bcc, and β-tin crystal phases, the elastic constants, the charge neutral vacancy formation energies, the surface energies, and GSFE and GB energies have been considered. This investigation revealed critical shortcomings: Specifically, the above mentioned potentials fail to provide a quantitative and qualitative description of GSFE curves with respect to DFT. The GSFE is a material property that relates to dislocation cores and hence it constitutes a benchmark for the potential in describing the GB line junctions. Moreover, the smooth GSFE curve is a benchmark of the interatomic screening under shear conditions.

To address the aforementioned shortcomings, in the present work, a 2NN-MEAM potential to study GB faceting in Si was parametrized. MEAM potentials have been widely applied to study GB energetics and structural properties [57, 91–93]. A 1NN-MEAM potential for Si has been parametrized by Baskes (hereinafter referred as B-MEAM potential) [42]. This parametrization is used as the basis to parametrize the present potential. Furthermore, it was shown that it can correctly predict the thermal properties, i.e., thermal expansion coefficient, and melting temperature of Si [94].

4.3.1 Computational Details

Ab-initio calculations

As has already been described, the construction of the MEAM potential involves the fitting of the potential parameters. In order to achieve this a material's database was constructed and split into two groups. The first group includes properties that were used to fit and the second group properties to evaluate the potential. This database includes the following properties: Cohesive energies in the diamond, bcc, fcc, and β-tin, elastic constants, charge neutral vacancy formation energies, surface energies, GB energies of S-{112}, A-{112}, and the $\Sigma3$ {111} GBs, and GSFEs for different shear directions. The cohesive energies of diamond and β-tin, the elastic constants of Si, the {110} and {110} surface energies, and the GSFEs were used to fit the potential parameters. The other properties were used to benchmark the interatomic potential.

To build the database, DFT calculations have been employed. All *ab-initio* calculations were performed with the Vienna *ab-initio* Simulation Package (VASP) [95]. A plane wave cutoff of 450 eV was used and an equivalent $6 \times 6 \times 6$ Monkhorst-Pack k-point mesh for the bulk unit cell was used to sample the Brillouin zone. For the exchange and correlation, both the local density approximation (LDA) [96] and the generalized gradient approximation (GGA) [97] were used. The atomic positions were relaxed until the absolute value of the maximum force on all atoms was less than 0.01 eV/Å.

VFF calculations

All interatomic potential calculations were performed using the Large-Scale Atomic/Molecular Massively Parallel Simulator (LAMMPS) [98]. All the GBs were annealed using the Isothermal - Isobaric ensemble (NPT). The temperature of the systems was first raised to 700 K and cooled to 0.1 K within a time period of 750 ns. It was explicitly checked that an order of magnitude slower cooling rate does not affect the relaxed geometries and the GB energetics. The annealing was followed by a conjugate gradient relaxation until the energy change was smaller than 10^{-6} eV/atom or all atomic forces less than 10^{-6} eV/Å. During the atomic relaxations, the pressure was relaxed along the normal to the GB direction.

GB Vibrational Free energy

In order to evaluate the effect of the vibrational contributions to the free energy, the dynamical matrix for the S- and A-{112} GBs has been calculated. For a system with an extended defect large supercell sizes are required. However, (i) only the relative stability of the S-{112} with the respect to the A-{112} is of interest, and (ii) contributions to the force constant arising from deeper layers are the same for both interfaces and correspond to those of a bulk system [99]. To calculate the force constant matrix contributions from atoms within a slab of ≈5 nm from the interfaces have been considered. The dynamical matrix has been calculated with the small displacement method [100] using the present 2NN-MEAM potential and the vibrational free energy contributions have been calculated within the harmonic approximation [101, 102].

4.4 MEAM potential parametrization

For a unary system, the 2NN-MEAM potential consists of 16 parameters [53] (see Table 4.1). The correlation of the parameters to physical properties is intricate. Nevertheless, as has already been described in Section 3.3 some

TABLE 4.1: 2NN-MEAM potential parameters set for Si. The cohesive energy, E_c is in eV/atom and the equilibrium nearest neighbors distance, r_e, cutoff distance, r_c, smoothing distance, Δr, and the parameter, δ are in Å. The reference structure for Si is diamond. The parameters in bold are fitted in the present study and the others were adopted from NIST [106].

E_c	r_e	$\boldsymbol{\beta_0}$	β_1	β_2	β_3	α	$\boldsymbol{A}$	t_1	$\boldsymbol{t_2}$	$\boldsymbol{t_3}$	$\boldsymbol{C_{min}}$	C_{max}	r_c	Δr	δ
4.63	2.35	**4.5**	4.8	5.5	4.8	4.87	**0.80**	3.3	**3.60**	**-2.3**	**1.60**	2.8	4.0	0.1	**0.0**

parameters play a more dominant role in certain physical properties and a parametric study to systematically fit the parameters has been applied. The parametrization of the 1NN-MEAM potential for Si by Baskes is used as the basis for the present potential [42]. The cohesive energy, E_c, and the nearest neighbor distance, r_e were taken from experiment [103, 104]. The parameters α and δ which enter the Rose's universal equation of state were correlated to the bulk modulus, B, and the pressure derivative of the bulk modulus, B_p [105] [see Eqs. (3.16)-(3.18)]. In the present study, the value of δ is set to 0.0 as the pressure derivative of the bulk modulus is already in good agreement with DFT (4.15 vs 4.20) even with neglecting the δa^{*3} term [see Eqs. (3.16)-(3.18)].

The remaining parameters are the embedding energy scaling factor, A, the background electron density scaling parameters, t_i, the decay lengths of the atomic partial electron densities, β_i, the radial cutoff and smoothing parameters, r_c and Δr and the screening parameters, C_{min} and C_{max}. The C_{min} and β_0 parameters were used to fit the GSFE for the shuffle cut and the unstable stacking fault energies. During the parametric study, it was revealed that lowering the value of C_{min} removes the spurious oscillations in GSFE found in the previous 1NN-MEAM Si potential. Nevertheless, this increases the energies of $\Sigma 3$ {112} GBs with respect to the DFT calculated values. However, this doesn't impact the qualitative description of the GBs' properties. Moreover, it does not affect the description of the long range interactions of the line junctions. Parameters A and t_3 were used to fit the cohesive energies of diamond, fcc, bcc, and β-tin structures and parameter t_2 was fit to the elastic constants.

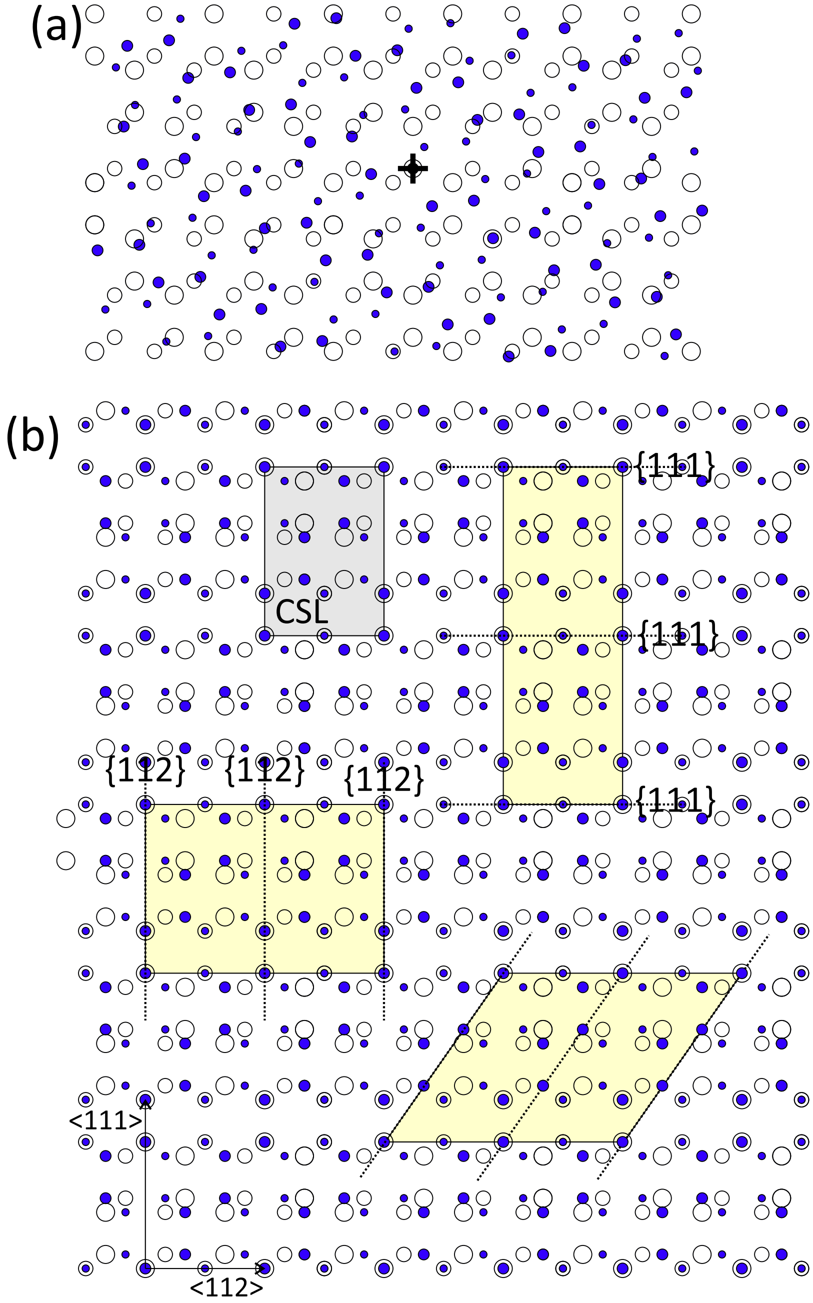

FIGURE 4.5: (a) Moiré pattern formed by two interpenetrating lattices denoted by open and filled balls, respectively. The plus sign indicates the position of the $\langle 110 \rangle$ rotation axis. The rotation of one lattice with respect to other produces no coincidence within a radius of tens of lattice constants from the rotation axis. (b) Moiré pattern of the $\Sigma 3$ CSL. The gray shaded area denotes the CSL unit cell. The yellow shaded areas indicate supercells containing a pair of low ({111} and {112}) and higher index GBs.

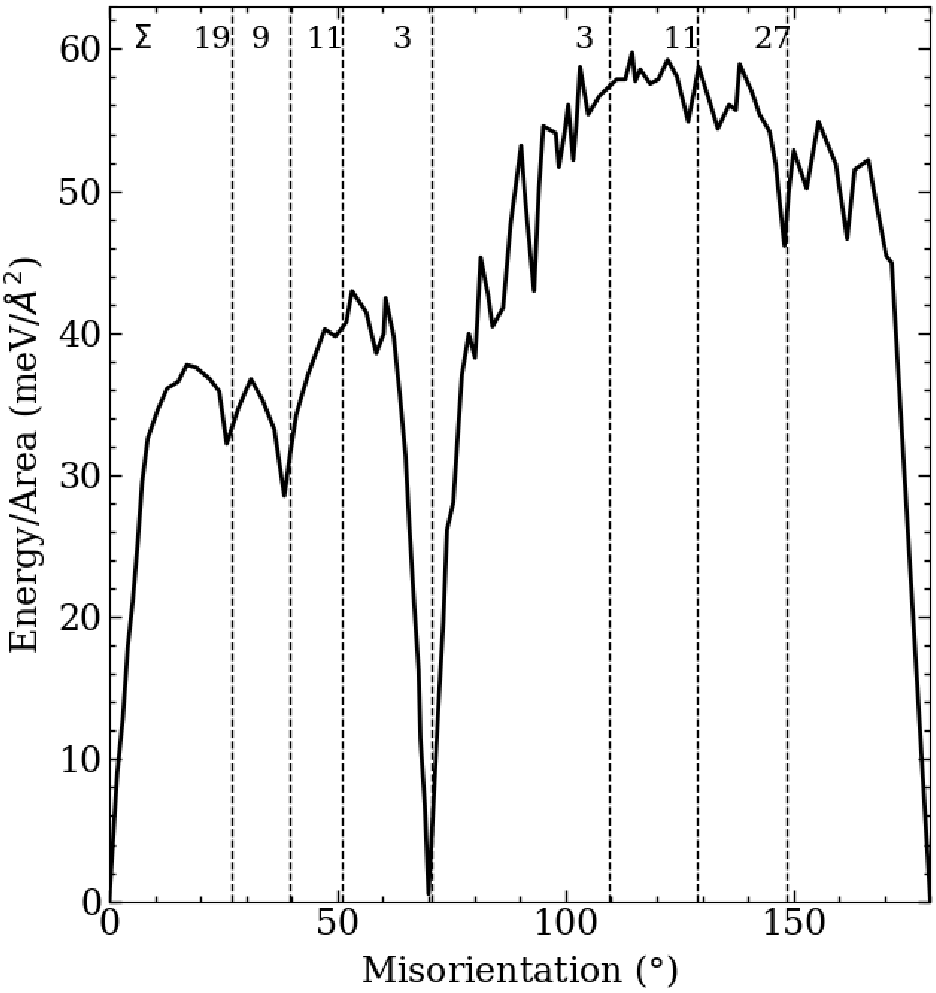

FIGURE 4.6: GB energy as a function of the misorientation angle in Si. The figure is adapted from Guziewski *et al.* [88].

4.4.1 Structural and elastic properties

TABLE 4.3: Properties of Si calculated using the present 2NN-MEAM potential (P-MEAM), 1NN-MEAM (B-MEAM) [42], bond order (E-Bond order) [41], and SW [40] potentials compared to DFT and experimental data. E_{dia} is the cohesive energy of diamond Si and ΔE denotes the cohesive energy differences between the diamond and the fcc, bcc, and β-tin Si structures in meV/atom. The lattice parameters a are in Å and the bulk modulus and elastic constants in GPa. The energies of the 1 × 1 (110), (110), and (111) surfaces are denoted as $E_{(100)}$, $E_{(110)}$, and $E_{(111)}$, respectively. The energies of the {111} and S- and A-{112} GBs are denoted as $E_{\Sigma3\{111\}}$, $E_{S-\Sigma3\{112\}}$, and $E_{A-\Sigma3\{112\}}$, respectively and are in meV/Å^2. The vacancy formation energy E_v is in eV.

		P-MEAM	B-MEAM	E-Bond order	SW	DFT	Experimental
diamond	E_{dia}	-4.63	-4.63	-4.628	-4.336	-4.75 ^{6}, -4.65 ^{4}	-4.62 ^{9}
	a	5.431	5.427	5.429	5.431	5.403 ^{1}, 5.43 ^{4}	5.431 ^{5}
fcc-dia	ΔE	771.21	468.89	652.24	396.28	449^{1}, 537.48^{2}, 566 ^{4}	
	a	4.282	4.20	3.85	4.14	3.817 ^{1}, 3.866 ^{2}, 3.885 ^{4}	
bcc-dia	ΔE	754.85	419.85	505.97	281.04	432 ^{1}, 519.69 ^{2}, 525 ^{4}	
	a	3.312	3.198	3.044	3.24	3.044 ^{1}, 3.087 ^{2}, 3.088 ^{4}	
β tin -dia	ΔE	613.75	320.86	423.14	199.68	212^{1}, 295.46 ^{4}	
	a	5.079	4.95	4.87	4.97	4.91^{1}, 4.97 ^{4}	
	c/a	0.553	0.545	0.527	0.56	0.55 ^{1}, 0.55 ^{4}	
Bulk modulus	B	96.53	96.89	98.38	101.18	96.19^{1}	99 ^{8}
	B_p	4.20	4.22	4.4	2.92	4.15^{1}	4.2 ^{8}
Elastic constant	C_{11}	162.40	162.44	169.33	151.42	160 ^{3}	166 ^{5}
	C_{12}	65.58	65.44	65.18	76.73	63 ^{3}	64 ^{5}
	C_{44}	77.74	73.25	60.41	56.44	82 ^{3}	80 ^{5}
E_v		3.45	2.94	3.13	4.33	3.64^{1}	
$E_{\{100\}}$		124.08	102.25	121.86	147. 02	147.93 ^{3}	132.95 ^{6}
$E_{\{110\}}$		94.17	118.10	76.47	103.96	104.86 ^{3}	94.25 ^{6}
$E_{\{111\}}$		78.69	102.56	62.35	84.88	107.36 ^{3}	76.77 ^{6}
$E_{S-\Sigma3\{112\}}$		69.89	66.50	59.75	59.38	42.24^{1}, 41.8 ^{7}	
$E_{A-\Sigma3\{112\}}$		55.3	50.52	51.01	43.16	24.86^{1}, 29.3 ^{7}	
$E_{\Sigma3\{111\}}$		0.40	0.0	0.0	0.0	0.42^{1}, 0.6 ^{7}	

^{1} and ^{2}denote DFT calculated properties employing LDA and GGA, respectively. In ^{3}Ref. [107],^{4}Ref. [108] LDA was employed and in ^{7}Ref. [21] GGA was used.

^{3}Ref. [107], ^{4}Ref. [108], ^{5}Ref. [109], ^{6}Ref. [110], ^{7}Ref. [21], ^{8}Ref. [104], ^{9}Ref. [111].

TABLE 4.4: Strain modes applied to calculate the three elastic constants, C_{ij}, of the diamond structure. The strain modes are depicted in the form $\{\epsilon_1, \epsilon_2, \epsilon_3, \epsilon_4, \epsilon_5, \epsilon_6\}$ where ϵ_i is the strain in the Voigt notation. $\Delta E/V$ is the strain energy density and δ is the strain variable.

	Strain configuration	$\Delta E/V$
1	$\{\delta, \delta, (1+\delta)^{-2}-1, 0, 0, 0\}$	$3(C_{11}$-$C_{12})\delta^2$
2	$\{\delta, \delta, \delta, 0, 0, 0\}$	$\frac{3}{2}(C_{11}$+$2C_{12})\delta^2$
3	$\{0, 0, \delta^2(4-\delta^2)^{-1}, 0, 0, \delta\}$	$\frac{1}{2}\, C_{44}\, \delta^2$

The cohesive energies and lattice constants of Si in the diamond, fcc, bcc, and β-tin crystal structures have been considered. For the calculations of the elastic tensor of the Si in the diamond structure, three different strain configurations have been applied (see Table 4.4). The elastic constants are determined by fitting the calculated energy densities $\Delta E/V$ for each of the strain configurations and small values of the strain parameter δ between -0.5% and +0.5%. The bulk modulus, B, and the pressure derivative of the bulk modulus, B_p, have been derived by fitting the calculated total energies, E, versus volume, V, data to the Murnaghan equation of state:

$$E(V) = E_0 + \frac{BV}{B_p(B_p-1)}\left[B_p\left(1-\frac{V_0}{V}\right)+\left(\frac{V_0}{V}\right)^{B_p}-1\right], \tag{4.3}$$

where V_0 and E_0 are the equilibrium volume and the total energy at this volume.

The results of the energetics, lattice and elastic constants are listed in Table 4.3. All the potentials considered, i.e., P-MEAM, B-MEAM, E-bond order, and SW, calculate the cohesive energy and lattice constant of the ground state diamond crystal phase in excellent agreement with the DFT calculations. The P-MEAM, B-MEAM, and E-bond order potentials provide an excellent description of the elastic constants as well. The SW potential provides an excellent qualitative description of the elastic constants, though the quantitative description is somewhat more inferior.

The P-MEAM systematically underestimates the cohesive energies with respect to the DFT calculated values of the higher energy crystal structures.

Nevertheless, it correctly predicts the sequence of the energetically most favorable structures. A good qualitative description of the cohesive energies of the higher energy crystal phases is provided by the B-MEAM, E-bond order, and SW potentials as well. The elastic constants of these crystal structures are generally overestimated by the P-MEAM and B-MEAM potentials.

Apart from the aforementioned structural and elastic properties, the charge neutral vacancy formation has also been considered. This has been calculated by removing an atom from a 3 × 3 × 3 bulk supercell. The structure was relaxed and the formation energies, E_v is calculated as

$$E_v = E_{tot} - (n-1)\mu_{Si} \tag{4.4}$$

where E_v is the vacancy formation energy. E_{tot} is the total energy of the system with the vacancy containing $(n-1)$ Si atoms and μ_{Si} is the chemical potential of bulk Si. The P-MEAM potential calculated formation energy is in excellent agreement with the DFT value (3.45 vs 3.64 eV, respectively). The B-MEAM and SW potentials severely under- and overestimate the E_v, respectively. The E-bond order potential also underestimates E_v by ≈0.5 eV.

4.4.2 Surface energies

The energies of the $\{100\}$, $\{110\}$, and $\{111\}$ surfaces have been included in the materials' database. In order to model the surfaces, slab geometries consisting of 10 unit cells along the normal to the surface direction with a vacuum of 10 and 1 × 1 surface unit cell were considered. The surface energy, E_{surf}, is calculated as

$$E_{\text{surf}} = \frac{1}{2A}\left(E_{\text{slab}} - nE_{\text{bulk}}\right) \qquad , \tag{4.5}$$

where E_{slab} is the total energy of the slab geometry containing n atoms, and E_{bulk} is the total energy per atom of bulk Si. A is the surface area and the factor 2 in the denominator accounts for the two symmetry equivalent surfaces in the slab geometry.

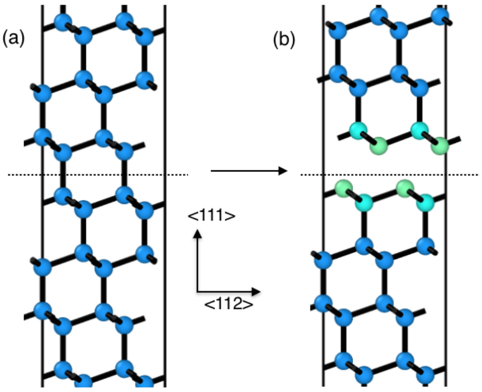

FIGURE 4.7: Schematic representation of supercell implemented to calculate the GSFE. (a) The supercell prior shearing. The dashed line indicates the sliding plane. (b) The upper half part of the cell is rigidly sheared along ⟨112⟩.

As seen in Table 4.3, all potentials underestimate the surface energies. Nevertheless, B-MEAM, E-bond order, and SW potentials predict that the {100} surface has the highest energy, in agreement with DFT calculations and experiments.

4.4.3 Generalized Stacking Fault Energy

The GSFE presents a challenging testbed for the interatomic potentials: The GSFE depends on the screening of the many-body interactions under shearing conditions. Inefficient screening at large shearing distances has been reported to result in oscillatory energy profiles [38, 39, 57]. Furthermore, according to the Peierls-Nabarro model, the GSFE profiles and the unstable stacking fault energies (USFE) are related to the width of the dislocation core [62, 77, 78, 112, 113]. The width of the dislocation core is inversely proportional to the USFE of GSFE. Hence, the GSFE profile constitutes a testbed for the accurate calculation of the relaxations of the atoms around a dislocation core. As has already been mentioned, faceting of the $\Sigma3$ GBs in Si involves the presence of partial edge type dislocations.

The slip system of the diamond crystal is similar to that of the fcc crystal. The GSFE was calculated for shear along ⟨110⟩ and ⟨112⟩ in the {111} plane [114–116]. To calculate the GSFE orthogonal parallelepiped supercells with their axis oriented along $\langle 110 \rangle$, $\langle 111 \rangle$, and $\langle 112 \rangle$ are formed. The supercells consisted of a 1×1 $\{111\}$ cell and 10 unit cells and a vacuum region of 10 Å thickness along the $\langle 111 \rangle$ direction. The bottom half of the slab was kept fixed while the upper half was rigidly shifted along the sliding direction (see Fig. 4.7). The excess energies per unit area with respect to no shear was used to calculate the GSFE, γ_i as following

$$\gamma_{x_i} = \frac{1}{A}(E_{x_i} - E_0). \tag{4.6}$$

Here, E_{x_i} is the total energy at displacement x_i, E_0 is the total energy without applied displacement and A is the area of the interface.

Fig. 4.8(a) shows the calculated GSFE for shear along $\langle 110 \rangle$. The E-bond order and Tersoff potentials show an abrupt increase at ≈0.45 and ≈0.55 displacement (in b^{-1} units, where b is the norm of the Burgers vector) and a plateau in-between these. This physically meaningless plateau is due to inefficient screening of interatomic interactions under shear conditions. The B-MEAM potential shows spurious local minima in the region of the unstable stacking fault. Although the SW potential provides a continuous GSFE profile with a single maximum at 0.5 displacement, it largely underestimates the USFE with respect to the DFT calculated value (56.63 vs 92.3 $\text{meV}/\text{Å}^2$, respectively). Following the Peierls-Nabarro model, this underestimation will result in the overestimation of the dislocation core width [62, 77, 78, 112, 113]. Nevertheless, the P-MEAM potential provides an excellent qualitative and quantitative description of the GSFE profile. It only slightly overestimates the USFE with respect to the DFT calculated value (99.95 vs 92.3 $\text{meV}/\text{Å}^2$, respectively).

Unlike the above discussed GSFE profile, the GSFE at the $\{112\}$ glide plane is characterized by a single hump at ≈ 0.5 of normalized displacement. This hump is a characteristic feature of the formation of a stable stacking fault and it is consistent with the formation of stable stacking faults in fcc and diamond materials. As with shear along $\langle 110 \rangle$, Tersoff and E-bond order potentials show abrupt increases and plateaus in the GSFE curves for shear along

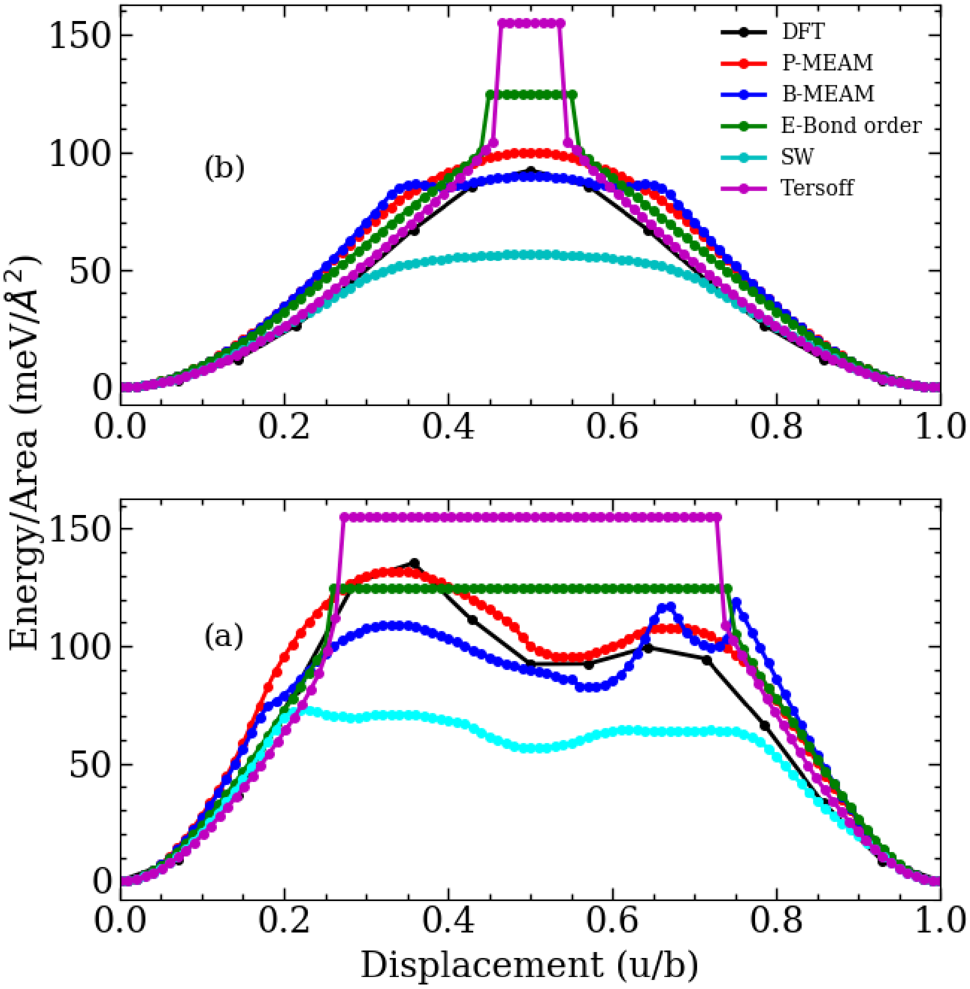

FIGURE 4.8: Generalized stacking fault energy as a function of the displacement along (a) ⟨110⟩ and (b) ⟨112⟩ in the {111} shuffle plane obtained from DFT, P-MEAM, B-MEAM [42], SW [40], E-bond order [41], and Tersoff potentials [90]

⟨112⟩ [see Fig. 4.8(b)]. Moreover, both B-MEAM and SW potentials fail to provide a qualitative agreement with the DFT calculations. Their calculated GSFE profiles show spurious oscillations. On the other hand, the P-MEAM potential provides an excellent qualitative and quantitative agreement to the DFT calculations. The P-MEAM calculated stable and unstable stacking fault energies are 95 and 107 meV/Å^2, respectively. The corresponding DFT calculated values are 92 and 99 meV/Å^2, respectively.

4.4.4 Low index Σ3 grain boundaries.

Let us now discuss the performance of the empirical potentials in describing the properties of low index Σ3 GBs in Si, i.e., the twin {111} and the S- and A-{112} tilt boundaries. To model these boundaries, supercells consisting of two mutually compensated GBs with a 2 × 2 interface unit cell were employed. The separation distance between the two interfaces was larger than 30 Å. Convergence checks indicted that this separation distance is sufficient to decouple the interactions between the two GBs. The energies of these boundaries are listed in Table 4.3. The GB energies, E_{GB}, were calculated as

$$E_{GB} = \frac{E_{tot} - n\mu_{Si}}{2A}, \tag{4.7}$$

where, E_{tot} is the total energy of the bicrystal, μ_{Si} is the chemical potentials of bulk Si, A is the interfacial area, and n denotes the number of Si atoms in the bicrystal. The factor 2 in the denominator accounts for the two GBs in the supercell.

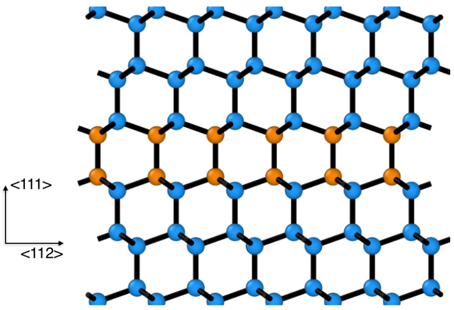

FIGURE 4.9: Ball and stick model of the Σ3 {111} GB in Si. Blue balls represent atoms in the diamond crystal and orange balls represent atoms in a hexagonal configuration.

A schematic representation of the twin boundary is shown in Fig. 4.9. This boundary is coherent and constitutes a hexagonal inclusion into the cubic lattice. The DFT calculated boundary energy of the Σ3 {111} is 0.42 meV/Å^2, i.e., it has negligible boundary energy. The atomic geometry of the twin differs from the bulk atomic geometry only at the second nearest neighbor distances. Therefore, valence force fields that do not include second nearest neighbor interactions and beyond calculate zero boundary energy. Indeed B-MEAM, SW, and E-bond order potentials calculate 0.0 boundary energy for the twin. Nevertheless, the P-MEAM potential includes second nearest neighbor interactions and calculates 0.40 meV/Å^2 boundary energy in excellent agreement with the DFT calculated value.

The S-{112} GB is shown in Fig. 4.1(a). This interface is commensurate to the $\Sigma3$ CSL and it consists of 5- and 7-atoms rings denoted as B and C in Fig. 4.1(a). Furthermore, it contains a five-fold coordinated atom per 1×1 interface cell denoted as γ in Fig. 4.1(a). This as well as the highly strained bonds at the interface introduce deep states into the fundamental bandgap [21]. The DFT calculated boundary energy of the S-{112} is 42.24 meV/Å^2. All considered valence force fields overestimate the GB energy. The P-MEAM calculated boundary energy is 69.89 meV/Å^2.

The A-{112} GB is formed from its symmetric counterpart by removing two atoms per 1×1 interface cell [denoted as α and β in Fig. 4.1(a)] and applying an upward shift along $\langle 111 \rangle$ and a leftward shift along $\langle 112 \rangle$ of the right grain [see Fig. 4.1(b)] [117]. The reconstructed A-{112} GB has a pattern of 5-, 6- and 7-atoms rings, denoted as F, E, and D in Fig. 4.1(c), respectively. Nevertheless, the interface consists of fully coordinated atoms only and has no deep states into the fundamental bandgap [21]. The DFT calculated energy of the A-{112} is by 14.6 meV/Å^2 lower than the S-{112}. Similar to the S-{112} all considered empirical potentials overestimate the energy of the A-{112}. Specifically, the boundary energy calculated by the P-MEAM potential is 55.3 meV/Å^2. Nevertheless, the GB energy difference between A- and S-{112} is in excellent agreement with the DFT results (17.38 meV/Å^2).

4.5 Results and Discussion

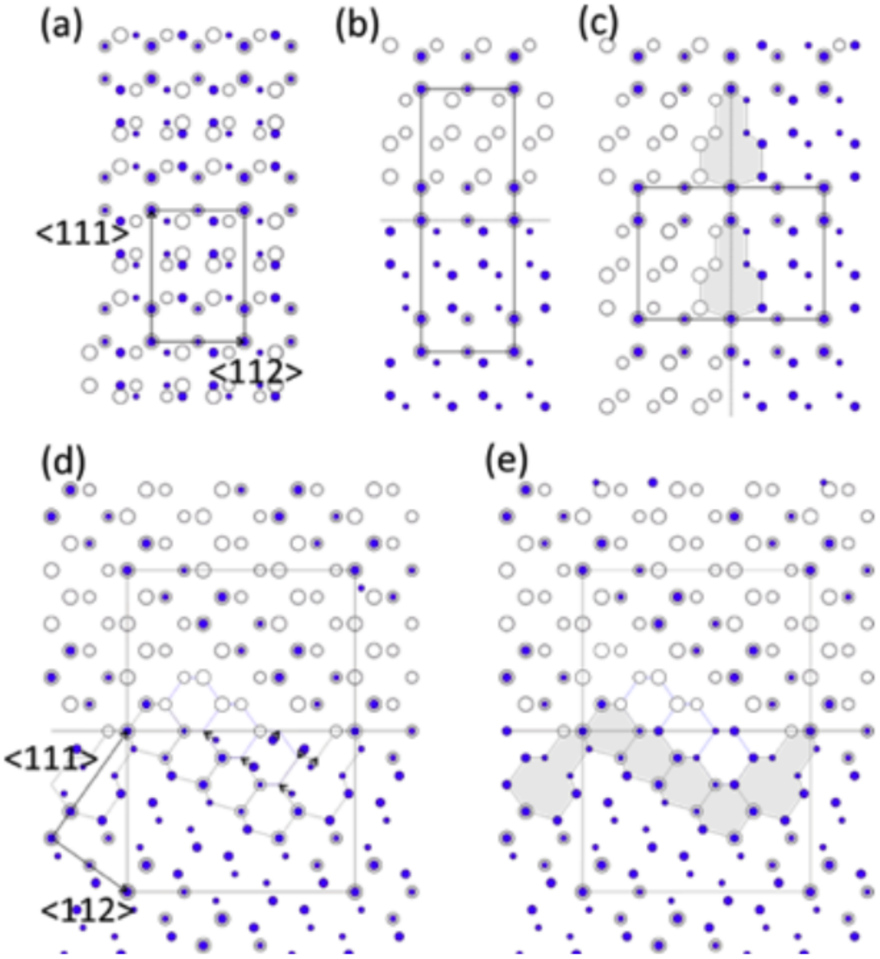

FIGURE 4.10: (a) Schematic representation of the Σ3 CSL of Si. The lattice points of two interpenetrating grains are denoted by filled and open circles. Large and small circles indicate atoms in the two different (110) planes. The CSL unit cell is indicated with the rectangle. (b) Supercell with two compensating Σ3 {111} GBs. (c) Σ3 {112} symmetric GB. The dashed areas highlight the 5- and 7- atoms ring pattern. (d) Σ3 GB at inclination angle of 35.26° prior annealing and relaxation. The arrows indicate the relaxation of the atoms from their initial positions at the CSL. (e) The relaxed GB shown in (d). The shaded highlight the {111} and S-{112} GBs formed upon relaxation.

As has already been discussed, five macroscopic degrees of freedom are required to define a GB, i.e., three degrees of freedom to identify the misorientation of the two adjacent grains and two degrees of freedom to define the boundary plane orientation. However, these degrees of freedom are not adequate to uniquely identify the lowest energy structures or reconstructions of the GBs. In addition to these, to achieve a complete macroscopic and microscopic description of a GB one has to consider the rigid translations of one grain with respect to the other as well as the density and position of atoms at the interfaces. Indeed, as it was demonstrated in Section 4.1.1 the ground state structure of the Σ3 {112} GB is formed by removing atoms from the boundary plane and rigidly shifting the one grain with respect to the other.

The aim of the present study is to investigate the energetics of Σ3 tilt GBs having the ⟨110⟩ rotational axis. Therefore, the three degrees of freedom that describe the misorientation of the one grain with respect to the other are fixed by the choice of the CSL, i.e., the Σ3. Moreover, one of the two degrees of freedom that define the boundary plane is fixed by the rotational axis. The remaining macroscopic degree of freedom is the inclination of the GB plane. The above mentioned discussion implies that in order to achieve an adequate description of the energetics and explore the high dimensional phase space of these GBs that consists of the boundary inclination, the rigid translations of the one grain with respect to the other, and the density and positions of the atoms at the boundary, the following have to be explicitly considered:

i Rigid translations of the one grain with respect to the other.

ii A grandcanonical ensemble for the thermodynamic description of the GBs, i.e., the GBs should be free to exchange energy and particles with a reservoir.

iii Apply a relaxation procedure for the atomic positions that it is able to overcome possible kinetic barriers.

Two different strategies were employed to calculate the GB energetics. At first, we created boundaries using the Σ3 CSL with the ⟨110⟩ rotation axis, i.e., all GBs are commensurate to the CSL. Four different inclination angles with respect to the {111} plane have been considered, (35.26°, 43.31°, 54.74°, and 70.53°). The inclination angles of 0° and 90° correspond to the twin and

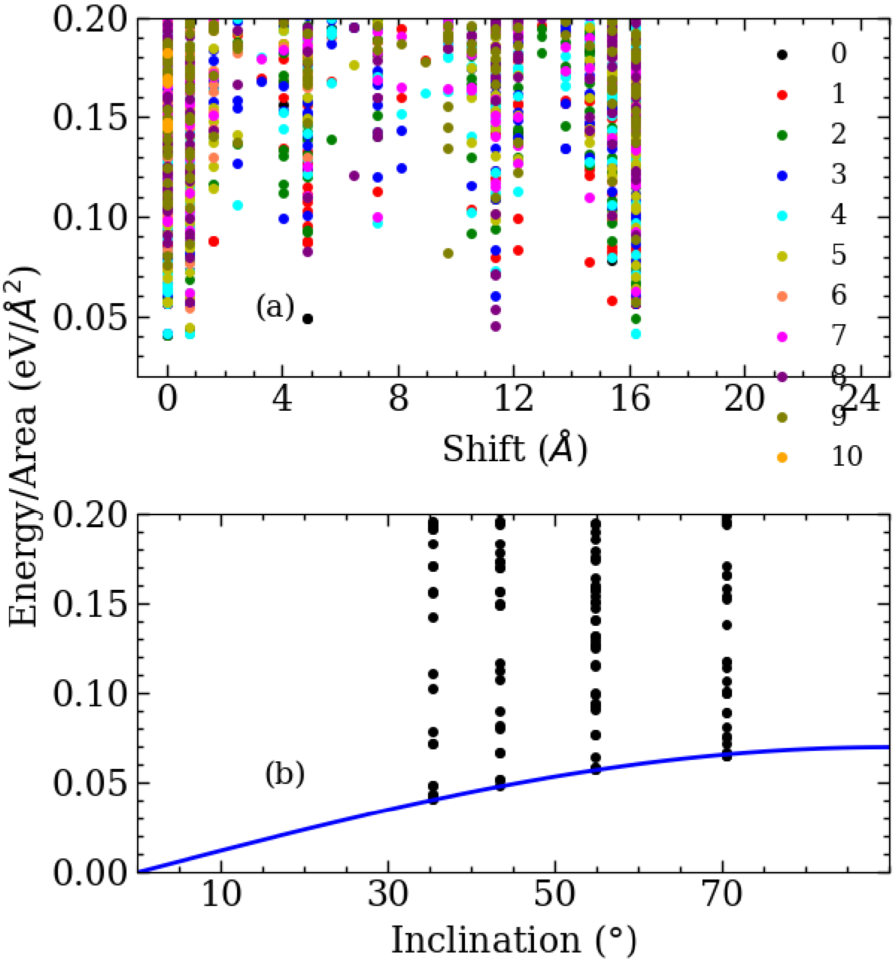

FIGURE 4.11: (a) GB formation energies of Σ3 tilt GBs inclined by 35.26° with respect to {111} as a function of the shift of one grain with respect to the other. For each shift up to 10 atoms were deleted randomly and the color coding represents the number of atoms deleted. (b) Blue line represent the energy using the equation Eq. (4.9). The black dots represent the energies obtained in the above process for four different inclination angles.

the S-{112} GBs, respectively. Taking advantage of the translational symmetry of the CSL, periodic boundary conditions were applied in all three directions and the simulation cell consists of two mutually compensating planar defects. The interface size was 1 × 1 in all cases.

The first strategy has the advantage that thanks to the translational symmetry there is no need to introduce free surfaces in the supercells. However, for high index boundary planes, i.e., for boundary planes with an inclination angle different than 0° or 90°, rigid translations of the one grain with respect to the other result in two symmetry inequivalent GBs in the supercell. In order to address this, in the second approach simulation boxes consist of a single GB bounded by two free surfaces parallel to and far from the GB plane. Nevertheless, PBC is applied in the GB plane. The thickness of the two adjacent grains was $\approx 100 - 150$ Å. Convergence checks revealed that this thickness is sufficient to decouple the interactions between the free surfaces and the boundary. In order to explore the degrees of freedom associated with the relative position of the two adjacent grains and the density and position of the atoms at the GBs a heuristic approach was implemented. Starting from the commensurate to the CSL GB structures rigid shifts of one grain with respect to the other along $\langle 111 \rangle$ and $\langle 110 \rangle$ were applied. The step width of these shifts were $a_x/20$ and $a_y/4$, where a_x and a_y are the CSL primitive vector lengths along $\langle 111 \rangle$ and $\langle 110 \rangle$, respectively (See Fig. 4.10(d)). Since we consider a grandcanonical ensemble, for each shift 0 to 10 atoms per 1×1 interface cell were randomly removed and the structure was subjected to simulated annealing (see Section 4.3.1). At the end of the annealing, conjugate relaxation was performed to calculate the final energy. The annealing effectively overcomes any kinetic barriers that may prevent the system to find its low energy structure. The aforementioned procedure was repeated ten times.

Fig. 4.11(a) shows the energy of the GBs with an inclination angle of 35.26° obtained with the above approach. The boundary energy was calculated using Eq. (4.7) and fixing the chemical potential of Si to the chemical potential of Si in bulk Si. The calculated interface energies vary from 0.04 eV/Å^2 to 5 eV/Å^2. For clarity the energy scale is restricted to the 0.00-0.20 eV/Å^2 range. The boundary with the lowest energy has no shift and no deletion of atoms. Hence, the lowest energetic structure is commensurate to the $\Sigma 3$ CSL.

Figs. 4.10(d) and (e) provide a schematic representation of the lowest energy structure before and after annealing and relaxation. Although we started from a flat boundary, the boundary dissociates into {111} and S-{112} facets. The final boundary is derived from the initial one by displacing six atoms per 1×1 interface unit cell. The displacement of these atoms is smaller than the bulk lattice constant [see arrows in Fig. 4.10(d)]. Hence, kinetic barriers that may hinder the transition into the ground state structure can be overcome by the applied annealing and atomic relaxation procedure. Analysis of the lowest energy structures for the other inclination angles, i.e., 43.31°, 62.06°, and 70.53°, reveals that all these GBs are intrinsically unstable against faceting toward {111} and S-{112} facets. Furthermore, the facet period is as small as a single interfacial primitive vector, i.e., they are unstable against nano-faceting.

Interestingly, although the A-{112} GB has smaller energy than the S-{112}, the former did not emerge as a nano-facet in all aforementioned cases. In general, faceting of GBs may be associated with dislocations and line forces. The dislocations arise from the rigid body translations of the two grains and the line forces from the different interface stress of the two facets at the junctions [64, 118]. As has already been discussed in Section 4.1.1, the A-{112} GB is constructed by rigidly shifting the one grain with the respect to the other both parallel and normal to the boundary plane directions. Therefore, at the {111} and A-{112} line junctions partial dislocations are introduced to accommodate the misfit and strain induced by the aforementioned rigid shifts as well as by the removal of atoms from the GB (see Fig. 4.1). The energy of a faceted boundary, $\gamma(L)$, includes contributions from the two facets, the core energy of the line defects at the junctions, and the long range strain interactions between the line junctions [64, 118]:

$$\gamma(L) = \gamma_{\mathrm{f}} + \frac{A}{L}\mathrm{Ln}\left(\frac{L}{B}\right) + \frac{C}{L} \qquad , \tag{4.8}$$

where L is the facet period (see Fig. 4.2) and the last two terms on the right side are the contributions from the long range strain interactions and the core energies. A, B, and C are constants that depend on the elastic constants, the geometry of the faceted GB, i.e., faceting length L and inclination angle θ, and the width of the cores. γ_f denotes the energy contribution of the two facets and is written as

$$\gamma_f = \frac{\gamma_{\{111\}} + \gamma_{\{112\}}\tan(\theta)}{\sqrt{1+\tan^2(\theta)}} \qquad , \tag{4.9}$$

where $\gamma_{\{111\}}$ and $\gamma_{\{112\}}$ are the energies of the flat {111} and {112} GBs.

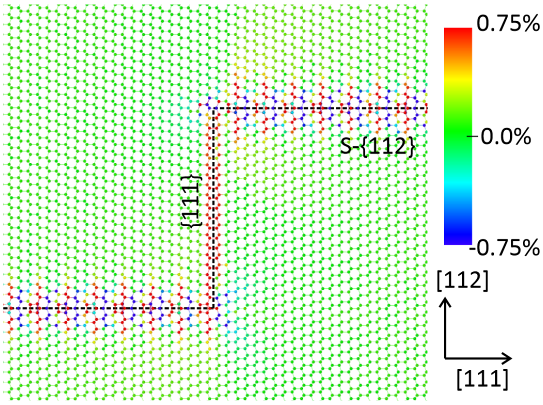

FIGURE 4.12: ε_{xx} component of the strain tensor obtained from a faceted junction consisting of {111} and S-{112} facets.

Using Eqs. (4.8) and (4.9) and for $\gamma_{\{112\}}$ the energy of the S-{112} and fixing parameters A and C to zero, the energies of the faceted GBs are plotted as function of the inclination angle in Fig. 4.11(b) . As can be seen, the calculated lowest energy faceted GBs coincide with the energy predicted by Eqs. (4.8) and (4.9). This indicates that faceting towards {111} and S-{112} is driven merely by the anisotropic GB energies and energetic contributions by line defects are negligible and/or cancel out. The absence of long range strain interactions is confirmed by the calculated strain distribution at and around a faceted GB (see Fig. 4.12): As can be seen the strain has finite values near and at the {111} and S-{112} facets and it is negligible a few lattice constants away from the planar defects. The tensile strain at the twin boundary is attributed to the larger interatomic distance in hexagonal Si.

The atomistic calculations plotted in Fig. 4.11 are on supercells containing rather small size interfaces, i.e., $n \times m$. Therefore, the energies of GBs faceted towards {111} and A-{112} facets are dominated by the core energies and interactions between the line junctions [see Eq. (4.8)]. In order to evaluate the effect of these interactions on the faceted GB energies, large supercells consisting of $\approx 10^5$ atoms and a pair of mutually compensated GBs have been employed. These faceted GBs have been constructed by imposing an inclination of the {112} boundaries toward {111}. Furthermore, for each inclination angle, facet periods up to ≈ 350 Å have been considered and the separation distance between the two planar defects was at least 100 Å. Convergence checks showed that this distance is more than sufficient to decouple the GBs.

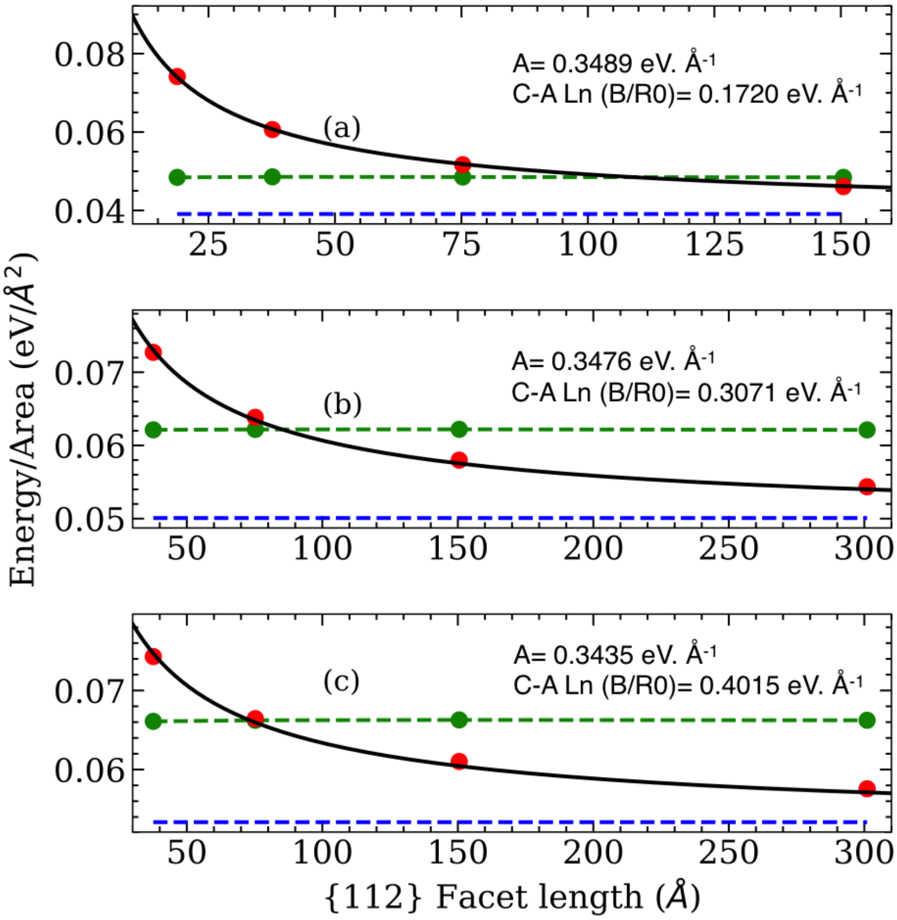

FIGURE 4.13: Formation energies of GBs as a function of facet length for S- (green circles) and A-{112} (red circles) facets with inclination angles (a) 43.31° (b) 62.06°, and (c) 70.53°. The continuous line represents the values obtained by fitting the Eq. (4.8) and the blue dashed line represents the energies at the asymptotic limit. Inset gives the fitting coefficients.

The boundary energies as function of the facet period for inclination angles 43.31°, 62.06°, and 70.53° are plotted in Figs. 4.13(a), (b), and (c), respectively. These inclination angles correspond to {111} over {112} facet lengths ratios of 1.5, 0.75, and 0.5, respectively. In agreement with the above mentioned finding, the energies of boundaries consisting of {111} and S-{112} facets are independent of the facet period. Nevertheless, in the case of A-{112} facets, the boundary energies decrease with the facet length. Furthermore, they asymptotically converge to the γ_f term [see Eqs. (4.8) and (4.9)]. This is consistent with the presence of extended defects at the line junctions which induce long range strain interactions. Indeed in Fig. 4.14(a), the ε_{xx}

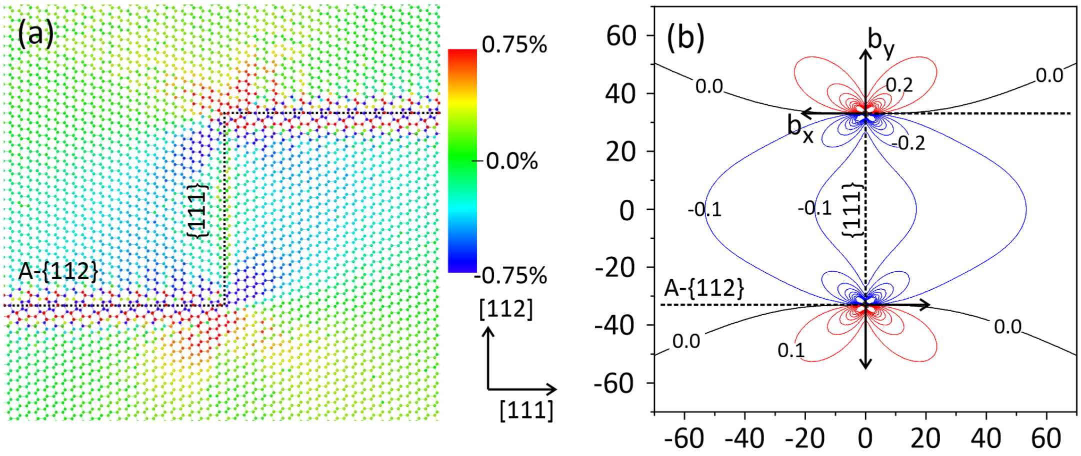

FIGURE 4.14: (a) ε_{xx} component of the strain tensor as obtained from a faceted junction consisting of {111} and A-{112} facets. (b) ε_{xx} elastic strain field derived by elasticity theory for a pair of mutually compensated edge type dislocations with Burgers vectors $|b_x| = 1.743$ Å and $|b_y| = 1.03$ Å placed at the two junctions. The horizontal and vertical axes are distances along $\langle 111 \rangle$ and $\langle 112 \rangle$ in Å. The value of each contour line differs from its immediate neighboring lines by ±0.1%.

strain component is plotted at the region of a facet junction consisting of {111} and A-{112} facets. In contrast to the case of S-{112} facets (see Fig. 4.12) the strain is long ranged. Furthermore, around the line junctions, two regions of compressive and tensile strain can be seen. This re-samples the situation of two edge type dislocation with opposite Burgers vectors sitting on the two line junctions. In Fig. 4.14(b) the ε_{xx} component of the strain field calculated by elasticity theory for two mutually compensated edge dislocations placed at the line junctions and with Burgers vector components $b_x = \pm 1.743$ Å and $b_y = \mp 1.03$ Å is plotted, where x is along $\langle 111 \rangle$ and y along $\langle 112 \rangle$. These values equal the rigid shifts applied along $\langle 111 \rangle$ and $\langle 112 \rangle$ to construct the A-{112}, respectively. There is both quantitative and qualitative agreement between the strain fields calculated by atomistic calculations and elasticity theory.

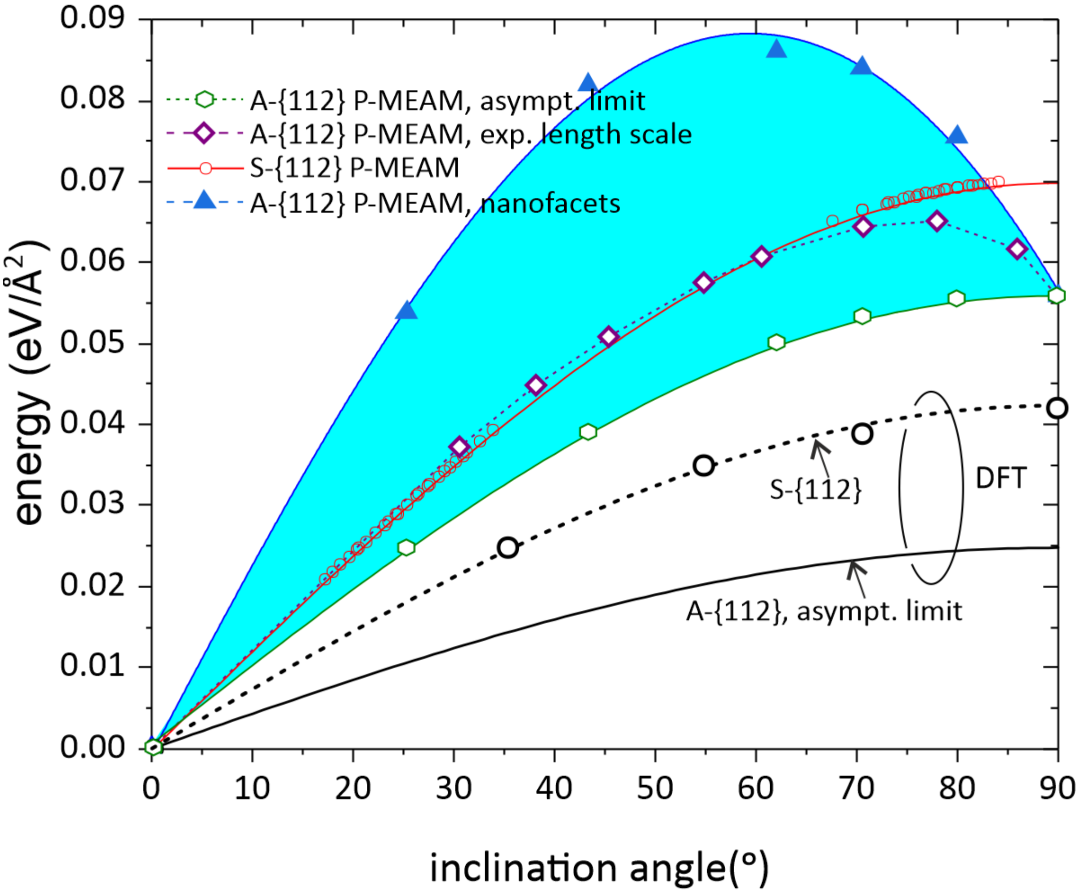

FIGURE 4.15: Boundary energies of faceted GBs as function the inclination angle. The black continuous line is the DFT values for A-{112} facets at asymptotic limit, black dashed line is the DFT values of S-{112} facets. The area between the red line and green line indicates the energy range (i.e., from the geometrically minimum facet length to the limit of infinite facet length) of faceted GBs with A-{112} facets.

4.6 Phase Diagram

An important outcome from Fig. 4.13 is that at short facet periods the faceted GBs with S-{112} facets are energetically favorable. However, as the facet period increases there is a transition from S-{112} to A-{112} facets. In order to shed light on these transitions in Fig. 4.15 the energies of faceted GBs for a wide range of facet lengths and all the range of inclination angles are plotted. The light blue shaded area represents the energy range of faceted GBs consisting of A-{112} facets with the smallest symmetry and geometrically allowed length, i.e., nano-facets, to the asymptotic limit of infinitely long facets. The red curve denotes the energy of GBs with S-{112} facets. As can be seen, for inclination angles larger than ≈ 80° A-{112} is the energetically favorable facets for all facet lengths. Therefore, in this range of high inclination angles, Σ3 GBs with the ⟨110⟩ rotation axes are favorable to facet towards {111} and A-{112} facets. Furthermore, under conditions of thermodynamic equilibrium, the facet length is restricted only by boundary conditions applied by the microstructure and the grain size. Nevertheless, for lower inclination angles the phase of the {112} facets depends on the facet length as well: Smaller facet lengths favor S-{112} facets and larger facet lengths their asymmetric counterparts. Interestingly at the experimentally relevant length scales, the A-{112} facets are energetically favorable for inclination angles larger than ≈ 55° while for smaller inclination angles the two facet junction reconstructions are energetically degenerate.

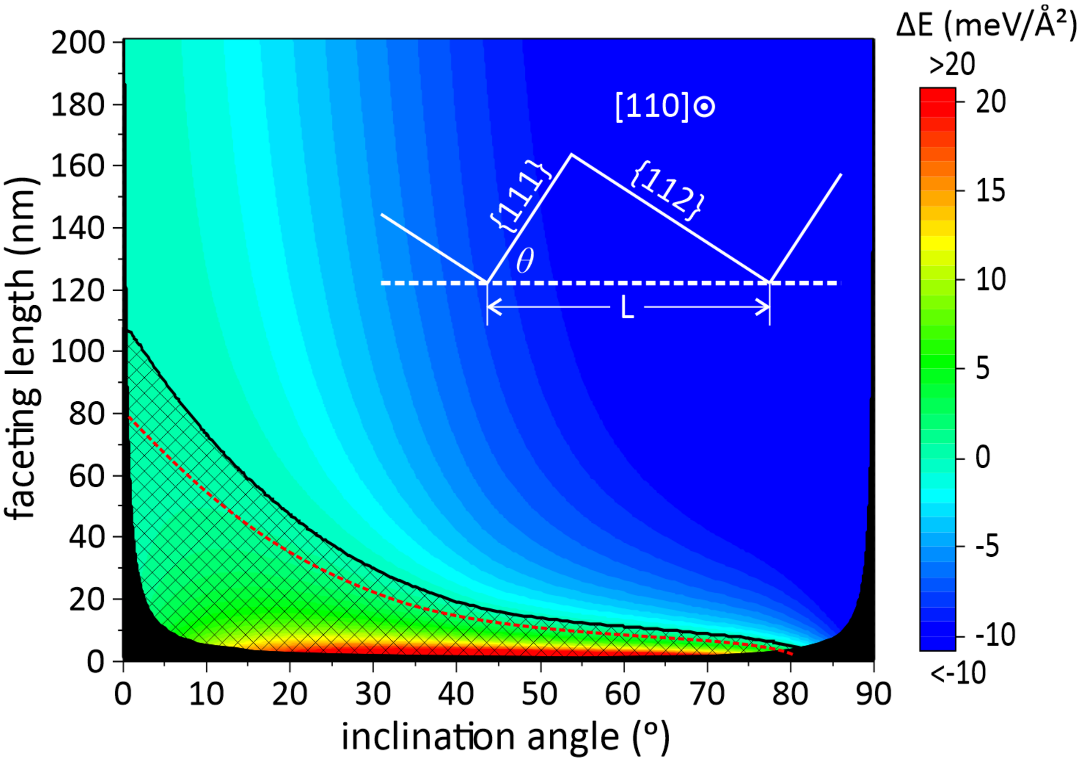

FIGURE 4.16: Energy difference of S-{112} + {111} and A-{112} + {111} boundary as a function of inclination angle. The solid black curve indicates the boundary between GBs having an A- or S-{112} facet. The dashed area denotes the stability region of GBs with S-{112} facets. The black curve shows the boundary line when DFT calculated energies of flat (unfaceted) {112} GBs are considered. The black shaded area marks the region of geometrically not accessible facet periods and inclination angles.

In Fig. 4.16 the boundary energy difference $\Delta\gamma$ between faceted GBs with A- and S-{112} facets are plotted against the inclination angle and the facet length. Vibrational contributions to the free energy have not been included since they have a marginal impact on the calculated energy differences. Specifically, at T=1000 K the energy difference between A- and S-{112} GBs changes by $\approx$ 2 meV/Å^2 with respect to T=0 K. This shifts upward the phase boundary line by $\approx$2 nm at the inclination angle of 45.

The phase diagram in Fig. 4.16 clearly demonstrates that Si GB faceting is not merely driven by the anisotropy in the boundary energies. Instead, the two geometrical characteristics of the facet junctions, i.e., the inclination angle and the facet period, are key parameters, alongside the GBs energies, that control the facet and line junction reconstructions. These geometrical characteristics depend on and can be controlled by the microstructure. For instance, large grain sizes that allow for large facet lengths will shift the system in the upper part of the phase diagram, i.e., will stabilize A-{112} facets. Nevertheless, a key outcome is that higher energy metastable GB reconstructions can be stabilized by thermodynamics instead of kinetics when they constitute the facets at line junctions.

The transition between the metastable S-{112} and the lower energy A-{112} phases has important implications on (i) the electronic properties of the multi- and nano-crystalline Si, (ii) impurities segregation at the facets, and the line junctions, and (iii) on the GB mobility. As has already been discussed in Section 4.4.4, S-{112} GBs introduce deep states into the fundamental bandgap, while the A-{112} interfaces are free from any intragap states [21]. Since the deep states are detrimental to the electronic properties and the efficiency of devices based on mc-Si, material growth and/or processing should be applied that shifts the system into the upper part of the phase diagram.

The strain distribution around the A- and S-{112} shows different periodic patterns that consist of alternating compressive and tensile regions [see Figs. 4.12 and 4.14(a)]. Specifically, in the S-{112} GB the strain extends deep into the bulk like region. Moreover, this indicates that strain induced segregation of impurities at Σ3 facets will depend strongly on the inclination angle and the facet period. Nevertheless, in the next chapter, the segregation of homovalent impurities at Σ3 line junctions will be discussed in detail.

Disconnections, i.e., GB line defects that have both step and dislocation character are key microstructural features that play a key role in the shear coupled migration [119]. In twin boundaries in Si, the disconnections correspond to {112} steps at the {111} boundaries. Geometrically, this corresponds to small facet periods or small inclination angles. Therefore, the steps at the disconnections would consist of S-{112} and hence there will be no GB dislocations at the line junctions. Therefore, the shear coupled migration of twins in Si, will not be affected by the presence of other extended lattice defects.

4.7 Summary

Σ3 tilt GBs with $\langle 110 \rangle$ rotation axis constitute up to 80% of GBs in Si and hence a system of GBs with special fundamental and technological interest. These boundaries are commonly observed to facet toward the low index {111} and {112} boundaries. However, the driving force that causes faceting in this system is still an open issue. This is the key question that the present chapter addresses.

Two different metastable reconstructions exist for the {112} GBs, the A- and the S-{112} reconstructions. Faceted GBs consisting of {111} and the lower energy A-{112} facets are associated with partial edge type dislocations at the line junctions. The latter renders the description of faceting by atomistic calculations cumbersome: Both long range strain interactions, as well as the highly strained but localized region of the cores have to be accurately described by the model for the interatomic interactions.

In order to investigate and correctly describe the different length scales associated with GB faceting, we combined DFT and 2NN-MEAM potential calculations. In the first step, a thorough evaluation of widely applied valance force fields for Si has been performed. This evaluation revealed that none of these potentials can correctly describe the GSFE profiles. The GSFE depends on the screening of the many-body interactions under shearing conditions and hence it constitutes a challenging testbed for the interatomic potentials. Therefore, in the next step, a new 2NN-MEAM potential for Si has been developed. This potential has been fitted using GSFE profiles, surface and interface energies, elastic constants, and structural transition energies of Si. The parametrization of the potential was accomplished by employing the iterative method described in Section 3.3.

Employing the newly developed 2NN-MEAM potential, we have studied the energetics, structure, and strain of flat and faceted $\Sigma3$ tilt GBs in Si with the $\langle 110 \rangle$ rotation axis. The present 2NN-MEAM potential provides an excellent qualitative and a very good quantitative description of the energetics of $\Sigma3$ GBs in Si. These calculations revealed that faceting is intrinsic to these GBs. Furthermore, a phase diagram has been constructed which indicates the energetically most favorable facet and line junction reconstructions as a function of the facet length and inclination angle. This diagram also reveals that the properties of the faceted GBs are controlled by the interplay between GB energies and long-range strain interactions. Specifically, it shows that at low misorientation angles or at small facet periods long-range strain interactions dominate, and S-$\{112\}$ facets are favored. However, at large facet periods and large inclination angles the weaker strain interactions are compensated by the low energy of the A-$\{112\}$ facets.

The significance of the GB phase diagram goes beyond mc-Si. Specifically, it highlights the connection of faceting with materials' microstructure. A common perception is that GB faceting is driven merely by the anisotropy in the GB energies. However, in this chapter, it is demonstrated that the higher-energy GBs can be stabilized by thermodynamics rather than kinetics when these constitute facets at line junctions. This further highlights the crucial role of microstructure on the GB properties: Microstructural parameters such as the grain size, control the geometric properties of faceted GBs and hence the reconstruction of the facet and line junctions. The latter has important implications on the electronic properties, mobility as well as on impurity segregation and/or gettering potential of the GBs. The interplay between strain and impurity segregation at facet and line junctions in Si will be addressed in the next Chapter.

Chapter 5

Strain-Induced Asymmetric Line Segregation

5.1 Introduction

In the previous Chapter, the properties and mechanisms of faceting of Σ3 Si GBs have been investigated. It has been demonstrated that the faceting of GBs in pristine, i.e., without impurities, Si is the result of a complex interplay between facet energies and long range strain field interactions. However, there is a strong interaction between impurities and GBs which is governed by the driving force to achieve an equilibrium distribution of impurities between the GB and bulk which minimizes the free energy of the system [120]. This strongly impacts the mechanical and electronic properties of materials [73, 120–123]. For example, decoration of GBs by solute atoms may lead to strengthening or weakening of the material [72, 124–126]. Impurity segregation at Si GBs is of particular interest due to its technological importance.

C, P, As, Fe, Cu, and O impurities are commonly present in mc-Si [127–131]. These impurities may result in diode breakdown, thermal degradation [132], or create a low resistance path for electrical conductivity (shunt) [80]. Furthermore, they may introduce deep defect states in the fundamental band gap [21]. For example, it has been shown that interstitial Fe introduces deep defect states in the electronic structure of Si GBs [21]. These states act as recombination centers and reduce the minority carrier lifetime and the solar cell efficiency [20, 82].

Moreover, it has been shown that O impurities form oxide precipitates in mc-Si, which alone is responsible for ≈5% reduction of solar cell efficiency [133] caused by the reduction of the minority carrier lifetime [129, 133]. Cu and Ni impurities also play a detrimental role in Si electronic devices [127] while decoration by P has been proposed to have a positive effect by increasing the lifetime of the minority carriers [128]. First principles calculations highlighted the correlation between the electronic structure of pristine GBs with the impurities' segregation energies at these interfaces: GBs that introduce deep states into the bandgap due to under- or over-coordinated atoms were found to attract P and As impurities [134]. Nevertheless, the segregation of impurities and their impact on the electronic properties of Si depend strongly on the orientation and the character of the GBs. For example, it has been demonstrated by employing 3D atom probe tomography, that the segregation and recombination activity of Fe, Cu, C, and O impurities at Si GBs predominantly take place at high angle GBs and not at the $\Sigma\,3$ $\{111\}$ twin boundaries [18].

The above described interactions between GBs and solutes have been extensively investigated and described in terms of the Langmuir-McLean theory where the segregation of a monolayer or submonolayer coverage is taking place without any structural changes and atomic interactions of the solute atoms. Nevertheless, recently it has been demonstrated that GBs can also transform between different states, termed complexions or interphase phases (see Ref. [1] and refs therein). Recently a unique segregation mechanism at Si GBs, that goes beyond classical McClean theory, has been reported [16]. More specifically, it has been observed that solute segregation occurs at the linear junction of faceted GBs rather than at the averaged planar structure of the GB or the GB facets as shown in Fig. 1.1. Moreover, solutes such as C, and Fe, preferentially segregate at one of the two facet junctions leading to an asymmetric segregation pattern of solute segregation.

In the present chapter, the mechanisms underlying the aforementioned asymmetric segregation of C impurities at faceted Σ3 GBs in Si are investigated. In particular, atomistic simulations have been conducted to investigate the interplay between GB facets, line junction core structures, long range strain interactions, and solute segregation. To study the C segregation mechanism, we have developed an interatomic potential for C and 3C-SiC. For Si, we have used the potential that has been developed in the previous Chapter. The newly developed potentials were evaluated for their transferability against non-fitted properties such as segregation energies, solute binding energies, GB energies, and generalized stacking fault energies. Using these potentials, the asymmetric C segregation was investigated in supercells containing faceted GBs at the experimentally relevant length scale and inclination angles.

The present chapter is organized as follows. In Section 5.2 we describe the methodology and the MEAM potential parametrization. Section 5.3 deals with the segregation energies of C solute at both S-{112} and A-{112} GBs. In Section 5.4.1 the atomistic mechanisms of the asymmetric line segregation are discussed. The summary is given in Section 5.5.

5.2 Methodology

The first principles calculations have been performed using the Vienna *ab-initio* simulation package, VASP [135]. A kinetic energy cutoff of 450 eV was used for the expansion of the plane wave basis set along with an equivalent $6 \times 6 \times 6$ Monkhorst-Pack k-point mesh for the bulk unit cell to sample the Brillouin zone. For the exchange-correlation the Local Density Approximation [96] was employed. All the atomic positions were relaxed until the absolute value of force on each atom was lower than 0.01 eV/Å.

The GSFE for the shuffle cut was calculated using the method described in the earlier chapter. The unit cell for the GSFE calculations consists of a 1×1 interface with 11 unit cells along the normal direction to the surface. A vacuum of 10 Å was used to decouple the two free surfaces. The substitutional and interstitial formation energies of C in bulk Si and the vacancy formation energy in bulk C were calculated using a $3 \times 3 \times 3$ supercell. For the calculations of GBs and point defects in GBs, a supercell with a 2×2 interface was implemented.

All interatomic potential calculations were performed using the Large-Scale Atomic/Molecular Massively Parallel Simulator (LAMMPS) [98]. The energy minimization has been performed using the conjugate gradient minimization method. The atomic positions were relaxed using conjugate gradient relaxation until the energy change was smaller than 10^6 eV/atom or all atomic forces were less than 10^{-6} eV/Å.

5.2.1 MEAM potential parametrization

To study C segregation in Si GBs, we have employed 2NN-MEAM potential calculations. The formalism of the 2NN-MEAM interatomic potentials has been discussed in detail in Chapter 3. For a binary system, such as the Si-C, three interatomic interactions, i.e., Si-Si, C-C, and Si-C, have to be considered. This implies that three interatomic potentials, i.e., for Si, C, and SiC, are required (see Section 3.2.2).

For the Si-Si interatomic interactions, the 2NN-MEAL potential developed and applied in Chapter 3 is used. This potential provides an excellent description of the elastic constants (C_{11}, C_{12}, C_{44}), the cohesive energy differences between the ground state fcc, and higher energy crystal structures, and the GSFE for shear along $\langle 110 \rangle$ and $\langle 112 \rangle$ in the basal plane. Furthermore, this potential describes in excellent agreement with DFT calculations the GB energies as a function of the inclination angle.

For the C-C interactions, the 2NN-MEAM potential by Daw and Baskes [136] has been applied with only one modification. As can be seen in Figs. 5.1 and 5.2, the 2NN-MEAM potential by Daw and Baskes (B-MEAM) [136] yields an artificial oscillatory behavior in GSFE profile for shear along $\langle 110 \rangle$ and $\langle 112 \rangle$ in the $\{111\}$ plane. Moreover, the bond order potential (E-bond) shows discontinuities in the GSFE profiles for both slip systems. To address this behavior, the screening parameter C_{min} has been adjusted. By lowering

Table 5.1: 2NN-MEAM potential parameter sets for Si and C. Parameters in bold are fitted in the present study. For Si the nearest neighbor distance, r_e is 2.35 Å, and the cohesive energy E_c is 4.63 eV. For C the nearest neighbor distance r_e was set to 1.54 Å, and cohesive energy E_c is 7.37 eV. The C potential is taken from Baskes *et al.* [42] and only the screening parameter C_{min} has been modified. The Si potential parameter set is taken from the previous Chapter.

	β_0	β_1	β_2	β_3	α	A	C_{min}	t_1	t_2	t_3	C_{max}	r_c	Δr	δ
Si	**4.5**	4.8	5.5	4.8	4.87	**0.80**	**1.60**	3.3	**3.60**	**-2.3**	2.8	4.0	0.1	0.0
C	4.10	4.20	5.0	3.0	4.38	1.0	**1.2**	5.0	8.04	-1.0	2.85	4.0	0.1	0.0

Table 5.2: 2NN-MEAM potential parameters set for C-Si interaction. All the parameters have been developed in the present thesis. the 3C-SiC has been used as the reference structure. The unit of the cohesive energy E_c is eV. The equilibrium nearest neighbors distance, r_e, cutoff distance, r_c, and smoothing distance, are in Å.

Parameter	Value	Parameter	Value
$E_c(Si, C)$	$(E_c(Si) + E_c(C))/2 + 0.4325$	$C_{min}(Si, Si, Si)$	**1.6**
$r_e(Si, C)$	**1.8878**	$C_{min}(Si, Si, C)$	**3.46**
$\alpha(Si, C)$	**4.37**	$C_{min}(Si, C, Si)$	**0.8**
$\rho_{Si} : \rho_C$	**1:1**	$C_{min}(Si, C, C)$	**1.2**
Δr	**0.1**	$C_{min}(C, C, Si)$	**1.2**
r_c	**4.8**	$C_{min}(C, C, C)$	**1.2**
$C_{max}(Si, C, Si)$	**1.85**	$C_{max}(Si, C, C)$	**2.85**
$C_{max}(C, C, Si)$	**2.85**	$C_{max}(Si, Si, C)$	**6.80**

the value of C_{min}, smooth GSFE curves are obtained for shearing along $\langle 110 \rangle$ and $\langle 112 \rangle$ directions in the {111} plane. However, this did not affect other physical properties such as the elastic constants, bulk modulus, phase transition energies, etc.

The parameters of the 2NN-MEAM potential for C are listed in Table 5.1. The calculated properties of C are given in Table 5.3 and compared with those calculated by DFT and E-bond order potential. The 2NN-MEAM potential provides, apart from the excellent qualitative, a very good quantitative description of the GSFE. As can be seen in Figs. 5.2(a), and (b), the present potential provides an excellent description of GSFE when compared with DFT calculations for shear along both $\langle 110 \rangle$ and $\langle 112 \rangle$ directions in the basal plane. Nevertheless, B-MEAM and E-bond order potentials fail to provide a quantitative description of the GSFE curves: The B-MEAM potential yields artificial oscillations in the GSFE curves and the E-bond order potential discontinuities. The unstable stacking fault energy of the $\{111\}\langle 110 \rangle$ and $\{111\}\langle 112 \rangle$ shear configuration is $\approx$518 meV/Å^2 and $\approx$ 520 meV/Å^2 calculated with the present MEAM potential. The unstable stacking fault energy for the same slip configuration calculated with DFT are $\approx$ 600 meV/Å^2 and $\approx$ 560 meV/Å^2, respectively.

The present potential can qualitatively describe the cohesive energy differences between the ground state diamond structure and higher energy phases with respect to DFT: Both DFT and P-MEAM potential predict the same ordering, i.e., diamond<β-tin<sc<bcc<fcc, where the left-sided structures are energetically more favorable than the right-sided. The charge neutral vacancy formation energy is in excellent agreement with DFT calculations (6.37 eV vs 6.88 eV, respectively). However, the E-bond order potential largely underestimates the vacancy formation energy (2.59 eV). The bulk modulus and the C_{11}, C_{12}, and C_{44} elastic constants are also in excellent agreement, within $\pm$8%, with the DFT calculated values. However, the present 2NN-MEAM potential overestimates the energies of the {100}, {110}, and {111} surfaces with respect to the DFT calculated values. Nevertheless, this discrepancy is not critical for the calculations presented here, which is the description of C

segregation at Si GBs and line junctions.

TABLE 5.3: Properties of C calculated using the present 2NN-MEAM potential (P-MEAM) and the E-Bond order potential compared to DFT data. ΔE denotes the cohesive energy differences between the diamond and the fcc, bcc, sc, and β-tin phases with respect to the diamond carbon structure in meV/atom. The lattice parameters, a, are in Å, the surface energies in meV/Å^2, the Bulk modulus and the elastic constants in GPa, the cohesive energy, E_c, in eV, and the vacancy formation energy, E_v in eV. U_{110} and U_{112} are the unstable stacking fault energies for shear along $\langle 110\rangle$ and $\langle 112\rangle$, respectively, in the $\{111\}$ plane. Values marked with an asterisk (*) are from DFT-LDA calculations performed in the present work.

		P-MEAM	E-Bond order [41]	DFT
diamond	E_c	7.37	7.37	8.95 [107]
	a	3.567	3.565	3.535 [107]
fcc	ΔE	1.157	4.483	4.50-4.65 [137], 4.61*
	a	2.936	2.739	3.02-3.07 [137], 3.005*
bcc	ΔE	1.115	3.963	4.24-4.35 [137], 4.36*
	a	2.294	2.16	3.32-2.37 [137], 2.34*
sc	ΔE	1.033	3.295	2.60-2.66 [137], 2.46*
	a	1.775	1.782	1.74-1.77 [137], 1.73*
β tin -diac	ΔE	0.968	3.728	2.72-2.82 [137]
	a	3.44	3.68	3.31 [137]
	c/a	0.54	0.435	0.39 [137]
Bulk modulus	B	440.58	442.87	460 [137], 461*
	B′	3.90	4.12	3.64-3.67 [137], 3.53*
Elastic constant	C_{11}	1062.92	1088.30	1094 [107]
	C_{12}	136.74	134.10	147 [107]
	C_{44}	629.42	641.27	584 [107]
E_v		6.37	2.59	6.88*
$E_{\{100\}}$		559.58	348.87	338.94 [107]
$E_{\{110\}}$		567.34	184.71	368.27 [107]
$E_{\{111\}}$		532.67	128.64	397.61 [107]
$U_{\{100\}}$		518	-	600
$U_{\{112\}}$		520	-	560

For the parametrization of the Si-C interactions, the 3C-SiC has been used as the reference structure. The 3C-SiC is the most stable and the only possible cubic structure among the large variety of SiC polytypes [138]. The cohesive energy $E_c(\mathrm{Si,C})$ was set equal to $(E_c(\mathrm{Si}) + E_c(\mathrm{C}))/2 + 0.4325$ where $E_c(\mathrm{Si})$ and $E_c(\mathrm{C})$ are the cohesive energies of Si and C, respectively (units are in eV). Using this value the formation enthalpy of 3C-SiC is in agreement with the DFT calculated value. The parameter $\alpha(\mathrm{Si}, \mathrm{C})$ is strongly correlated to the bulk modulus B of 3C-SiC [see Eq. (3.18)]. The nearest neighbor distance $r_e(\mathrm{Si}, \mathrm{C})$ was set to $\sqrt{3}a/4$ where a is the lattice parameter of 3C-SiC calculated from DFT. The density scaling parameter $(\rho_{\mathrm{Si}}/\rho_{\mathrm{C}})$ has not been changed and it is calculated by the densities of the individual elements.

To identify the correlation of the binary screening parameters with the material properties, a parametric study was conducted. Among all the screening parameters, $C_{\mathrm{min}}(\mathrm{Si}, \mathrm{C}, \mathrm{Si})$, $C_{\mathrm{min}}(\mathrm{Si}, \mathrm{C}, \mathrm{C})$, and $C_{\mathrm{min}}(\mathrm{Si}, \mathrm{Si}, \mathrm{C})$ were found to be strongly correlated with the GSFE and the GSFE profile. The parameter $C_{\mathrm{min}}(\mathrm{C}, \mathrm{C}, \mathrm{Si})$ was found to be strongly correlated with the interstitial and substitutional C formation energies in bulk Si. The parameters, $C_{\mathrm{min}}(\mathrm{Si}, \mathrm{Si}, \mathrm{Si})$ and $C_{\mathrm{min}}(\mathrm{C}, \mathrm{C}, \mathrm{C})$ were not adjusted and the corresponding values from the unary Si and C potentials are used, respectively. Parameter, r_c was set to 4.80 Å, and parameter, Δr was set to 0.1 Å. Parameters r_c and Δr are chosen such that the second nearest neighbor interactions are included. Larger values of r_c increase the computational cost without improving the potential's accuracy. Both parameters do not affect the properties of Si, C, and 3C-SiC included in the material's database. Once the correlation of the aforementioned screening parameters to the material properties was established they were employed to adjust the GSFEs energy along $\langle 110 \rangle$ and $\langle 112 \rangle$ in the $\{111\}$ plane and the C substitutional and interstitial formation energies in Si. The 2NN-MEAM parameters for the Si-C interactions are listed in Table 5.2.

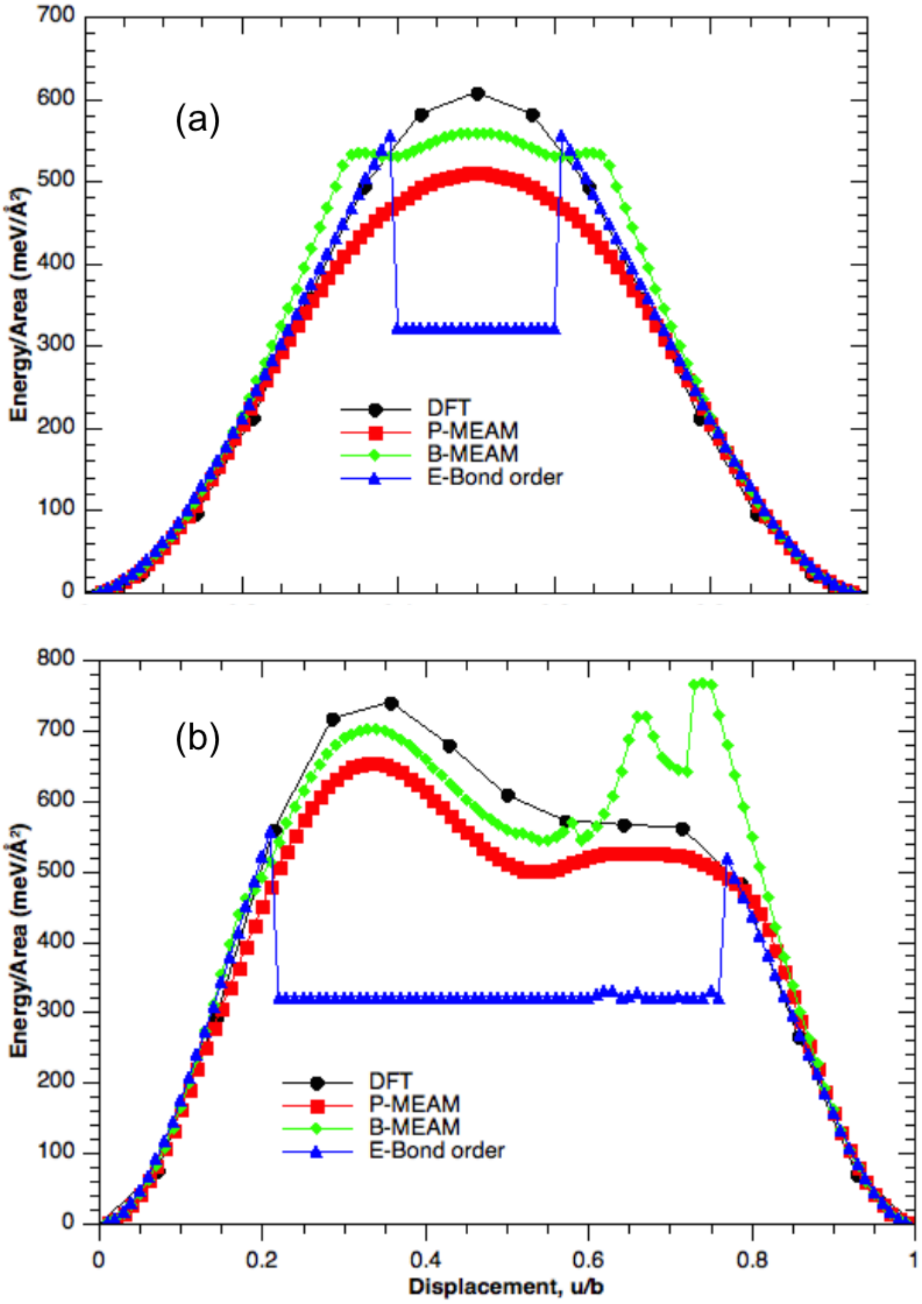

FIGURE 5.1: Generalized stacking fault energy as a function of the displacement along (a) $\langle 110 \rangle$ and (v) $\langle 112 \rangle$ in the $\{111\}$ glide plane of C obtained from DFT, P-MEAM, B-MEAM, and E-Bond order potentials.

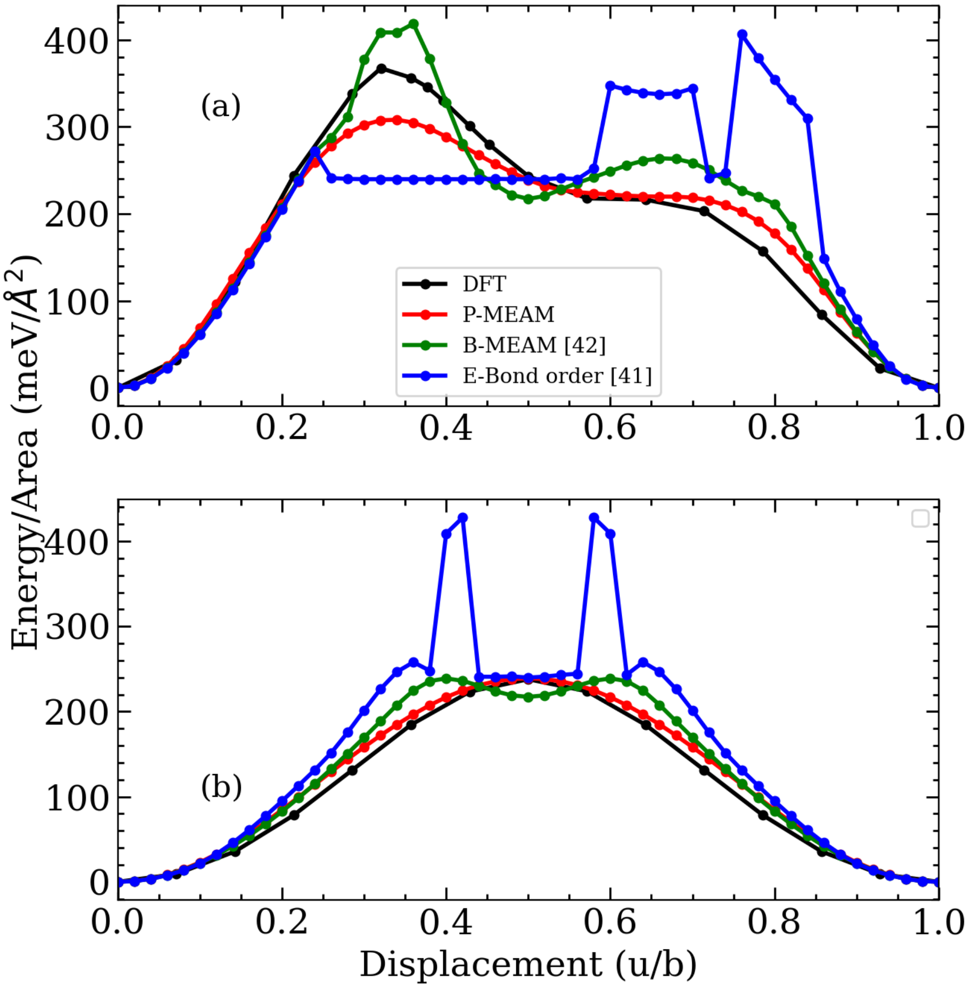

FIGURE 5.2: Generalized stacking fault energy of 3C-SiC for shear along (a) ⟨112⟩ and (b) ⟨110⟩ in the {111} plane obtained from DFT, P-MEAM, B-MEAM and E-Bond order potentials.

TABLE 5.4: Calculated bulk properties of 3C-SiC with the P-MEAM compared with the E-bond and B-MEAM potential calculations. The cohesive energy E_c and mixing enthalpy ΔH_f are in eV. The lattice constant, a, is in Å and the elastic constants are in GPa. Substitutional and interstitial formation energies are in eV. B-MEAM potential does not give a maximum at u/b=0.5 for shear along $\langle 110 \rangle$. Therefore, the U_{110} is not given. The E-bond order potential yields oscillatory behaviour for both shearing directions and the USFE values are also not reported.

		P-MEAM	E-Bond order [41]	B-MEAM [42]	DFT/Experiment
3C-SiC	ΔE	6.43	6.34	6.432	7.37 [107], 6.34
	ΔH_f	0.4325	0.341	0.43	
	a	4.359	4.359	4.359	4.338 [107]
Bulk modulus	B	211	224	211	225
	B_p	3.91	4.16	3.91	2.81
Elastic constant	C_{11}	409	383	402	405 [107]
	C_{12}	112	145	116	145 [107]
	C_{44}	226	239	215	247 [107]
C_{Si}		0.59	0.09	0.69	1.28, 1.95 [107]
C_i		2.85	5.42	1.43	3.38, 3.39 [107]
GSFE	U_{110}	200	-	-	199
	U_{112}	220	-	260	220

Table 5.4 lists the properties of 3C-SiC calculated with the present 2NN-MEAM potential alongside the DFT calculated values. As can be seen there is an excellent agreement between the 2NN-MEAM and DFT calculated elastic constants. The 2NN-MEAM calculated elastic constants are $C_{11} = 409$, $C_{12} = 112$, and $C_{44} = 226$ GPa whereas the DFT calculated values are $C_{11} = 405$, $C_{12} = 145$, and $C_{44} = 247$ GPa. Moreover, the present potential provides in a very good agreement with DFT the substitutional (0.59 vs 1.28-1.95 eV) and the interstitial (2.85 vs 3.38-3.39 eV) formation energies. For the interstitial configuration, the C atom is placed in the middle of the hexagon formed by the Si atoms along the $\langle 110 \rangle$ direction. Furthermore, the present 2NN-MEAM potential describes the GSFE profiles in excellent agreement with the DFT calculations. On the contrary, the B-MEAN and the E-bond potentials fail to qualitatively describe shear along $\langle 110 \rangle$ and $\langle 112 \rangle$ directions in the basal plane [see Figs. 5.2(a) and (b)]. Quantitatively, the unstable stacking fault energy for the $\langle 110 \rangle$ shear direction and stable stacking fault energy for the $\langle 112 \rangle$ shear direction are in excellent agreement with DFT.

5.3 Carbon segregation at flat GBs.

To further evaluate the transferability of the potential, the segregation energy of C substitution in symmetry inequivalent sites at the $\Sigma 3$ S-$\{112\}$ and A-$\{112\}$ GBs in Si have been calculated [see Figs. 5.3(a) and (b)]. The segregation energy is written as:

$$E_{\text{seg}} = E_{\text{GB}}^{\text{C}_{\text{Si}}} - E_{\text{bulk}}^{\text{C}_{\text{Si}}} \qquad , \tag{5.1}$$

where, $E_{\text{GB}}^{\text{C}_{\text{Si}}}$ and $E_{\text{bulk}}^{\text{C}_{\text{Si}}}$ are the total energies of the supercell with a GB and a C substituting for Si at the boundary and in the bulk like region of the supercell, respectively. To calculate the segregation energies supercells containing a pair of mutually compensated GBs have been employed. The number of unit cells were $8 \times 4 \times 2$ along $\langle 112 \rangle$, $\langle 110 \rangle$, and $\langle 111 \rangle$, respectively both for MEAM and DFT calculations.

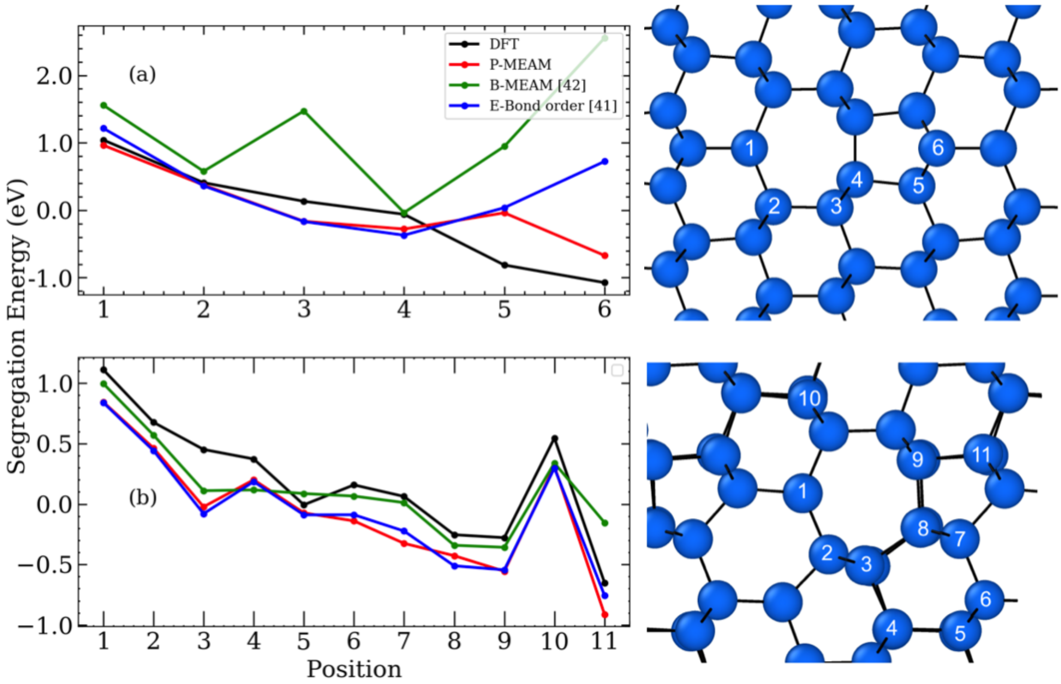

FIGURE 5.3: Segregation energies of C substitutional at (a) S-{112} and (b) A-{112} GBs. The horizontal axes represent the atomic positions denoted to the right side of each diagram.

At the S-{112} GB there are six symmetry inequivalent sites denoted as 1-6 in Fig. 5.3(a). Positions 1-4 correspond to atoms in the 7-atoms ring and positions 4-6 in the 5-atoms ring. At site 6 the atom is five-fold coordinated. Furthermore, the interatomic distance between a Si atom at this position and its 5 nearest neighbors is $0.46a$ and $1.4a$ Å where a is the lattice parameter of Si.

Fig. 5.3(a) shows the calculated segregation energies as obtained from present 2NN-MEAM potential, DFT, B-MEAM, and E-bond potential calculations. The DFT calculated segregation energies vary from $\approx$-1 to $\approx$1 eV. The five fold coordinate site is the energetically most favorable position for C substitution at the S-{112} GB. Moreover, the sites at the 5-atoms ring have negative segregation energies, i.e., it is more favorable for C atoms to substitute Si at these sites than in bulk. The B-MEAM potential fails to both qualitatively and quantitatively describe the segregation of C at the S-{112} GB. Indeed, B-MEAM potential predicts positive segregation energies for all sites and the five fold coordinated site has the highest segregation energy. The

E-bond potential shows a better description of segregation, i.e., smaller differences with the DFT calculated energies. However, it fails to qualitatively describe the segregation energetics. It erroneously calculates positive segregation energy at the five fold coordinated atom. The present 2NN-MEAM potential provides a very good qualitative and quantitative description of the segregation energies. The P-MEAM predicts site 6 as the energetically most favorable site for segregation. The only discrepancy with respect to the DFT calculations is the overestimation of the energy of segregation and site 5. The failure of B-MEAM and E-bond potentials to predict the most favorable site for C segregation and hence provide at least a qualitative description of C segregation at these GBs can be attributed to the absence of screening of the interatomic interactions. As has already been mentioned the site at the apex of the 5-atoms ring is over-coordinated. Hence, screening interactions is important to achieve a consistent description of the energetics.

Eleven symmetry inequivalent positions at the A-{112} GB have been considered to calculate the segregation energies [see Fig. 5.3(b)]. Likewise segregation at the S-{112} GB, the DFT calculated segregation energies vary from ≈-1 to ≈1 eV. The energetically most favorable site for segregation is at the 5-atoms ring [site 11 in Fig. 5.3(b)]. Both the present 2NN-MEAM potential and the E-bond potential provide a good qualitative description of the segregation energies, though they underestimate the energies. Furthermore, they predict site 11 at the 5-atoms ring to be the energetically most favorable, in agreement with DFT calculations. On the other hand, the B-MEAM potential erroneously predicts the site at the apex of the 5-atoms ring [site 9 at Fig. 5.3(b)] as the most favorable site for C segregation.

In the A-{112} GB all atoms are four fold coordinated. Therefore and unlike segregation at the S-{112} GB, atoms' coordination plays no role in the calculated segregation energies. Nevertheless, the energetically most favorable C segregation sites are in the 5-atoms ring. These sites are compressively strained [see Fig. 5.8(a)]. Both Si and C are homovalent atoms. Therefore, the segregation energies are predominantly controlled by strain. C atoms are smaller than Si atoms. Hence, the compressively strained sites at the 5-atoms ring are preferable.

In order to further highlight the effect of strain on the C segregation energies, in Fig. 5.4 the energy of C substitutional in Si bulk is plotted against the applied hydrostatic strain. The substitutional energy in strain free bulk Si is used as a reference, i.e.:

$$\Delta E = \left[E^{\mathrm{C_{Si}}}(\varepsilon) - E^{\mathrm{Si}}(\varepsilon)\right] - \left[E^{\mathrm{C_{Si}}}(0) - E^{\mathrm{Si}}(0)\right] \quad , \tag{5.2}$$

where, $E^{\mathrm{C_{Si}}}(\varepsilon)$ and $E^{\mathrm{C_{Si}}}(0)$ are the total energies of the system with a C substitutional at hydrostatic strain ε and at strain free Si bulk, respectively. $E^{\mathrm{Si}}(\varepsilon)$ and $E^{\mathrm{Si}}(0)$ are the total energies of bulk Si at hydrostatic strain ε and at zero strain, respectively. To calculate the aforementioned energy difference $8 \times 4 \times 2$ supercells of bulk Si have been employed oriented along $\langle 112 \rangle$, $\langle 110 \rangle$ and $\langle 111 \rangle$ respectively. As can be seen in Fig. 5.4, compressive hydrostatic strain in the order of 1% reduces the chemical potential of substitutional C by more than 0.5 eV. On the other hand, 1% tensile strain increases the chemical potential of C by ≈0.5 eV. Compared to DFT, the present 2NN-MEAM and the B-MEAM potentials over- and under-estimate these energy differences and the E-bond potential provides a better quantitative agreement. This is because the MEAM potentials underestimate the bulk modulus of SiC by ≈6%, while the E-bond potential by less than ≈0.5% with respect to DFT (see Table 5.2). Nevertheless, compressive and tensile hydrostatic strain reduces and increases the chemical potential of C substitutional, respectively.

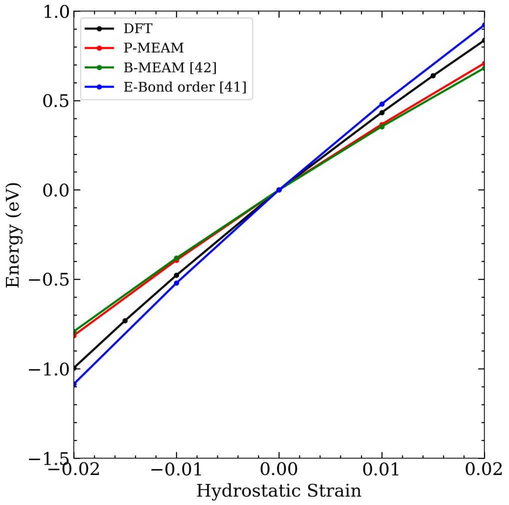

FIGURE 5.4: Strain energy plotted against the hydrostatic strain of bulk Si with a C substitutional. The strain energy of pristine Si is used as a reference [see Eq. (5.2)].

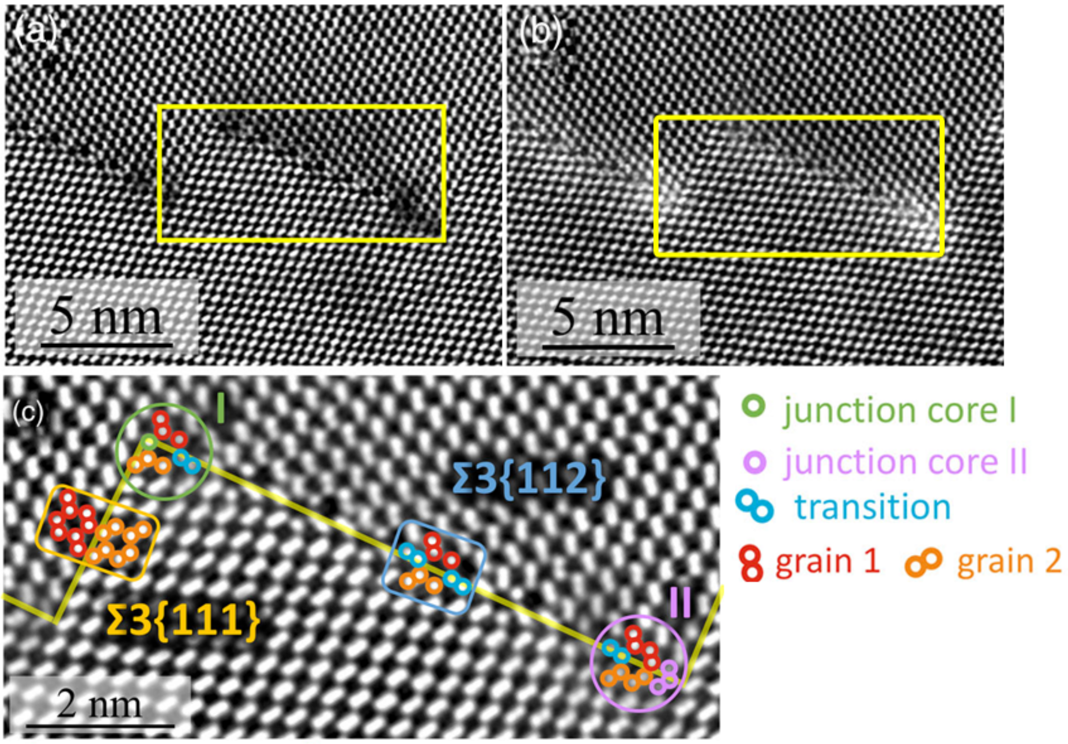

FIGURE 5.5: Atomic structures of a faceted Σ3 tilt GB in Si derived by high resolution scanning tunneling transmission electron microscope (HR- STEM). (a) STEM image of a faceted GB (b) strain sensitivities of the above faceted GB. The brighter spot sows the higher amount of strain. (c) Core of the faceted junction as denoted by I and II. The facets are Σ3 {111} and Σ3 {112}. The Figure has been adapted from Ref. [16].

5.4 Asymmetric C segregation at GB line junctions

The aforementioned strong dependence of segregation energies on strain is expected to influence the impurities' segregation at the GBs. More specifically, it is very reasonable to assume that the segregation of homovalent impurities, such as C, at flat S- and A-{112} GBs will follow the periodic alternation of compressive and tensile regions at these planes [see Figs. 5.8 (a) and 5.9]. Nevertheless, regions of particular interest with respect to segregation, are the line junctions of A-{112} with the twin boundaries. The superposition of the strain field arising from the partial dislocations at these junctions (see Fig. 5.9) with the periodic strain field of the flat A-{112} GB, may locally enhance or reduce the segregation potential at and around these line defects.

5.4.1 Experimental evidence

Let us briefly discuss the scanning transmission electron microscopy (HAADF-STEM) and atom probe tomography (ATP) experiments that provide evidence of asymmetric impurities' segregation at the line junctions of Σ3 A-{112} and {111} GBs. Since these experiments are not explicitly part of the present thesis, only the key messages will be presented. More details on the experiments can be found in Ref. [16].

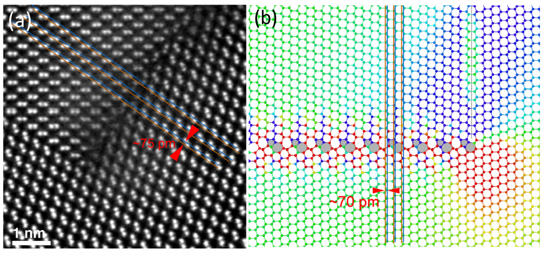

FIGURE 5.6: {111} lattice plane offset at an A-{112} GB determined by (a) HAADF-STEM and (b) MEAM potential calculations. The color code in (b) denotes the volumetric strain [see also Fig. 5.8(a)].

Fig. 5.5(a) shows the high angle annular dark-field STEM (HAADF-STEM) image of a faceted Σ3 GB. This interface consists of shorter {111} and longer {112} facets. The low angle annular dark-field (LAADF) STEM image shown in Fig. 5.5(b) reveals the strain state at the interface. In agreement with the atomistic calculations on the A-{112} GB [see Fig. 5.8(a)] and in contrast to the calculations on the S-{112}, the strain is not symmetric at the two line junctions. This constitutes a strong indication that the {112} facet consists of the asymmetric reconstruction. Indeed, as is revealed by the slight rotation of the blue colored Si dumbbells in Fig. 5.5(c) the {112} facet is asymmetric. Moreover, the experimentally determined {111} lattice plane offset at the {112} segment (≈75 pm) fits excellently with the MEAM potential calculated offset at an A-{112} facet (≈70 pm), see Fig. 5.6.

The line junction denoted as (I) in Fig. 5.5(c) almost conserves the structural units present at the {112} facets (only one of the blue colored Si dumbbells is replaced by a single atomic column which is denoted with the green circle). On the other hand, the atomic motif at the junction (II) is substantially different and the atomic columns are densely packed. The APT experiments revealed a linear segregation pattern for C, Fe, and N impurities. The distance between adjacent impurity density peaks was calculated to be equal to

8 ± 2 nm which is in excellent agreement with the faceting period calculated in the STEM images (see Fig. 5.5). Moreover, the APT revealed that these segregation lines coincide with line junctions (II).

5.4.2 Atomistic calculations

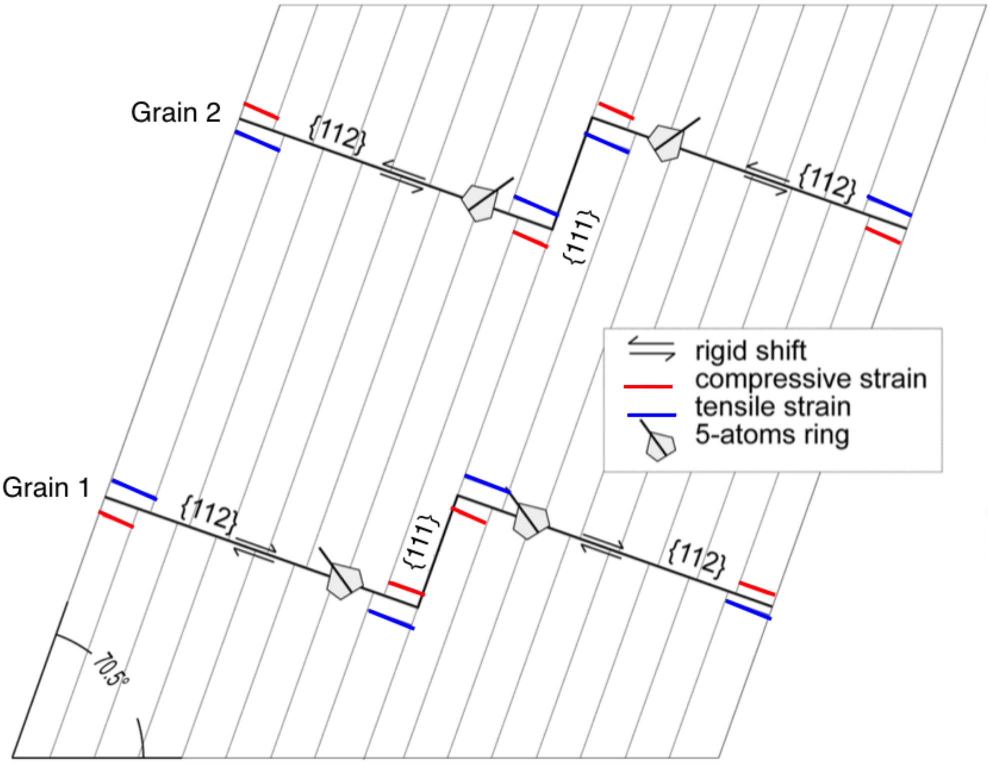

FIGURE 5.7: Schematic representations of the supercell employed to compute the C segregation energies. The supercell consists of asymmetric {112} and {111} facets. The thickness of the supercell along ⟨110⟩ is 0.77 nm.

To identify the atomistic mechanisms underlying the above mentioned asymmetric line segregation, large scale atomistic simulations of C substitution at faceted Σ3 GBs in Si have been employed. The simulation cells consisting of a pair of mutually compensated faceted GBs have been constructed. The length of the {111} facet in the (110) plane was ≈6.6 nm and of the A-{112} facet ≈18.8 nm. The corresponding unfaceted/flat GB would be inclined by ≈ 70.5° with respect to the {111}. The separation distance between the two GBs was ≈16 nm. Convergence checks showed that this distance is sufficient to decouple the GBs. Larger separation distances did not affect the C segregation energies at the GBs. The thickness of the cell along $\langle 110 \rangle$ was four atomic layers (≈0.77 nm). A schematic representation of the supercell indicating the 5-atoms rings and {111} planes is shown in Fig. 5.7. The simulation cell consists of 64960 atoms.

Before investigating C segregation, the equilibrium structure of the faceted GB has been calculated. This was accomplished in a two step procedure. In the first step, the structure was annealed: The temperature was raised to 600 K and reduced to 0 K with a cooling rate of 7.5 K/psec. Convergence checks indicated that an order of magnitude slower cooling rate does not affect both the atomic positions and the total energy. The annealing procedure was applied to avoid trapping in metastable states. In the second step, the atomic positions were relaxed with a conjugate gradient relaxation scheme, until the maximum force acting on the atoms was less than 10^{-6} eV/Å.

As can be seen in Fig. 5.7 the two GBs denoted as Grain 1 and Grain 2 are symmetry inequivalent. This is because the {112} facets are asymmetric. Hence, the strain field at the corresponding two facet junctions has an opposite sign. Nevertheless, only results for the faceted GB that fits the experimentally observed structure, i.e., structural units and core structure of the facet junctions, are discussed. However, the calculated strong anisotropy of C impurities segregation to only one particular facet junction is observed for both faceted GBs.

Using the relaxed structure of the above mentioned faceted GB, the volumetric strain has been calculated [see Fig. 5.8(a)]. The volumetric strain at each atomic site was calculated using the volume of the tetrahedra formed by the four nearest neighbors. In Fig. 5.8(a) the strain is plotted at and around the Grain 2 shown in Fig. 5.7. The tensile strained regions are colored in hot/red colors and the compressive regions are in cold/blue colors. The volumetric strain distribution resamples that of the ε_{xx} component shown in 5.8(a) and arises from the presence of two partial dislocations of opposite

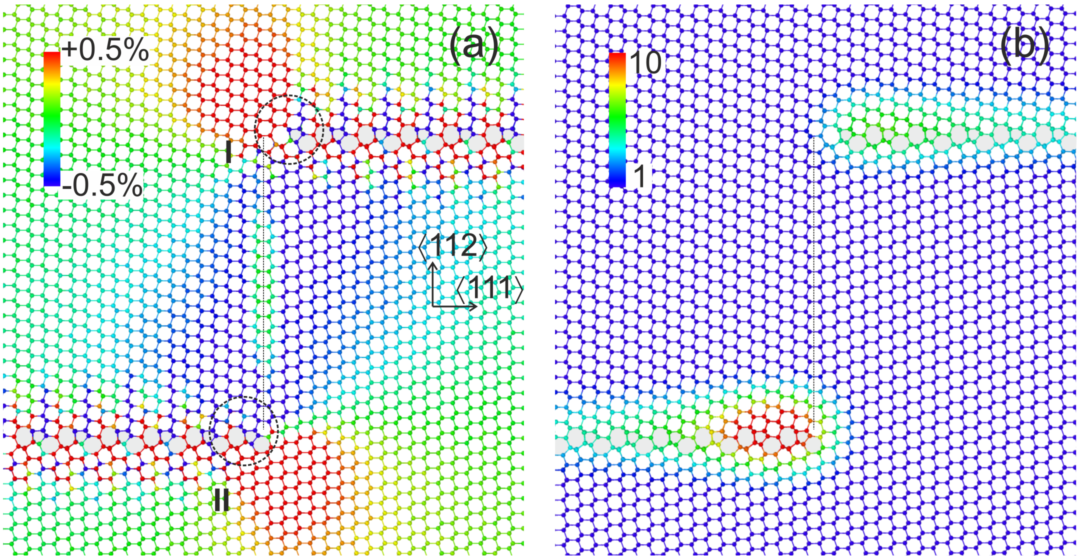

FIGURE 5.8: (a) Volumetric strain at a faceted Σ3 Gb consisting of {111} and A-{112} facets. Cold and hot colors represent compressive and tensile strain, respectively. (b) C concentration at the faceted GB with respect to the C concentration in bulk at T=300/;K [see Eq. (5.3)].

Burgers' vectors at the two line junctions. The origin of these dislocations is the rigid shift of one grain with respect to the other and hence the misfit of the {111} planes in the A-{112} segment. At the {111} twin boundary this misfit is accommodated by the tensile, and compressive regions around the line junctions (see Fig. 5.7).

The strain distribution arising from the partial edge type dislocation at the line junctions cannot explain the experimentally revealed asymmetric C segregation. Tensile and compressive regions are present at both line junctions. In Section 5.3 it has been shown that the energetically most favorable site for C segregation at the A-{112} GB is at the 5-atoms ring. However, the 5-atoms rings are not symmetric with respect to the {112} planes. Furthermore, as is schematically indicated in Fig. 5.7, these rings are oriented into compressive and tensile regions at the facet junction cores. This is expected to reduce and increase the C chemical potential in these regions and hence enhance and reduce the C content, respectively.

To quantify the effect of strain on C segregation at the line junctions, the C segregation energies at these defects have been explicitly calculated by using Eq. (5.1). Using these energies, the excess local C content has been calculated

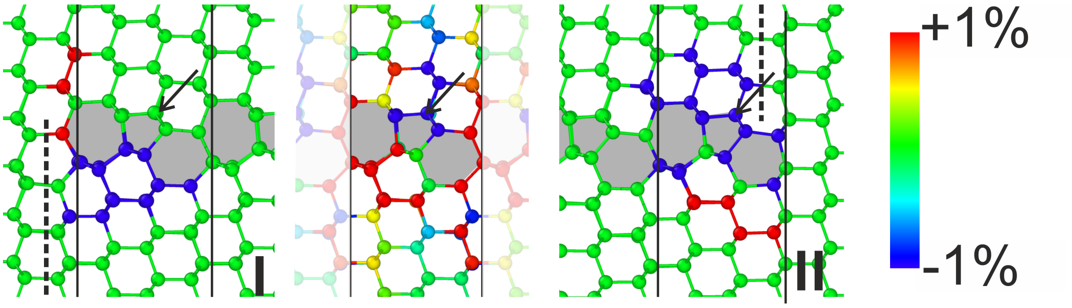

FIGURE 5.9: MEAM potential calculated atomic geometries and volumetric strain at junction I (left), junction II (right), and flat A-{112} GB. The dashed lines indicate the twin and the gray shaded regions the structural units of the A-{112} GB. Blue/cold colors represent compressive strain and red/hot colors tensile strain. The arrows denote the energetically most favorable site for C substitutionals at the flat A-{112} GB.

using Boltzmann statistics. The relative C concentration at each site with respect to the bulk content was calculated as:

$$\frac{c_i}{c_0} = \exp\left(-\frac{E_{\text{seg}}}{k_B T}\right) \quad , \tag{5.3}$$

where c_i and c_0 are the C contents at site i and in bulk, respectively, E_{seg} is the segregation energy, k_B is the Boltzmann constant and T is the temperature. For the calculations to be consistent with the ATP measurements (see Section 5.4.1), the local concentrations were integrated within a cylindrical region with 0.5 nm full width at half maximum (FWHM). The calculated local C contents are color coded in Fig. 5.8(b). The highest C concentration was found in the vicinity of line junction II and it is ≈1 order of magnitude higher with respect to the bulk. High C concentration was found at junction I as well. However, the C content is approximately ×5 lower than that at junction II.

These findings are in excellent agreement with the experimental observation of site-specific line segregation. To identify the underlying mechanism let us focus on the regions of the two line junctions (see Fig. 5.9). As has already been mentioned, the energetically most favorable site for C substitution at flat A-{112} GB is at the 5-atoms ring, indicated by the arrow in the middle of Fig. 5.9. The driving force for the reduction of the C chemical potential at this site is the compressive strain state of this site. At the junction I, the 5-atoms ring is in the tensile region of the strain field induced by the partial dislocation. Hence, the aforementioned compressive strain largely cancels out by the dislocation's tensile strain. On the other hand, at junction II, the 5-atoms ring is oriented toward the compressive region of the dislocation. This enhances the compressive strain of atom at the 5-atoms ring and results in further reduction of the substitutional C chemical potential. This explains the enhanced C content calculated and observed at line junction II.

5.5 Conclusions

In this chapter, the development of 2NN-MEAM potentials for C and SiC has been presented. These potentials have been fitted on and benchmarked against various physical properties such as GSFE, elastic constants, cohesive energy differences of several stable and metastable crystal phases, charge neutral vacancy formation energies, interstitial and substitutional energies, and surface energies. The 2NN-MEAM potential for C gives an excellent qualitative description and in general a very good quantitative description of these properties. Although it provides a rather poor description of the energies of low index diamond surfaces, this is not crucial to investigating the segregation of C substitutionals in Si GBs. As a reference structure for the 2NN-MEAM potential for SiC, the 3C-SiC structure has been used. This potential provides an excellent description of the GSFE for shear along $\langle 112 \rangle$ and $\langle 110 \rangle$ in the $\{111\}$ plane as well as of the elastic constants. Moreover, it provides a very good description of the C substitutional and interstitial formation energies in bulk Si. Furthermore, the segregation energies of C impurities at both S-$\{112\}$ and A-$\{112\}$ Si GBs have been evaluated for several symmetry non-equivalent positions. The segregation energies are in excellent qualitative and very good quantitative agreement with the DFT calculated values.

Following the rigorous benchmark of the interatomic potentials, we have performed simulations on faceted Σ3 GBs to identify the origin of the experimentally observed asymmetric line segregation at the facet junctions. The simulations have been performed using supercells that contained {111} and A- and S-{112} facets at the experimental length scale. Based on these calculations, the volumetric strain at and around the line junctions of these facets has been evaluated. This revealed that the facet junctions are accompanied by regions of tensile and compressive strain. The origin of the strain field is the presence of partial edge type dislocations of opposite Burgers vectors at the two line junctions which are introduced to accommodate the misfit of the {111} planes across the A-{112} boundaries. The C substitutional segregation energies and concentration at the line junctions have been also calculated. These calculations revealed that the lack of mirror symmetry across the A-{112} and the differences in the strain and the core structure of the two line junctions lead to strong asymmetric segregation of C impurities in one of the two junctions.

Chapter 6

2NN-MEAM Potentials for Atomistic Fracture calculations in NiRe Alloys

6.1 Introduction

The durability and reliability of structural materials are of great importance. Applications of these materials such as high-speed train railways [139, 140] or airplane wings [141] clearly demonstrate the importance of understanding and controlling materials' failure. Furthermore, low-cost yet robust against failure devices/structures allow for more efficient energy usage. The study and understanding of the mechanisms governing fracture are essential in designing structural materials: It allows to predict materials' failure and design structural materials with improved mechanical properties [140].

The fracture process itself is multi-scale in nature. Nevertheless, fracture at the atomistic and micro-scales initiates by bond breaking across a crack or by the emission of dislocations at a crack tip [141–143]. A crack can be considered as a material separation by opening or sliding where the separation distance is much smaller than the separation extend [144]. The crack front is formed by two faces which are usually considered to lie on the same surface before deformation. When the cracked body is subjected to an external load, these crack faces move relative to each other. Depending on the external load and the displacement of the cracked surfaces, three fracture modes

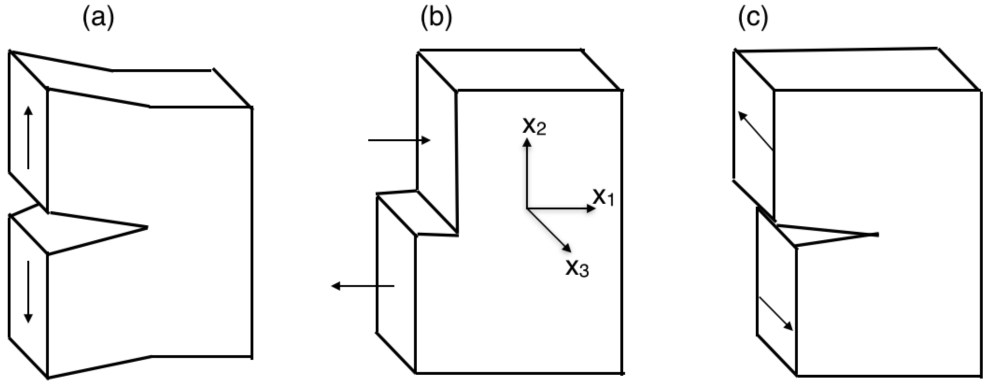

FIGURE 6.1: Schematic representation of crack opening modes: (a) Mode I or opening mode, (b) Mode II or sliding mode, and (c) Mode III or tearing mode. The arrows indicate the applied stress/load.

can be distinguished (see also Fig. 6.1) [140]:

Mode I: It is an opening mode where the application of tensile external load results in symmetric and normal to the crack surface displacements of the bounding facets [see Fig. 6.1(a)].

Mode II: It is the sliding mode that results from the application of shear stress parallel to the crack plane and normal to the crack front. The displacement of the bounding facets is in the crack surface [see Fig. 6.1(b)].

Mode II: The shear stress is acting parallel to the crack plane and the crack front. The displacements of the bounding facets are parallel to both the crack plane and the crack front, as well. This results in the tearing mode [see Fig. 6.1(c)].

Apart from these three modes, the fracture can occur in combinations of any of these modes. Atomistic calculations have been widely applied to study the above mentioned fracture modes [145–147] and are now well established to provide insights into the atomistic mechanisms governing failure mechanisms in metals, semiconductors, and metallic alloys [38, 45, 46, 148, 149].

In the present study, the effect of Re in the fracture mechanism at a crack tip in Ni is investigated. The choice of this material's system is motivated by the fact that Ni-based superalloys are characterized by high ductility, creep and fatigue resistance, and high melting point. Because of their superior ductility and high melting point they are used in jet engine turbine blades [150, 151]. The addition of a few at.% Re in Ni is known to considerably improve the creep resistance of Ni-based superalloys. However, the mechanism of the so-called *rhenium effect* is still under debate. A possible mechanism that has been investigated by combining cluster expansion based Monte-Carlo simulations with experiment is the formation of D_{1a} crystal structure which retards the dislocation climb [152]. The D_{1a} phase may also hinder the coarsening of the $\gamma^{'}$ phase of Ni-based superalloys.

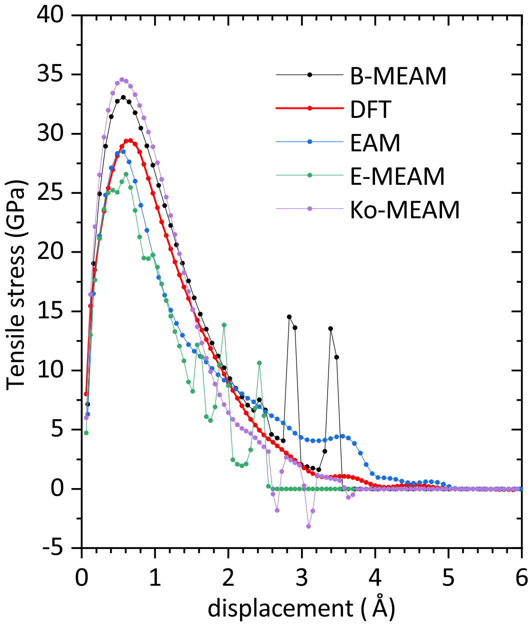

FIGURE 6.2: Comparison of tensile stress of Ni {112} as a function of separation displacement calculated with different interatomic potentials and DFT. Ko-MEAM, EAM, B-MEAM, and E-MEAM refer to the potentials [153], [154], [155] and [156] respectively.

Crack tip phenomena during fracture are controlled by mechanisms that span multiple length scales such as bond breaking and lattice trapping [148, 157], dislocation emission [158, 159], cleavage anisotropy [160, 161], long range elastic strain interactions, and kink nucleation [162–164]. To accurately describe all these mechanisms in atomistic simulations, one needs to employ simulation cells consisting of at least 10^5 atoms [165]. *Ab-initio* calculations can accurately describe the mechanical properties of materials at all relevant scales. However, these calculations are limited by the available computational power to systems consisting of a few thousand atoms. Nevertheless, semi-empirical interatomic potentials are routinely used nowadays to calculate cells consisting of a few million atoms and hence they provide an alternative route to model fracture. For example, such interatomic potentials have been widely used to study dislocation and fracture related properties both in unary and binary systems [38, 39, 166]. However, a prerequisite to accurately describing such complex phenomena using interatomic potentials is the transferability of these potentials, i.e., their robustness in different conditions and environments.

For Ni, there is a large number of semi-empirical interatomic potentials in literature [153–156]. For example, Lee *et al.* [155] developed 2NN-MEAM interatomic potentials for Ni to reproduce the physical properties of Ni. The MEAM potential developed by Ko *et al.* [153] was used to describe the martensitic phase transition in Ni-Ti. Interatomic potentials have been developed in both the EAM and MEAM frameworks for Re [167, 168]. The Re EAM potentials developed by Bonny *et al.* [167] were trained to predict the properties of W-Re solid solution whereas MEAM Re potentials [168] were trained to reproduce the physical properties only.

We tested a large number of Ni and Re interatomic potentials to validate their ability to model fracture. Specifically, these potentials were tested against the physical properties which are known to correlate with fracture. These include surface energies, stacking fault energies, elastic constants, as well as work of separation and traction separation behavior. As shown in Fig. 6.2, all potentials that were evaluated show either discontinuous traction separation or unrealistically negative traction separation. These artifacts are known to qualitatively affect crack tip behavior, e.g., unrealistic crack tip blunting in atomistic simulations [38, 169].

To study the mechanisms occurring at the crack tip of Ni during fracture, 2NN-MEAM potentials for Ni, Re, and Ni-Re system have been developed. A database that includes the properties that are known to correlate with fracture properties has been constructed to fit, validate, and evaluate the transferability of the potentials.

The Chapter is organized as follows. Section 6.2 describes the linear elastic fracture mechanics theory, Section 6.3 provides the methodology, Sections 6.3.1 to 6.3.8 deal with tensile stress, GSFE, and melting temperature calculations. Finally, the results are discussed in Section 6.4 and the conclusions are outlined in Section 6.5.

6.2 Linear Elastic Fracture Mechanics

6.2.1 Solution of stresses

Key parameters in the description of fracture are the stress intensity factor, K, and the critical stress intensity factor, K_c. The stress intensity factor describes the stress near the crack tip caused by an external load and the critical intensity factor is the minimum stress intensity required to propagate the crack. The units of both K and K_c are stress times the square root of length, e.g., $\mathrm{Pa}\sqrt{\mathrm{m}}$ in S.I. . The critical intensity factor can be derived from an energy balance consideration at the crack tip under an external load.

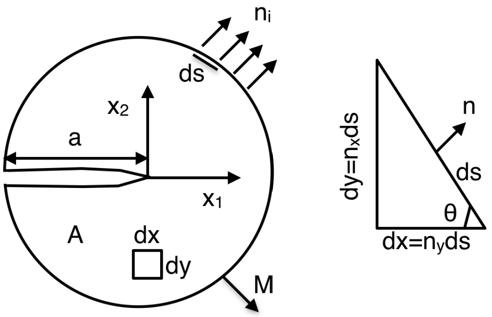

FIGURE 6.3: Schematic representation of a cracked body. x_1 is the crack propagation direction and the crack plane normal is along x_2. a is the crack length, n_i is the vector normal to the surface element ds. dx and dy are the length and width of an element of the cracked body subjected to a body force, M.

The energy balance consideration at a crack tip can be formulated as follows: During the propagation of a crack, extra free surfaces are formed which costs energy. Furthermore, other phenomena such as plastic deformation via dislocation nucleation and emission or formation of point defects or defect clustering may take place which also involve energy dissipation. For the crack to grow, the rate of the energy dissipation (G) should be balanced by the rate of the mechanical work done by the external load:

$$G = -\frac{dE}{da} \qquad , \tag{6.1}$$

where E is the potential energy and da is the crack advanced distance. The potential energy is defined as follows

$$E = \frac{1}{2}\int_v \sigma_{ij}\epsilon_{ij} dV - \int_s T_i n_i ds \qquad . \tag{6.2}$$

Here, σ_{ij} is the stress tensor, ϵ_{ij} is the strain tensor, and dV is the volume. Therefore, the first term on the right hand side of Eq. (6.2) defines the strain energy stored in the volume dV. The second term is the energy due to the applied traction, T_i, on the surface of area ds. n_i is the normal vector to the surface (see Fig. 6.3). Rice [143] and Irwin [170] showed that the energy release rate G can be correlated to the stress intensity factor. The energy release rate for mode I fracture in plane strain condition is written as

$$G = \frac{1-\nu^2}{Y} K_I^2 \qquad , \tag{6.3}$$

where ν is the Poisson ratio, Y is the Young's modulus, and K_I is the critical stress intensity factor. Accordingly, the energy release rate, G is related to the fracture toughness of mode I fracture as

$$K_{Ic} = \sqrt{\frac{Y}{1-\nu^2} G} \tag{6.4}$$

In mode I brittle fracture G is equal to the energy required to create two new surfaces, i.e., $G = 2\gamma_s$, where γ_s is the surface energy. In this case, the critical stress intensity factor can be written as (Griffith critical stress intensity factor, K_{Griffith}):

$$K_{\text{Griffith}} = \sqrt{\frac{2Y\gamma_s}{1-\nu^2}} \tag{6.5}$$

For mode I ductile fracture, the nucleation of dislocation has to be considered. If we consider a solid subjected to loading conditions to create the stress intensity factor of mode I (K_{Rice}, Rice critical stress intensity factor) then the nucleation condition for a dislocation is written as [142]

$$\left[f_I(\theta)K_{\text{Rice}}\right]\cos\phi = \sqrt{\frac{2\mu}{1-\nu}\left[\cos^2\phi + (1-\nu)\sin^2\phi\right]\gamma_{us}} \qquad . \tag{6.6}$$

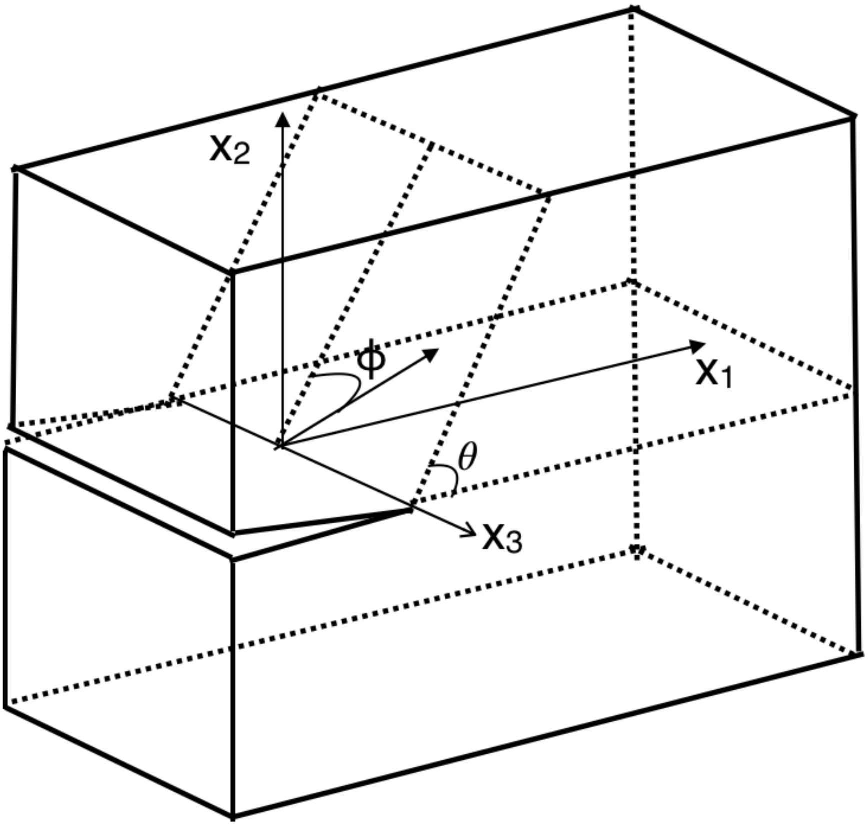

FIGURE 6.4: Schematic representation of the geometry to calculate K_{Rice}. θ is the angle between the dislocation Burgers vector and the crack direction and ϕ is the angle between the crack front normal and the slip plane.

Here, $f_I(\theta)$ is a geometric factor. θ and ϕ are the angles between dislocation Burger's vector and crack direction and between the crack and the slip planes, respectively (see Fig. 6.4). μ is the shear modulus and γ_{us} is the unstable stacking fault energy. For an isotropic material, the geometric factor is written as

$$f_I(\theta) = \cos^2\left(\frac{\theta}{2}\right)\sin\left(\frac{\theta}{2}\right) \quad . \tag{6.7}$$

The Griffith and Rice criteria relate the critical intensity factor with the surface and the unstable stacking fault energies, respectively. In addition to these two theories, the cohesive zone modeling establishes the relation between the critical stress intensity factor with the work of separation. The separation energy of two surfaces along the normal direction increases with the separation distance and vanishes at a sufficiently long distance. Rose *et al.* [171, 172] showed that the interaction between the two surfaces has an exponential form and Needleman *et al.* [173] showed that the traction, σ can be written as a function of the separation distance, δ as following

$$\sigma\left(\delta\right) = -\sigma_0 \frac{\delta}{\delta_0} exp\left(-\frac{\delta-\delta_0}{\delta_0}\right) \quad . \tag{6.8}$$

Here, σ_0 is the cohesive strength of the material, and δ_0 is the crack opening displacement (see Fig. 6.5). The significance of this relation is that the area under the σ vs δ curve is the work of separation w. The work of separation can be calculated by atomistic calculations and for a homogenous isotropic solid is written as:

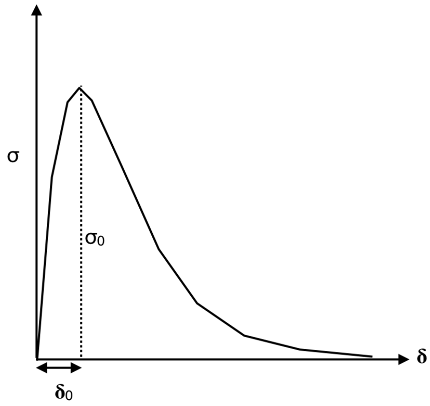

FIGURE 6.5: Schematic diagram of tensile stress against separation distance. The maximum stress (σ_0) is the cohesive strength, and the separation distance (δ_0) at which this stress occurs is the critical crack tip opening displacement.

$$K = \sqrt{\frac{Yw}{1-\nu^2}} \quad . \tag{6.9}$$

Here, Y is the Young's modulus. w can be calculated by integrating the tensile stress vs separation distance curve [38, 174]. The calculation of the traction stress σ and hence the work of separation w are discussed in Subsection 6.3.6.

6.3 Methodology

6.3.1 *Ab-initio* calculations

As described in the above section, the accurate description of the fracture properties requires the accurate description of the surface energies, the unstable stacking fault energies, and the tensile stress. Therefore, to build the database to parametrize the interatomic potential, we have calculated the surface energies, the generalized stacking fault energies, and tensile stress by employing DFT calculations. Apart from these, we have calculated the energy differences of the bcc, sc, diamond, and hcp phases with respect to the ground state fcc for the unary Ni system. Similar properties were also calculated for hcp Re. To build the database for the binary system, we have considered the CsCl-NiRe structure as the reference structure. Therefore, we have included cohesive energies, elastic constants, and formation enthalpies of this phase in the database. Furthermore, the Re substitutional and interstitial formation energies in fcc Ni were also considered. In addition to these, we have evaluated the formation energies and elastic constants of binary Ni-Re in the D1a, $D0_{22}$, Cu_3Au, and NaCl phases. These calculations were then used to benchmark the transferability of the interatomic potentials.

The spin-polarized DFT calculations were performed using the Vienna *Ab-initio* simulation package [135]. A kinetic energy cut-off of 400 eV was used for the expansion of the plane wave basis set with an equivalent $6 \times 6 \times 6$ Monkhorst-Pack k-point mesh for the bulk unit cell to sample the Brillouin zone. For the exchange and correlation, the Generalized Gradient approximation was used. All the atomic positions were relaxed until the force on each atom is lower than 0.01 eV/Å. For the surface and GSFE calculations, 10 unit cells were considered along the normal direction to the surface and interface. The visualization of the large scale atomistic simulation has been performed using Ovito [175].

6.3.2 2NN-MEAM Interatomic Potentials

The formalism and the methodology to parametrize 2NN-MEAM potentials have been described in detail in Sections 3.2 and 3.3, respectively. In the following, the parametrization of the 2NN-MEAM potentials for the Ni-Re binary system is briefly described. For the unary Ni, and Re the cohesive energies, E_c and equilibrium nearest neighbor distances, r_e are obtained from existing interatomic potentials [153, 167]. The fcc and hcp crystals were used as reference structures for Ni and Re, respectively. The parameter α was used to fit the bulk modulus of the individual elements. The combinations of the partial electron densities, β_i, and the background electron densities, t_i, were used to fit the GSFE, elastic constants, surface energies, and tensile stress curves. The scaling parameters of the embedding function, A, and the parameter β_0 were used to fit the transitions energies of several stable and metastable crystal structures. The screening parameters, C_{min} and C_{max}, were used to correct the oscillations in the GSFE curves. The cutoff distance, r_c, the smoothing distance, Δr, and the parameter δ were used to fit the surface separation energy profiles.

For the binary system, the CsCl structure was used as reference. The nearest neighbour distance, $r_e(Ni, Re)$, and cohesive energy, $E_c(Ni, Re)$, were fixed to the DFT calculated values. The parameters $C_{min}(\mathrm{M}_i, \mathrm{M}_j, \mathrm{M}_k)$ and $C_{max}(\mathrm{M}_i, \mathrm{M}_j, \mathrm{M}_k)$, where $\mathrm{M}_{i,j,k}$ denotes Ni and/or Re, control the screening of the many body Ni-Re interactions and were used to fit the elastic constants of the CsCl structure as well as the Re substitutional and interstitial formation energies in fcc Ni.

The 2NN-MEAM potential parameters for Ni and Re and listed in Table 6.1 and these for the Ni-Re binary in Table 6.2.

TABLE 6.1: 2NN-MEAM potential parameter sets for Ni and Re. The units of E_c are eV, r_e, r_c, and Δr are Å. The reference structures for Ni and Re are fcc and hcp, respectively.

	E_c	r_e	β_0	β_1	β_2	β_3	α	A	C_{min}	t_1	t_2	t_3	C_{max}	r_c	Δr	δ
Ni	4.45	2.76	3.107	2.4	1.5	4.0	5.308	1.0	0.7	3.1	1.8	1.36	2.85	5.5	2.0	0.05
Re	8.03	2.49	4.5	2.40	7.285	4.0205	6.2402	0.74	0.45	5.60	3.5	-4.02	2.85	10.80	0.4	0.01

TABLE 6.2: 2NN-MEAM potential parameters set for the binary Ni-Re. The units of E_c are eV, r_e, r_c, and Δr are Å. The CsCl is used as a reference structure for NiRe.

parameters	values	parameters	values
$E_c(Ni, Re)$	6.165	$C_{min}(Ni, Ni, Re)$	2.10
$r_e(Ni, Re)$	2.555	$C_{max}(Ni, Re, Re)$	2.85
$\alpha(Ni, Re)$	5.85	$C_{min}(Ni, Re, Ni)$	0.70
Δr	2.0	$C_{min}(Ni, Re, Re)$	1.90
r_c	5.5	$C_{min}(Re, Re, Ni)$	1.90
$C_{max}(Ni, Re, Ni)$	3.0	$C_{max}(Re, Re, Ni)$	2.7
$C_{max}(Ni, Ni, Re)$	4.3		

TABLE 6.3: Properties of Ni calculated by P-MEAM potential, DFT, B-MEAM and EAM potentials, and experimental data. All properties are for Ni in fcc structure, unless otherwise stated. The cohesive energy of Ni in fcc, E_c, is in eV/atom. ΔE is in meV/atom and denotes the cohesive energy differences between the ground state fcc and higher energy crystalline phases. a is the lattice constant in Å and c/a is the ratio of lattice constants of the hcp structure. The unit of the bulk modulus is GPa. The units of the other properties are listed in the Table. Properties with an asterisk [$^{(*)}$] have been included in the materials' database and employed to fit the potential.

		P-MEAM	B-MEAM [155]	EAM [154]	DFT /Experimental
fcc Ni	$^{(*)}E_c$	-4.45	-4.45	-4.45	-4.842 [153] , -4.801
	$^{(*)}a$	3.521	3.521	3.52	3.524 [153], 3.52
	$^{(*)}$B	185	170	181	190.9 [153], 185
	B'	4.84	4.69	5.22	5.05
bcc	$^{(*)}\ \Delta E$	160	160	112	97, 93 [153]
	a	2.79	2.79	2.79	2.805
sc	ΔE	507	660	833	705
	a	2.32	2.35	2.35	2.33
hcp	ΔE	6.78	21	21	26 [153], 24
	a	2.49	2.49	2.48	2.488
	c/a	1.63	1.63	1.63	1.645
Elastic constant (GPa)	$^{(*)}C_{11}$	290	260	247	266 [153], 272
	$^{(*)}C_{12}$	161	150	148	155 [153], 155
	$^{(*)}C_{44}$	101	131	125	129 [153], 132
Vacancy formation energy (eV)	E_v	1.18	1.97	1.6	1.41 [153], 1.42
Surface energy (meV/Å^2)	$^{(*)}\gamma_{(100)}$	130	178	117	151 [176], 135
	$^{(*)}\gamma_{(110)}$	129	176	128	148 [176], 147
	$\gamma_{(111)}$	106	148	101	125 [176] 120
	$\gamma_{(112)}$	124	171	122	140

		P-MEAM	B-MEAM [155]	EAM [154]	DFT / Experimental
Cohesive strength (GPa)	$\sigma_{(100)}$	32	35	28	29
	$\sigma_{(110)}$	29	32	29	29
	$\sigma_{(111)}$	29	33	28	29
	$\sigma_{(112)}$	30	33	28	28
Critical Opening Displacement (Å)	$\delta_{(100)}$	0.56	0.57	0.56	0.5
	$\delta_{(110)}$	0.48	0.57	0.56	0.6
	$\delta_{(111)}$	0.48	0.48	0.48	0.45
	$\delta_{(112)}$	0.48	0.56	0.56	0.55
Work of Separation (meV/Å^2)	$^{(*)}w_{(100)}$	254	346	270	253
	$w_{(110)}$	253	341	286	279
	$w_{(111)}$	210	290	250	230
	$w_{(112)}$	246	335	282	267
Melting Temperature (K)	T_{Ni}	1550	2013	1635	1455 [177]

TABLE 6.4: Calculated physical properties of Re using the present 2NN MEAM potential as well as previous EAM potential compared to experimental and DFT data. All the properties are for hcp Re unless it is otherwise stated. The units are as in Table 6.3. The later applies also for the asterisk [$^{(*)}$].

		P-MEAM	EAM [167]	DFT /Experimental
hcp Re	$^{(*)}E_c$	-8.03	-8.03	-7.82, -8.03 [178]
	$^{(*)}a$	2.765	2.761	2.77
	c/a	1.623	1.614	1.615
	$^{(*)}$B	373	382	303
	B'	5.21	3.08	19
fcc	$^{(*)}\Delta E$	27.26	20.0	63
	$^{(*)}a$	3.91	3.90	2.58
bcc	ΔE	200	130	315
	a	3.10	3.05	3.11
sc	ΔE	1617	1944	1365
	a	2.60	2.63	2.58
Elastic constant (GPa)	$^{(*)}C_{11}$	609	611	613 [179]
	$^{(*)}C_{12}$	286	299	270 [179]
	$^{(*)}C_{44}$	124	159	163 [179]
	$^{(*)}C_{33}$	705	682	683 [179]
	$^{(*)}C_{13}$	208	234	206 [179]
Vacancy (eV)	E_v	3.22	3.49	3.27
Surface energy (meV/Å^2)	$^{(*)}\gamma_{(0001)}$	188	140	158
	$\gamma_{(10\bar{1}0)}$	194	151	184
	$\gamma_{(\bar{1}2\bar{1}0)}$	213	183	192

		P-MEAM	EAM [167]	DFT /Experimental
Cohesive strength (GPa)	$\sigma_{(0001)}$	48.17	57.27	38
	$\sigma_{(10\bar{1}0)}$	47.31	59.19	40
	$\sigma_{(\bar{1}12\bar{1}0)}$	45.83	59.36	38
Critical Opening Displacement (Å)	$\delta_{(0001)}$	0.45	0.33	0.55
	$\delta_{(10\bar{1}0)}$	0.47	0.34	0.5
	$\delta_{(\bar{1}2\bar{1}0)}$	0.53	0.39	0.6
Work of Separation (meV/$\mathring{A}^2$)	$^{(*)}w_{(0001)}$	367	318	333
	$w_{(10\bar{1}0)}$	377	344	361
	$w_{(\bar{1}2\bar{1}0)}$	407	397	387
Melting Temperature (K)	T_{Re}	4350	4836	3186 [177]

6.3.3 Structural and Elastic properties of Ni and Re

To parameterize and evaluate the interatomic potentials for Ni and Re, the structural, elastic, and point defect properties of these elements have been included in the material's database. Apart from the fcc and hcp ground states the crystal structures of bcc, and sc have been also considered. For Ni, the fcc and bcc phases were used to fit the potential whereas the sc and hcp phases to evaluate the potential. The Ni P-MEAM potential provides an excellent description of the lattice parameter, bulk modulus, and pressure derivative of bulk modulus when compared with DFT (see Table 6.3): The P-MEAM (DFT) calculated values of fcc lattice parameter, a, and bulk modulus, B, are 3.521 (3.52) Å and 185 (185) GPa, respectively. For hcp Re, the P-MEAM (DFT) calculated values of a, c/a, and B are 2.765 (2.77) Å, 1.623 (1.615), and 373 (303) GPa respectively. Nevertheless, apart from hcp Ni, the P-MEAM potential calculated equilibrium volumes are within less than 0.6 ^{3} in agreement with the DFT calculated values.

The P-MEAM calculated cohesive energy differences between the ground state and the higher energy crystal structures are in excellent qualitative agreement with the DFT calculated values. The ordering of the Ni cohesive energies is fcc<hcp <bcc < sc and for Re hcp< fcc < bcc < sc. In both cases, the left-sided structures are energetically more favorable than the right-sided.

The P- MEAM (DFT) calculated elastic constants of fcc Ni are C_{11}=290 (272), C_{12}=161 (148), and C_{44}=101 (125) GPa, respectively, i.e., there is an excellent agreement with the DFT calculations. The five independent elastic constants of hcp Re were also evaluated with P-MEAM and DFT. The P-MEAM calculated elastic constants are within 30% in agreement with the DFT calculated values (see Table 6.4). There is also an excellent agreement between P-MEAM and DFT calculated Ni and Re vacancy formation energies: The P-MEAM values for Ni and Re are 1.18 and 3.22 eV whereas the DFT values are 1.41and 3.27 eV, respectively. For these calculations, $4 \times 4 \times 4$ bulk supercells have been employed and the chemical potentials of Ni and Re were fixed to the chemical potential of bulk fcc Ni and hcp Re.

6.3.4 Generalized Stacking Fault Energies

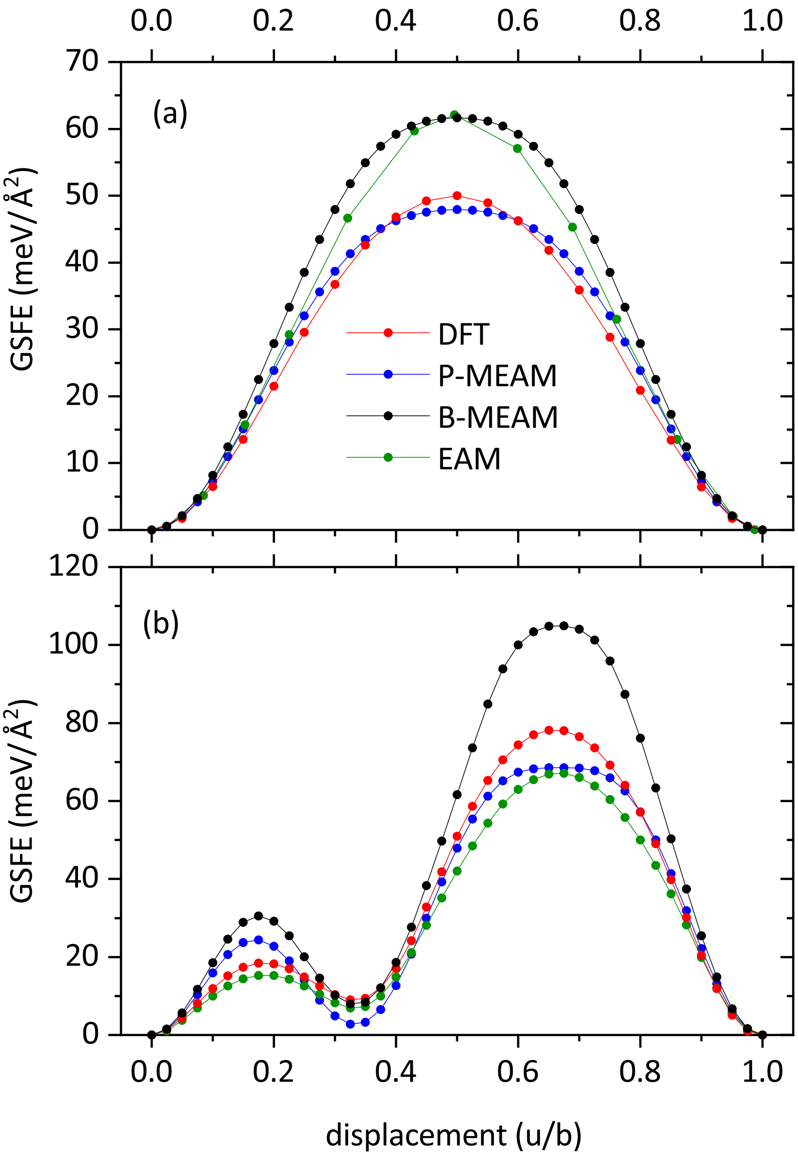

FIGURE 6.6: GSFE for Ni as function of normalized displacement along (a) $\langle\bar{1}10\rangle$ and (b) $\langle\bar{1}\bar{1}2\rangle$ shear directions in the $\{111\}$ plane obtained from DFT, P-MEAM, EAM [154] and B-MEAM [155] potential calculations.

A key material parameter that controls the dislocation emission is the unstable stacking fault energy (USFE). To calculate the unstable stacking fault energies for fcc Ni, we have calculated the GSFE for shear along $\langle 110\rangle$ and $\langle 112\rangle$ in the $\{111\}$ glide plane. The GSFE profiles calculated by P-MEAM and DFT as well as B-MEAM and EAM for the $\langle 110\rangle\{111\}$ and $\langle 112\rangle\{111\}$ systems are plotted in Figs. 6.6(a) and (b), respectively. The calculated USFE for the

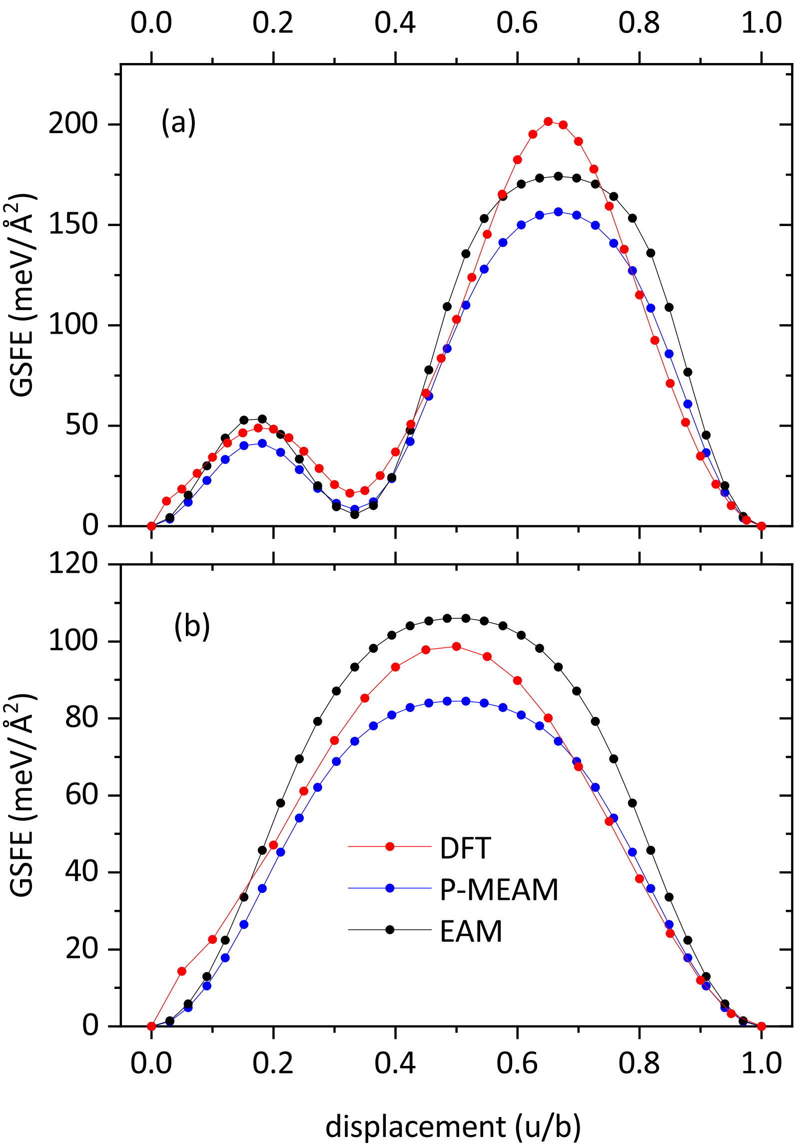

FIGURE 6.7: GSFE for Re as function of normalized displacement along (a) the $\langle\bar{1}2\bar{1}0\rangle$ shear directions in the basal plane and (b) the $\langle\bar{1}2\bar{1}0\rangle$ shear directions in the $\{10\bar{1}0\}$ plane obtained from P-MEAM, DFT, and EAM [167] potential calculations.

$\langle 110\rangle\{111\}$ slip system is at u/b reduced displacement, where u and b are the displacement and the norm of Burgers vector, respectively. The P-MEAM and DFT calculated values are 47.93 meV/Å^2 and 60.2 meV/Å^2, respectively. The P-MEAN calculated values of stable and unstable stacking fault energies for the $\langle 112\rangle\{111\}$ slip system are 2.74 and 24.38 meV/Å^2, respectively, whereas the DFT values are 9.3 and 16.8 meV/Å^2, respectively.

The GSFE profiles for Re calculated by P-MEAM, DFT, and EAM are plotted in Fig. 6.7(a) for shearing along $\langle\bar{1}2\bar{1}0\rangle$ in the basal plane and in Fig. 6.7(b) for the $\langle\bar{1}2\bar{1}0\rangle$ $\{10\bar{1}0\}$ slip system. The former was included in the material's database to fit the potential and the later to evaluate the transferability of the potential. The P-MEAM calculated values of USFE and SFE for the $\langle\bar{1}2\bar{1}0\rangle\{0001\}$ slip system are 41.28 and 8.31 meV/Å^2, respectively, whereas the DFT calculated values are 42.0 and 15.08 meV/Å^2, respectively. For the $\langle\bar{1}2\bar{1}0\rangle$ $\{10\bar{1}0\}$ slip system there is no stable stacking fault and the P-MEAM calculated USFE is 83.62 meV/Å^2 which compares well with the DFT calculated value of 68.69 meV/Å^2.

6.3.5 Surface Energies

The brittle fracture of materials is characterized by bond breaking and surface cleavage. Therefore, to perform an atomistic simulation of fracture, a prerequisite for the interatomic potentials is to correctly calculate surface energies. For Ni, we have considered the low index (100), (110), (111), and (112) surfaces and for Re the (0001), (1100), (1120) planes. The surface energy was calculated using slabs with 1 × 1 surface unit cell and 10 units along the normal direction to the surfaces. A 10 Å thick vacuum region was considered to decouple the two bounding surfaces of the slab. The surface energy E_{surf} is defined as:

$$E_{\mathrm{surf}} = \frac{1}{2A}\left(E_{\mathrm{slab}} - nE_{\mathrm{bulk}}\right) \qquad , \tag{6.10}$$

where E_{slab} is the total energy of the slab containing n atoms and two symmetry equivalent surfaces, E_{bulk} the bulk total energy per atom, and A is the area of the surface.

The calculated energies of Ni and Re surfaces are listed in Tables 6.3 and 6.4, respectively. The P-MEAM potential calculations predict, in excellent agreement with the DFT calculations, the following ordering of the surface energies for Ni: $\gamma_{\{111\}} < \gamma_{\{112\}} < \gamma_{\{110\}} < \gamma_{\{100\}}$. Moreover, the surface energy ordering of Re is in the same order as in DFT. For Re, both P-MEAM and DFT calculations agree qualitatively and the ordering of the surface energies is: $\gamma_{\{0001\}} < \gamma_{\{10\bar{1}0\}} < \gamma_{\{11\bar{2}0\}}$. Nevertheless, the Ni and Re surface energies are under- and over-estimated by P-MEAM with respect to the DFT calculated values, respectively.

6.3.6 Work of Separation

The work of separation has been calculated for the (100), (110), (111), and (112) Ni surfaces and for the (0001), (1100), and (1120) Re surfaces. The work of separation was calculated by employing the following two steps procedure. At first, a supercell was created consisting of a 1×1 unit cell and 10 unit cells along the surface normal. A vacuum of 10 angstrom was added to the cell. The cell is divided into two parts. The upper half of the crystal was rigidly shifted incrementally with a step size of 0.08 Å along the surface normal and the energy (U) was calculated at each step. The tensile stress σ is calculated as:

$$\sigma = \frac{1}{V(\varepsilon)} \frac{dU}{d\varepsilon} \quad . \tag{6.11}$$

Here, $V(\varepsilon)$ is the volume at strain ε. The maximum stress obtained from such a curve is known as the cohesive strength of the material and the separation distance at which the maximum stress occurs is the critical crack opening displacement, δ. The area enclosed under the curve is the work of separation, w (see Fig. 6.5).

Fig. 6.8 shows the tensile stress for Ni obtained by DFT, P-MEAM, B-MEAM [154], and EAM [155] potential calculations. As can be seen, the cohesive strength shows a weak dependence on the cleavage plane. The values of cohesive strength vary from 29-30 Pa. The P-MEAM predicted critical

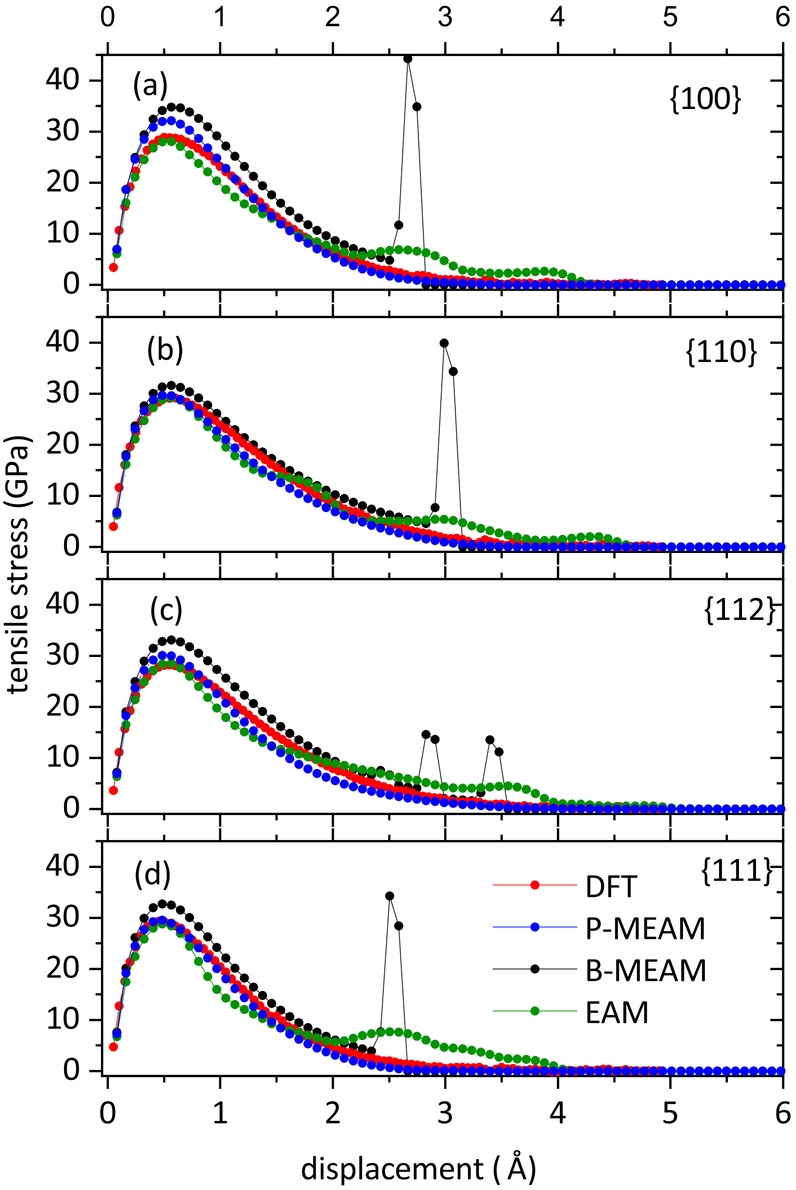

FIGURE 6.8: Traction separation of Ni as a function of separation distance. The DFT calculated curve for the (100) surface was used to fit the P-MEAM potential. The profiles of the other surfaces were used to evaluate the P-MEAM potential. EAM and B-MEAM are from Refs. [155] and [154] respectively.

opening displacements are in the range of 0.48-0.65 Å whereas the DFT obtained values vary from 0.60 to 0.66 Å. The work of separation is given in Table **??**. The DFT calculated values are in the range of 242-293 meV/Å^2 and the P-MEAM values in the range of 210-254 meV/Å^2.

As seen can be seen in Fig. 6.8, the EAM and B-MEAM potentials show spurious oscillations in the tail region of the tensile stress profiles. On the

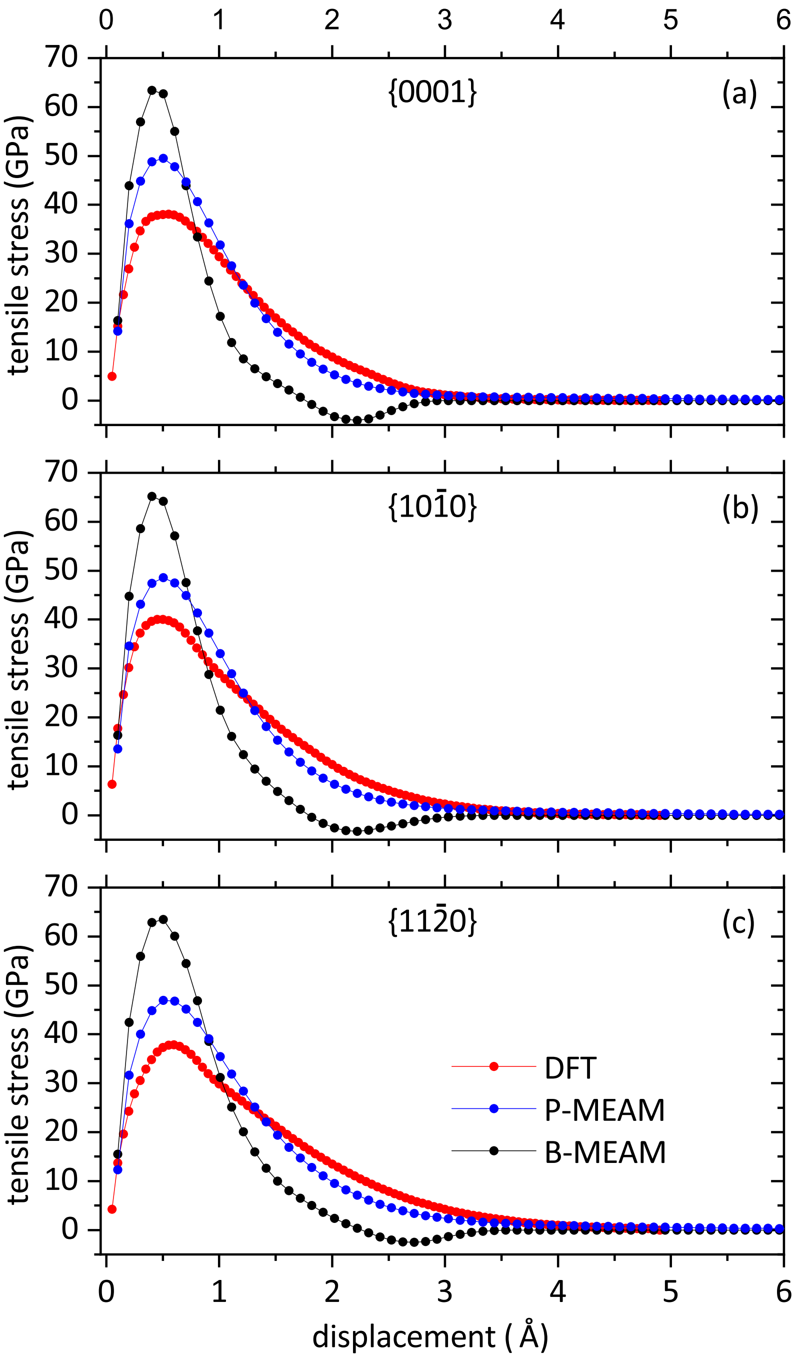

FIGURE 6.9: Traction separation of hcp Re as a function of separation distance. The DFT calculated curve for the (0001) plane was used to fit the P-MEAM potential. The profiles of the other surfaces were used to evaluate the P-MEAM potential. EAM potential is from Ref. [167].

other hand, DFT and P-MEAM potential calculations show a smooth decay of tensile stress with increasing separation distance. The above mentioned oscillations are attributed to the abrupt truncation of B-MEAM and EAM pair potentials at large separation distances [38, 46]. Ko *et al.* showed that such oscillations act as artificial barriers for the ductile-brittle transitions and are also responsible for the artificial crack blunting in fracture simulations [169].

Fig. 6.9 shows the tensile stress of Re for (0001), (1100), and (1120) surfaces obtained by the P-MEAM, EAM [167], and DFT calculations. The work of separations, cohesive strengths, and critical displacements calculated within the P-MEAM potential are in good quantitative and excellent qualitative agreement with the DFT values (see also Table 6.4). The P-MEAM calculated tensile stress profiles are in excellent qualitative agreement with the DFT calculations. On the other hand, the EAM potential shows artificial minima at separation distances larger than ≈2 Å.

6.3.7 Properties Ni-Re binaries

To fit and evaluate the potential selected properties of Ni-Re binary alloys have been calculated. These include the lattice and elastic constants, the cohesive energies, and mixing enthalpies. Moreover, the Re interstitial formation and binding energies of Re pairs at nearest neighbor distances have been also calculated. Specifically, the following crystal structures have been considered:

CsCl structure. This is used as the reference structure for the MEAM potential. The CsCl structure belongs to the Pm$\bar{3}$m space group and the primitive cell has two atoms, a Cs (Ni) atom at (0,0,0) and a Cl (Re) atom at $\left(\frac{1}{2},\frac{1}{2},\frac{1}{2}\right)$ in units of the primitive vectors (α,0,0), (0,α,0), and (0,0,α), where α is the lattice constant.

D1$_a$ structure. This structure belongs to the I4/m space group and has 5 atoms in the primitive cell. In units of the primitive vectors (α,0,0), (0,α,0), and $\left(\frac{\alpha}{2},\frac{\alpha}{2},\frac{c}{2}\right)$, where α and c are the lattice constants, the basis atoms are at: Re at (0,0,0) and Ni at $(+x,+y,0)$, $(-y,+x,0)$, $(-x,-y,0)$, and $(+y,-x,0)$, where x and y are internal lattice parameter. Therefore, the composition of this structure is Ni$_4$Re. This structure is the ground state of the binary at 20 at.% Re content [152].

TABLE 6.5: Strain configurations applied to calculate the elastic constants, C_{ij} of Ni-Re binaries in the tetragonal crystal structures. The strain configurations are in the form $\{\varepsilon_1, \varepsilon_2, \varepsilon_3, \varepsilon_4, \varepsilon_5, \varepsilon_6\}$. ε_i is the strain in Voigt notation. $\Delta E/V$ is the strain energy density and δ is the strain variable.

	Strain configuration	$\Delta E/V$
1	$\{2\delta, -\delta, -\delta, 0, 0, 0\}$	$\frac{1}{2}(C_{11} - 4C_{12} - 2C_{13} + C_{33})\,\delta^2$
2	$\{-\delta, -\delta, 2\delta, 0, 0, 0\}$	$(C_{11} + C_{12} - 4C_{13} + 2C_{33})\,\delta^2$
3	$\{\delta, \delta, 2\delta, 0, 0, 2\delta\}$	$(C_{11} + C_{12} - 4C_{13} + 2C_{33} + 2C_{66})\,\delta^2$
4	$\{\delta, 0, 0, 0, 0, 0\}$	$\frac{1}{2}C_{11}\delta^2$
5	$\{0, 0, \delta, 0, 0, 0\}$	$\frac{1}{2}C_{33}\delta^2$
6	$\{0, 0, 0, \delta, 0, 0\}$	$2C_{44}\,\delta^2$

$D0_{22}$ structure. This belongs to the tetragonal I4/mmm space group and the prototype is the Al_3Ti. The primitive vectors are the (α,0,0), (0,α,0), and $\left(\frac{\alpha}{2}, \frac{\alpha}{2}, \frac{c}{2}\right)$ and the four atoms in the primitive cell are at $(0,0,0)$ (Re), $\left(\frac{1}{2}, \frac{1}{2}, 0\right)$ (Ni), $\left(\frac{1}{4}, -\frac{1}{4}, \frac{1}{2}\right)$ (Ni), and $\left(-\frac{1}{4}, \frac{1}{4}, \frac{1}{2}\right)$ (Ni), in reduced coordinates.

Cu_3Au structure. The primitive vectors of this structure are the $(\alpha, 0, 0)$, $(0, \alpha, 0)$, and $(0, 0, \alpha)$, where α is the lattice constant. In the primitive cell, the 3 Ni atoms are at $\left(0, \frac{1}{2}, \frac{1}{2}\right)$, $\left(\frac{1}{2}, 0, \frac{1}{2}\right)$, and $\left(\frac{1}{2}, \frac{1}{2}, 0\right)$ and the Re atom at $(0,0,0)$ in reduced coordinates.

NaCl structure The rock salt structure belongs to the cubic Fm$\bar{3}m$ space group. The primitive vectors are the $\left(0, \frac{\alpha}{2}, \frac{\alpha}{2}\right)$, $\left(\frac{\alpha}{2}, 0, \frac{\alpha}{2}\right)$, and $\left(\frac{\alpha}{2}, \frac{\alpha}{2}, 0\right)$. The two basis atoms are at $(0,0,0)$ and $\left(\frac{1}{2}, \frac{1}{2}, \frac{1}{2}\right)$.

To calculate the bulk modulus and its pressure derivative the Murnaghan equation of state has been used [see Eq. (4.3)]. For the elastic tensors of the cubic phases, the strain configurations listed in Table 4.4 have been used. For the tetragonal phases, the strain configurations shown in Table 6.5 have been applied. Finally, the elastic constants were obtained by solving these linear systems of equations. The methodology was described in Section 4.4.1.

The Re substitutional, E^f_{sub} and interstitial, E^f_{inter} formation energies are written as:

$$E^f_{\text{sub or inter}} = E_{\text{tot}}(n) - nE^{\text{bulk}}_{\text{tot}} - \mu_{\text{Re}} \quad , \tag{6.12}$$

Here, $E_{\mathrm{tot}}(n)$ is the total energy of the Ni fcc supercell consisting of n atoms and an interstitial or substitutional Re, and $E_{\mathrm{tot}}^{\mathrm{bulk}}$ is the total energy per atom of fcc Ni. The chemical potential of Ni is therefore fixed to that of bulk Ni. μ_{Re} is the chemical potential of Re which is fixed to that of bulk Re in the hcp structure. The Re substitutional binding energy E_{bind} is calculated as follows:

$$E_{\mathrm{bind}} = E_{2\mathrm{sub}}^{f} - 2E_{\mathrm{sub}}^{f} \qquad , \tag{6.13}$$

where $E_{2\mathrm{sub}}^{f}$ is the formation energy of the substitutional pair. The mixing enthalpy is calculated as

$$\Delta H = E_{\mathrm{tot}}(\mathrm{Ni}_x\mathrm{Re}_y) - xE_{\mathrm{tot}}(\mathrm{Ni}) - yE_{\mathrm{tot}}(\mathrm{Re}) \tag{6.14}$$

where $E_{\mathrm{tot}}(\mathrm{Ni}_x\mathrm{Re}_y)$, $E_{\mathrm{tot}}(\mathrm{Ni})$, and $E_{\mathrm{tot}}(\mathrm{Re})$ are the total energies per atom of $\mathrm{Ni}_x\mathrm{Re}_y$, fcc Ni, and hcp Re, respectively. To calculate the Re interstitial, substitutional, and binding energies $4 \times 4 \times 4$ bulk fcc Ni supercells have been employed.

The calculated properties of $\mathrm{Ni}_x\mathrm{Re}_y$ by P-MEAM and DFT are listed in Table 6.7. As can be seen, the P-MEAM fitted cohesive energy and mixing enthalpy as well as the lattice constant and bulk modulus of NiRe in the CsCl structure are in excellent agreement with the DFT calculations. The mixing enthalpy is positive indicating that the formation of this phase is unstable at T=0 K. However, both P-MEAM and DFT calculate negative mixing enthalpy for the $\mathrm{Ni}_4\mathrm{Re}$ in $\mathrm{D1_a}$ structure. Nevertheless, all the P-MEAM calculated cohesive energies are in excellent agreement with the DFT values. Furthermore, both Re substitutional and interstitial

TABLE 6.6: Mechanical stability analysis of considered crystal structures as obtained from MEAM and DFT. s and u denote mechanically stable and unstable phases, respectively.

	MEAM	DFT
CsCl	u	u
Cu3Au	s	s
NaCl	s	u
d1a	s	s
I4-mmm	s	s

formation energies calculated with P-MEAM are positive and qualitatively agree with the DFT calculated values. However, while the DFT calculated binding energy of Re interstitials is negative, the P-MEAM predicted values are slightly positive. The P-MEAM calculated bulk modulus and its pressure derivative are within less than 20% in agreement with the DFT values, for all crystal structures considered.

Using the calculated elastic constants, the mechanical stability of the five different $Ni_{1-x}Re_x$ crystal structures can be addressed. A cubic crystal is said to be mechanically stable if the following conditions are met [180]:

$$C_{11} - C_{12} > 0 \tag{6.15}$$

$$C_{11} > 0, C_{44} > 0 \tag{6.16}$$

$$C_{11} + 2C_{12} > 0 \tag{6.17}$$

Both DFT and P-MEAM calculations predict mechanically stable crystal for the Cu_3Au structure and unstable for the CsCl. However, for NiRe in the NaCl structure, the DFT predicts $C_{44} < 0$, i.e., mechanically unstable, whereas P-MEAM $C_{44} > 0$, i.e., mechanically stable. Nevertheless, the P-MEAM calculated C_{44} is very low (10 GPa).

The mechanical stability conditions for tetragonal crystals are [180]

$$C_{11} - C_{12} > 0 \tag{6.18}$$

$$C_{11} > 0, C_{44} > 0, C_{33} > 0, C_{66} > 0 \tag{6.19}$$

$$C_{11} + C_{33} - 2C_{13} > 0 \tag{6.20}$$

$$2C_{11} + C_{33} + 2C_{12} + 4C_{13} > 0 \tag{6.21}$$

Both DFT and P-MEAM calculations predict D1a, and $D0_{22}$ structures to be mechanically stable. The results for the aforementioned crystal structures are summarized in Table 6.6.

TABLE 6.7: Calculated properties of the Ni-Re binary. The mixing enthalpies, ΔH_f are in eV/formula unit, the cohesive energies, E_c are given in eV/atom and the lattice parameters, a and c, in Å. The elastic constants are in GPa. Substitutional and interstitial formation energies and nearest neighbor substitutional binding energy are in eV. Properties with an asterisk [$^{(*)}$] are included in the materials' database.

	P-MEAM	DFT
CsCl NiRe (1:1)		
$^{(*)}E_c$	-6.165	-6.14
$^{(*)}a$	2.95	2.95
$^{(*)}$B	291	293
B´	5.14	4.78
$^{(*)}\Delta H_f$	0.15	0.67
$^{(*)}C_{11}$	193	186
$^{(*)}C_{12}$	342	354
$^{(*)}C_{44}$	250	144
D1a NiRe (4:1)		
E_c	-5.17	-5.73
a	5.53	5.67
c	3.91	3.58
B	243	249
B´	5.08	6.28
ΔH_f	-0.043	-0.29
C_{11}	409	359
C_{12}	147	165
C_{44}	123	161
C_{33}	457	338
C_{13}	154	201
$D0_{22}$ NiRe (3:1)		
E_c	-5.31	-5.73
a	3.64	3.56
c	7.30	7.38

	P-MEAM	DFT
B	273	285
B′	5.21	5.13
ΔH_f	0.14	0.11
C_{11}	363	328
C_{12}	250	248
C_{44}	255	157
C_{33}	401	365
C_{13}	207	192
Cu_3Au Ni_3Re		
E_c	-5.30	-5.61
a	3.64	3.63
B	274	227
B′	4.94	4.35
ΔH_f	0.17	0.77
C_{11}	395	239
C_{12}	215	196
C_{44}	221	113
NaCl NiRe (1:1)		
E_c	-5.58	-5.32
a	5.01	4.85
B	201	233
B′	5.01	4.72
ΔH_f	1.31	2.33
C_{11}	558	428
C_{12}	22	133
C_{44}	10	-54
$^{(*)}E_{\text{sub}}$	0.03	0.34
$^{(*)}E_{\text{inter/oct}}$	7.22	6.93
E_{binding}	0.05	-0.26

6.3.8 Melting Temperatures

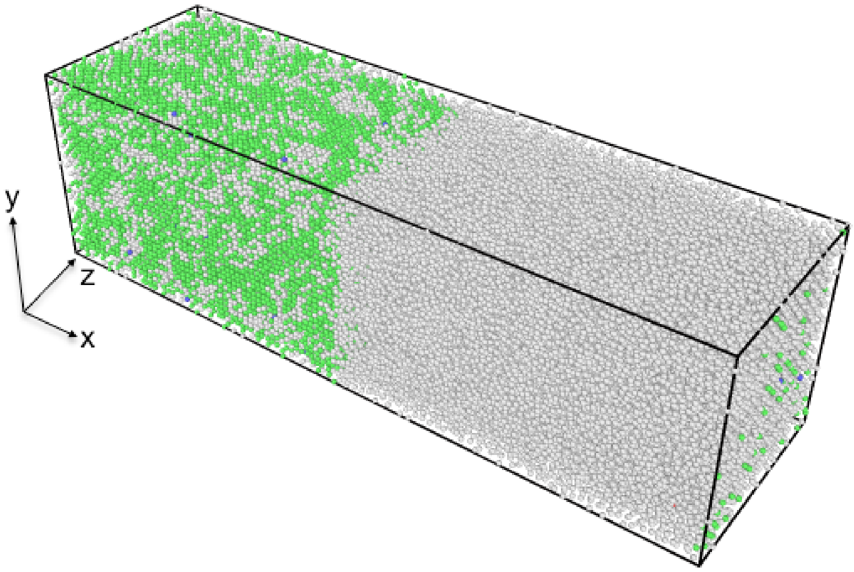

FIGURE 6.10: Solid-liquid interface model employed to calculate the melting temperature of Ni. The green atoms represent Ni in the solid phase whereas the white atoms Ni in the liquid phase.

Ni-Re superalloys are used in turbine blades of jet engines where they withstand extremely high temperatures. Therefore, it is of interest to calculate the melting temperature of Ni, Re, and Ni-Re using the present 2NN-MEAM potentials. To do so the moving interface method has been applied [181]: In the first step, a solid-liquid interface is created normal to the x direction of an orthogonal supercell with dimensions 200×70×70 Å, consisting of $\approx 5 \times 10^4$ atoms. This was achieved by melting half of the crystal under zero pressure while keeping the other half of the crystal in its crystalline state (see Fig. 6.10). Afterward, all the atoms are reassigned velocities equivalent to a temperature T_{guess} which is a guess of the actual melting temperature, T_m. All the atoms in the system are then equilibrated under zero pressure along the interface normal for a time of 50 ps using the isothermal-isobaric (NPT) ensemble. In the next step, the system is allowed to evolve for a further 20 ps within the canonical (NVT) ensemble. Then, the thermostat is turned off and the system is allowed to evolve within the micro-canonical (NVE) ensemble for 20 ps. If at the end of this procedure the current temperature is lower (higher) than the actual melting temperature, the interface moves towards the liquid (solid) phase, respectively.

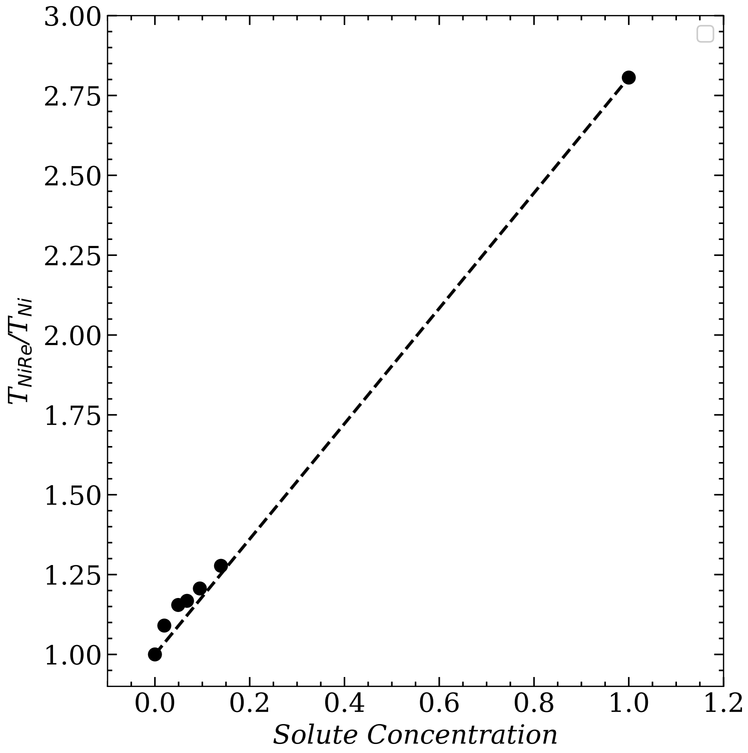

FIGURE 6.11: Melting point of $Ni_{1-x}Re_x$ alloy with respect to the melting temperature of pure Ni as a function of the Re content.

Using the above mentioned method the calculated melting temperatures for Ni and Re are 1550±10 K and 4350±20 K, respectively. These values are in good agreement when compared with the experimental values of 1455, 3186 K, respectively [177]. We further calculated the melting temperature of Ni-Re alloys. Substitutional Re was added randomly in the host matrix for different Re contents in the range of ≈2 - 14 at %. The calculated melting temperature of the Ni-Re with respect to that of Ni is plotted against the Re content in Fig. 6.11. As can be seen, within the aforementioned Re contents range, the melting temperature shows a monotonous increase with the content. Although an upward bowing can be seen at the low Re content region, this may be related to noise.

6.4 Results and Discussions

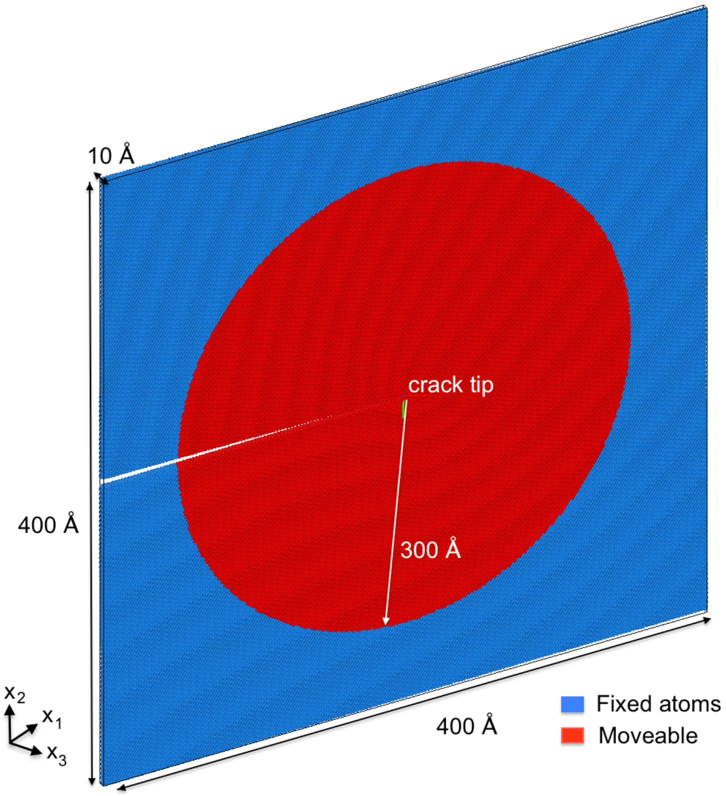

FIGURE 6.12: Schematic representation of the simulation cell employed to model crack propagation. The crack tip is placed at the origin. x_1 and x_2 are the crack propagation direction and the crack surface normal, respectively. The crack front direction is along x_3.

To perform large scale fracture simulations for the $\langle 112 \rangle \{111\}$ slip system, an atomically sharp crack has been introduced in a simulation cell using the isotropic displacement field of mode I fracture (see Fig. 6.12). The crack propagation direction, crack plane normal, and crack front are along x_1, x_2, and x_3 respectively. For an isotropic solid, the displacement field, $u = (u_1, u_2)$, for mode I fracture in plane strain condition is written as:

$$u_1 = \frac{\Delta K_I}{\mu} \sqrt{\frac{r}{2\pi}} cos\frac{\beta}{2}\left(1 - 2\nu + sin^2\frac{\beta}{2}\right) \tag{6.22}$$

$$u_2 = \frac{\Delta K_I}{\mu} \sqrt{\frac{r}{2\pi}} sin\frac{\beta}{2}\left(2 - 2\nu + cos^2\frac{\beta}{2}\right) \tag{6.23}$$

where

$$r = \sqrt{x_1^2 + x_2^2} \tag{6.24}$$

$$\beta = tan^{-1}\left(\frac{x_2}{x_1}\right) \quad . \tag{6.25}$$

μ and ν are the shear modulus and Poisson ratio, respectively. β is the angle between x_1 and x_2. ΔK_I is the increment in stress intensity factor.

The simulation cells consisted of $\approx 4 \times 10^5$ atoms and had the form of an orthogonal parallelepiped with edge length of $\approx$ 400 Å along x_1 and x_2, and $\approx$ 10 Å along x_3 (see Fig. 6.12). Periodic boundary conditions were applied along x_3. The crack was introduced by mapping the displacement field $\{u_1, u_2\}$ for mode I fracture in plane strain condition [see Eqns. (6.22)-(6.23)] on the atomic positions. The crack load was performed quasistatically: The atomic positions within an inner cylinder of radius $\approx$ 300 Å were relaxed while the atoms in the outer region were kept fixed. The atomic relaxation was performed until the change in the total energy was less than 10^{-8} eV or the forces on the atoms were lower than 10^{-12} eV/Å. After atomic relaxation, the stress intensity factor was increased by 0.005 MPa$\sqrt{\text{m}}$ and the displacement field was imposed on the relaxed structure. The quasistatic loading was continued until the stress intensity factor was 50% higher than the critical stress intensity factor predicted by LEFM.

To identify the angles between the slip and the crack planes and between the Burgers vector and the crack direction, the Thompson tetrahedron has been used. The Thompson tetrahedron describes all possible dissociations of dislocations in fcc crystals. Fig. 6.13 shows the four different $\{111\}$ planes, i.e., the $(\bar{1}\bar{1}1)$, (111), $(1\bar{1}\bar{1})$, and $(\bar{1}1\bar{1})$ planes denoted by the ABD, ABC, ADC,

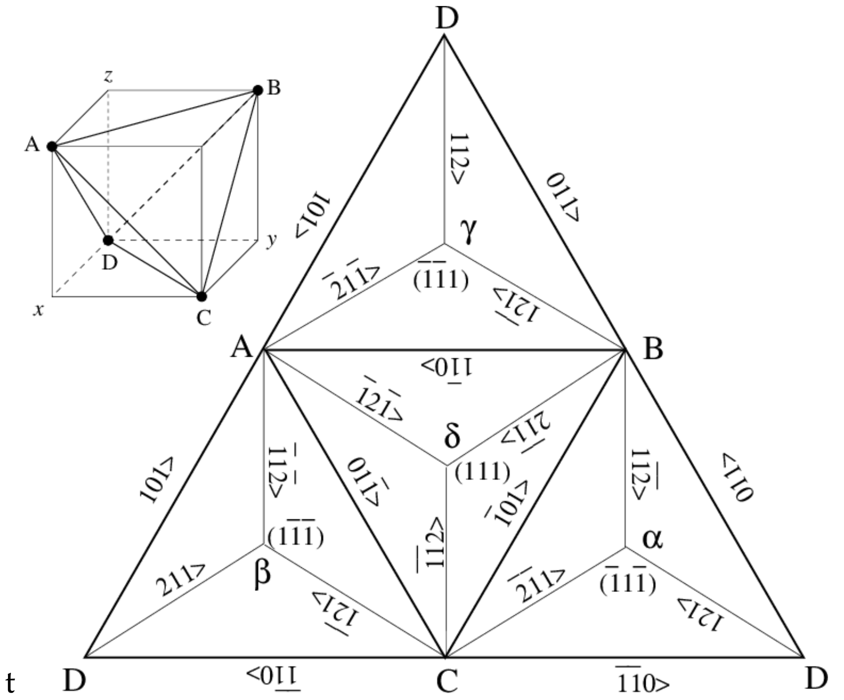

FIGURE 6.13: Schematic diagram of Thompson tetrahedron which contains all the slip systems of fcc and shows the Burgers vector of perfect and partial dislocations. Each side represents a slip plane, and the edge of the side represents the Burgers vector of a perfect dislocation.

and BCD triangles, respectively. The Shockley partial dislocations are confined in the $\{111\}$ planes whereas the perfect dislocations are given by the edges of the tetrahedron. For example, in the (111) plane, AB, BC, and CA correspond to perfect dislocations with Burgers of type $\frac{1}{2}\langle 110\rangle$. δA, δB, and δC represent the Shockley partial's Burgers vectors of type $\frac{1}{6}\langle 112\rangle$. In this slip plane, the dissociation of a perfect dislocation, AB, can be expressed in terms of the partial dislocations δA and δB. The dissociation is written as follows:

$$AB = A\delta + \delta B \tag{6.26}$$

In order to calculate the aforementioned angles, let us consider the following dissociation of a perfect dislocation with Burgers vector $\frac{1}{2}\langle 01\bar{1}\rangle$ into partial dislocations with Burgers vectors of type $\frac{1}{6}\langle 112\rangle$ in the (111) slip plane:

$$AB = A\delta + \delta B \tag{6.27}$$

$$\frac{1}{2}\langle 01\bar{1}\rangle = \frac{1}{6}\langle \bar{1}2\bar{1}\rangle + \frac{1}{6}\langle 11\bar{2}\rangle \tag{6.28}$$

All possible dissociations can be calculated similarly to the above reaction for all slip planes. Each plane contains three possible reactions. For example, The (111) slip plane can yield the three following reactions:

$$AB = A\delta + \delta B \tag{6.29}$$

$$AC = A\delta + \delta C \tag{6.30}$$

$$BC = B\delta + \delta C \tag{6.31}$$

Following all symmetry allowed dissociations described by Eqs. (6.29) the angles between the slip and the crack planes and the Burgers vector and the crack direction can be calculated.

TABLE 6.8: Critical stress intensity factors K_{Rice}, K_{Griffith}, and K_{CZM} obtained from LEFM using DFT and P-MEAM calculated unstable stacking fault and surface energies and works of separation, and K_{1c} obtained from atomistic simulations employing the P-MEAM potential for six different crack configurations in the $\langle 112 \rangle \{111\}$ slip system. The intensity factors are in MPa$\sqrt{\mathrm{m}}$. For each crack configuration, the angles θ and ϕ between the slip and the crack planes and between the crack front normal and the Burgers vector as well as the observed behavior, i.e., brittle or ductile, in atomistic simulations are also listed.

			DFT			MEAM				
Crack direction/ plane	θ	ϕ	K_{CZM}	K_{Griffith}	K_{Rice}	K_{CZM}	K_{Griffith}	K_{Rice}	K_{1c}	Observed behaviour
$[100]/(010)$	54.73	35.26	1.22	1.22	0.97	1.06	1.08	1.06	1.0	Brittle
$[1\bar{1}0]/(111)$	90	19.47	1.14	1.14	0.88	0.96	0.97	0.97	0.90	Brittle
$[1\bar{1}2]/(1\bar{1}\bar{1})$	61.87	19.47	1.14	1.14	0.82	0.96	0.97	0.91	0.91	Ductile
$[1\bar{1}0]/(\bar{1}\bar{1}2)$	90	0	1.23	1.23	0.84	1.04	1.05	0.93	1.0	Ductile
$[010]/(10\bar{1})$	54.73	30	1.25	1.25	0.92	1.06	1.07	1.01	0.9	Ductile
$[1\bar{1}0]/(001)$	90	144.73	1.22	1.22	0.99	1.06	1.08	1.08	1.0	Brittle

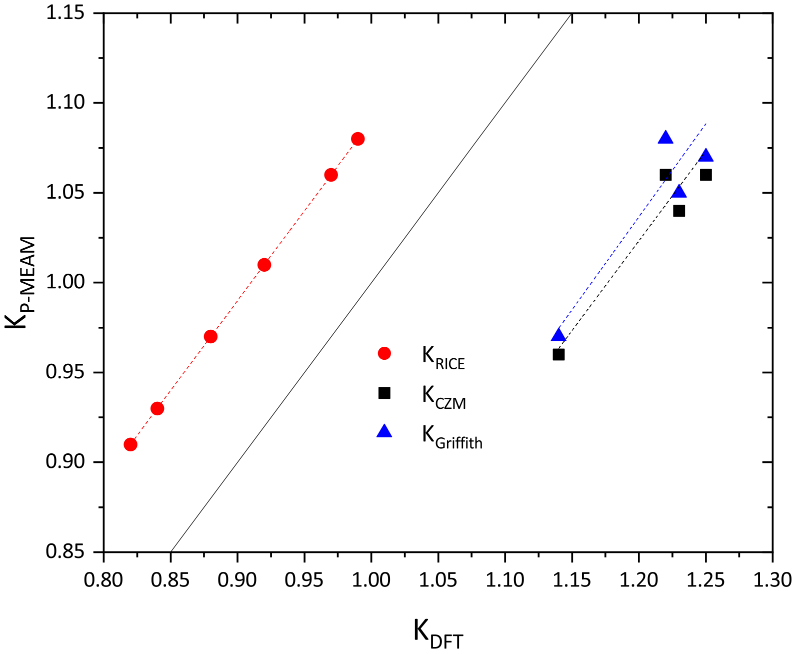

FIGURE 6.14: Critical stress intensity factors K_{Rice}, $K_{Griffith}$, and K_{CZM} in MPa$\sqrt{m}$ obtained from LEFM and P-MEAM calculated parameters plotted against those obtained from DFT calculated parameters. The solid black line indicates the ideal correlation between P-MEAM and DFT calculated values.

Table 6.8 lists the six different crack systems considered for the calculation of the stress intensity factor. In a first step, the stress intensity factors have been calculated using LEFM, i.e., the Griffith theory ($K_{Griffith}$), Rice theory (K_{Rice}), and cohesive zone modeling (K_{CZM}) (see Section 6.2). The stress intensity factors vary from 0.83 to 1.26 MPa$\sqrt{m}$ using DFT calculated values, and from 0.91 to 1.08 MPa$\sqrt{m}$ using P-MEAM calculated values. The differences in the value of K predicted by DFT and P-MEAM calculations arise from the differences in the calculated surface energies and unstable stacking fault energies.

The LEFM calculated values of the critical stress intensity factors using the P-MEAM calculated parameters are plotted against the DFT calculated ones in Fig. 6.14. There is a very good agreement between P-MEAM and DFT in the K_{Rice}. There is also a good agreement in the K_{Griffith} and K_{CZM} values, though the P-MEAM calculated values are underestimated with respect to

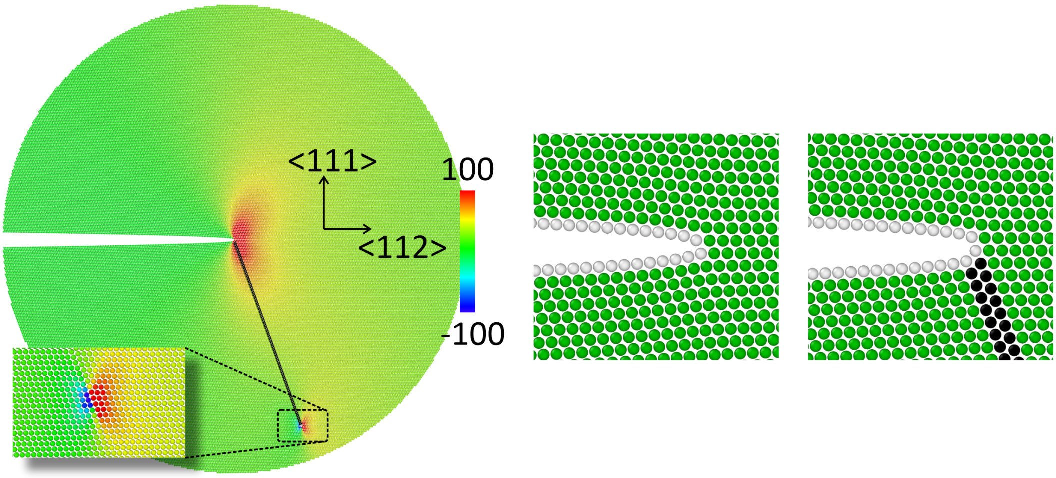

FIGURE 6.15: Left: σ_{yy} stress distribution (in GPa) in Mode I crack opening of the $\langle 112\rangle\{111\}$ crack system at K_{Ic}=0.91 MPa$\sqrt{\mathrm{m}}$. Inset: Zoom into the core of the emitted dislocation. Hot and cold colors represent tensile and compressive stress, respectively. Middle and right panels: Zoom into the crack region before and after and the nucleation and emission of the dislocation. The magnified atoms are colored according to their nearest neighbor coordination. Green and black atoms are in fcc and hcp bulk-like configurations, respectively. White balls represent surface atoms.

the DFT calculated ones. Nevertheless, both P-MEAM and DFT predict ductile fracture for the $[1\bar{1}2]$ / $(1\bar{1}\bar{1})$, $[1\bar{1}0]$ / $(\bar{1}\bar{1}2)$, and $[010]$ / $(10\bar{1})$ crack configurations, i.e., $K_{\mathrm{Griffith}} > K_{\mathrm{Rice}}$ and brittle for the $[100]$ / (010) configuration, i.e., $K_{\mathrm{Griffith}} < K_{\mathrm{Rice}}$. For the $[1\bar{1}0]$ / (111) and $[1\bar{1}0]$ / (001) configurations DFT predict brittle fracture, while P-MEAM calculates $K_{\mathrm{Griffith}} = K_{\mathrm{Rice}}$, i.e., a conclusion cannot be made. The atomistic calculations for these two systems predict brittle fracture, i.e., the crack tip propagates by cleavage instead of nucleation and emission of dislocations. The latter characterizes ductile fracture. Nevertheless, all the critical stress intensity factors calculated from P-MEAM based LEFM and atomistic fracture simulations agree within 10%. This small difference is attributed to the facts that (i) that the displacement field from isotropic elasticity theory has been applied and (ii) the tension-shear coupling and the surface tension have not been included in the calculations of the USFE.

To get insights into the large scale atomistic calculations let us focus on two crack systems with different fracture characters. We first discuss the

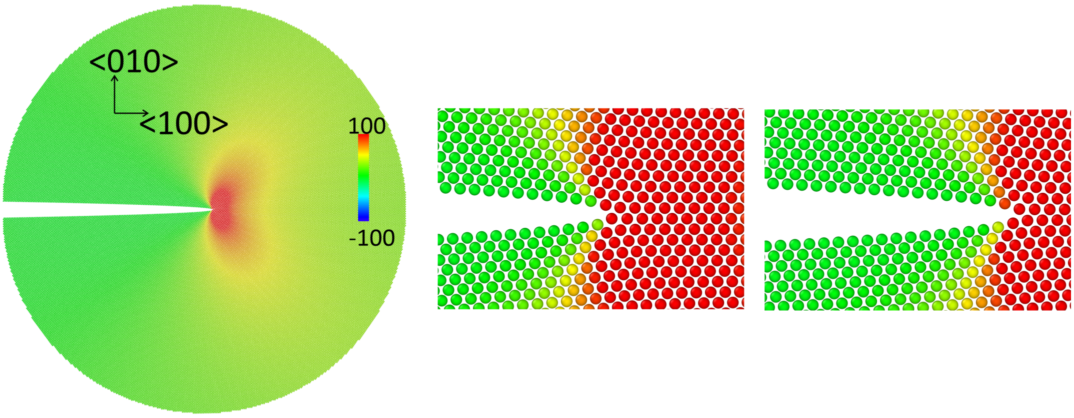

FIGURE 6.16: Left: σ_{yy} stress distribution (in GPa) around the [100] / (010) crack tip at K_{1c}=1 MPa$\sqrt{m}$. Middle and right panels: Zoom into the crack region before and after the crack propagation. Hot and cold colors represent tensile and compressive stress, respectively.

$[1\bar{1}2]$ / $(1\bar{1}\bar{1})$ system where the crack propagates via a dislocation nucleation and emission, i.e., it shows a ductile fracture. Fig. 6.15(left) shows the σ_{yy} stress distribution around the $[1\bar{1}2]$ / $(1\bar{1}\bar{1})$ crack tip at K_{Ic}=0.91 MPa$\sqrt{m}$. As can be seen, the crack tip propagation took place via the nucleation and emission of a Shockley partial with Burgers vector of type $b = a/6\langle 112\rangle$. Indeed the stress field shown in the inset is characteristic of an edge type dislocation. The glide away of the partial from the crack tip leaves behind a stacking fault (see black balls in the right panel of Fig. 6.15. A comparison of the atomic structure at the crack tip before [see Fig. 6.15(middle)] and after [see Fig. 6.15(right)] the propagation, demonstrates that the crack opening results in a blunted crack tip.

For the [100] / (010) crack system, brittle fracture is predicted (see Table 6.8). Fig. 6.16(left) demonstrates the σ_{yy} stress distribution around that crack tip at K_{1c}=1 MPa$\sqrt{m}$. Unlike the $[1\bar{1}2]$ / $(1\bar{1}\bar{1})$ system, the stress field does not indicate the presence of an edge type dislocation far from the crack tip. The propagation of the crack tip is depicted in Figs. 6.16(middle) and (left). The advancement of the crack is obtained by cleavage of the crack plane and the absence of any dislocation activity. Furthermore, as can be seen, the crack tip remains sharp. Therefore, fracture in this crack system is brittle.

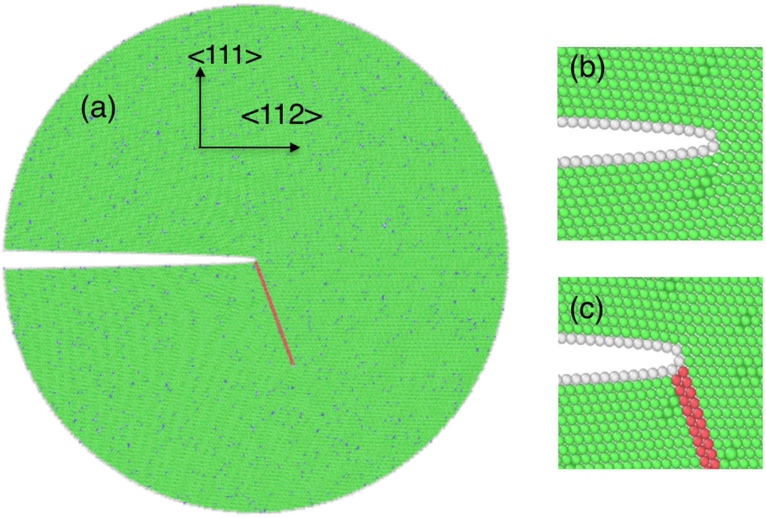

FIGURE 6.17: Left: Schematic representation of the atomic structure at the $[1\bar{1}2]$ / $(1\bar{1}\bar{1})$ crack system Crack tip in Ni with 0.6 at.% Re substitutionals at K_{1c}=0.87 MPa$\sqrt{\text{m}}$. Green and blue balls denote Ni and Re atoms, respectively. Red and white balls are atoms in hcp and at the surface, respectively. Middle and right: Zoom into the crack region before and after the nucleation and emission of the dislocation.

To investigate the effect of Re on the mechanical properties of Ni, Re solute is introduced in Ni. Since the $[1\bar{1}2]$ / $(1\bar{1}\bar{1})$ crack system has the lowest critical stress intensity factor, this system is selected to introduce Re solute. Re substitutional has been randomly distributed in the Ni host matrix by employing a random number generator with a uniform distribution. The atomic radius of Re is larger than that of host Ni. Therefore, the substitution of Re is expected to be favorable at the highly tensile stressed region around the crack tip (see stress distributions in Figs. 6.15 and 6.16). The solute content was varied from 0.5 at. % to 3.5 at. %, and for each concentration two random configurations have been constructed. The structures were then relaxed and the critical stress intensity factor was calculated using the same approach as for Ni.

The $[1\bar{1}2]$ / $(1\bar{1}\bar{1})$ crack system in Ni demonstrates ductile fracture (see Table 6.8). The addition of Re, within the 0.5 at.%-3.5 at.% range, does not alter the nature of fracture, i.e., fracture remains ductile. Indeed, the crack opening takes place via nucleation and emission of a Schottky partial [see the stacking in Fig. 6.17(left)]. Moreover, the crack opening results in a blunted crack tip [see Figs. 6.17(middle) and (right))].

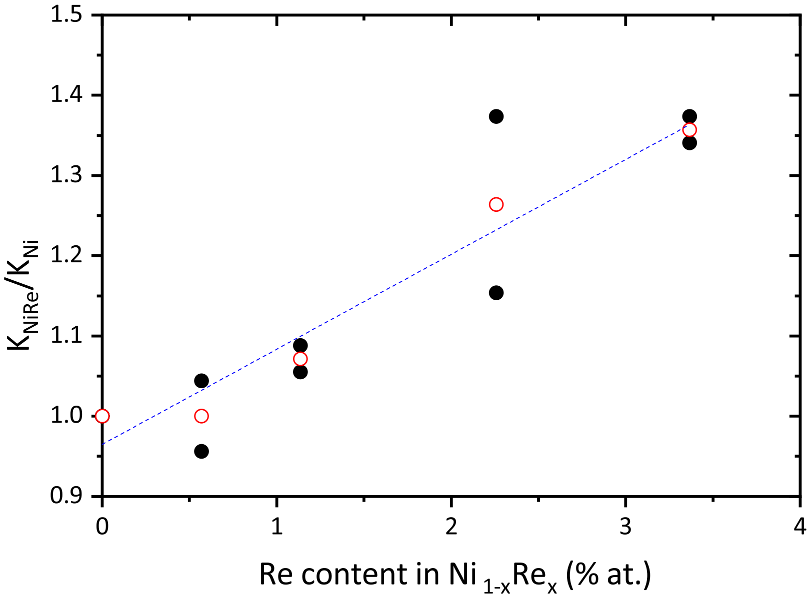

FIGURE 6.18: Ratio of critical stress intensity factor of $Ni_{1-x}Re_x$ (K_{NiRe}) to that of Ni (K_{Ni}) for mode I fracture in the $[1\bar{1}2]$ / $(1\bar{1}\bar{1})$ crack system plotted against the Re content. Filled and open balls indicate calculated and average values for each Re content. The dashed line is a linear fit to the average values.

Nevertheless, the addition of Re has a strong quantitative impact on the crack opening. The ratio of critical stress intensity of NiRe binary to that of Ni is plotted against Re content in Fig. 6.18. The critical stress intensity factor monotonously increases with the increase of Re content. For example at 3.5 at.% Re content, it is ≈35% larger than the critical value of Ni. This is consistent with the existing theoretical studies [~]breidi2016first and further validates the suitability of the P-MEAM potential for future studies of NiRe alloys.

6.5 Conclusions

In the present Chapter the effect of Re on the critical stress intensity factor of Ni has been investigated. In a first step, a detailed study to find suitable interatomic potentials for the unary Ni, Re, and binary $Ni_{1-x}Re_x$ systems has been conducted. The focus was given to the properties that correlate with fracture, such as surface energies, generalized stacking fault energies, tensile stress, and elastic constants. All the considered potentials for Ni and Re showed artificial oscillations or minima in the tensile stress curve at relatively large separation distances. These artificial oscillations result in artificial crack blunting in atomistic fracture simulations or overestimation of the critical strength. To address this, we have developed a new 2NN-MEAM Ni and Re potentials. Due to the scarcity of interatomic potentials to describe the Ni-Re interactions, an interatomic potential has also been developed for these interactions. During the parametrization of the potential, special care was taken to accurately describe properties that play dominant role in fracture such as surface energies, GSFE, works of separation, and traction separation profiles.

Using the newly developed potentials the critical stress intensity factors for mode I fracture in Ni has been calculated employing both LEFM and atomistic calculations. Six different crack configurations in the $\langle 112 \rangle \{111\}$ slip system have been considered. The lowest calculated value of K using LEFM was for the $[1\bar{1}2]$ / $(1\bar{1}\bar{1})$ configuration. For this crack system the $K_{\text{Rice}} < K_{\text{Griffith}}$, i.e., the fracture is ductile. This is also conformed by the large scale atomistic calculations which revealed that the crack opening proceeds through nucleation and emission of Shockley partial dislocations. The effect of Re on the fracture properties of Ni was further investigated. For Re contents in the range 0.5-3.5 at.%, the large scale atomistic calculations revealed that the nature of fracture does not change. However, the critical stress intensity factor increases, in agreement with the *rhenium effect*. The aforementioned indicate that the 2NN-MEAM Ni, Re, and Ni-Re potentials developed are suitable for large scale atomistic simulations of fracture in Ni and Ni-Re systems.

Chapter 7

Conclusions

The present thesis aimed to gather an on-atomic-scale understanding of the mechanisms governing grain boundary and line junctions reconstructions, segregation of impurities at these defects, and fracture mechanisms. A major challenge in these studies is that the underlying phenomena span a wide range of length scales. To address this, *ab-initio* calculations have been employed and 2NN-MEAM potentials for Si, C, Si-C, Ni, Re, and Ni-Re unary and binary systems have been developed and used in large scale atomistic calculations.

The work can be divided into three sections. The first part of the work was devoted to establishing the phase diagram of $\Sigma3$ GBs and GB line and facet junctions in Si. In the next part, the segregation of C at Si faceted GBs has been investigated. In the third part, linear elastic fracture mechanics and large scale fracture simulations of crack propagation have been conducted to study the effect of Re on the fracture toughness of Ni.

In the first step, a thorough investigation has been performed to screen available interatomic potentials in literature. The interatomic potentials were evaluated by calculating a wide range of material properties that influence GB and fracture properties. This evaluation revealed shortcomings in the description of some material properties such as the physically meaningless oscillatory profiles in the GSFE curves or unrealistically negative traction separation. However, these are key material properties strongly related to GBs and fracture. To address this, 2NN-MEAM potentials have been developed. Parametric studies that identify the relation between potential parameters and materials' properties have been applied and a code, "Potitr", to fit the potentials has been developed.

Using the newly developed 2NN-MEAM potentials, the phase diagram of $\Sigma3$ GBs in Si has been calculated. To calculate this diagram, both flat and faceted interfaces consisting of the low index and low energy {111} and {112} tilt facets have been considered. This diagram indicates that faceting is intrinsic to $\Sigma3$ GBs in Si. Furthermore, it demonstrates that GB faceting and facet and line junction reconstructions are strongly connected to the facet length and inclination angle, i.e., to geometric characteristics of the microstructure. Therefore, it highlights the crucial role of the microstructure on the GB and materials properties. This has important implications for the electronic properties mc-Si. Indeed, at small inclination angles with respect to the {111} plane, a symmetric {112} facet reconstruction that introduces deep states into the fundamental bandgap is stabilized. Nevertheless, the importance of the aforementioned phase diagram goes beyond the properties of GBs in Si. Specifically, it demonstrates that higher energy metastable GB reconstructions can be stabilized by thermodynamics and not kinetics when they constitute the facets at line junctions.

The emerged pattern from the aforementioned phase diagram of $\Sigma3$ GBs plays a crucial role in the segregation of impurities. Employing large scale simulations of C segregation at flat and faceted GBs in Si the mechanisms governing the experimentally observed asymmetric segregation of impurities at one of the two junctions at faceted GBs have been revealed. Using the calculated segregation energies, local concentrations of C solute were derived and compared to that of bulk. Our calculations revealed a site specific linear segregation at one facet junction core. This is a consequence of the complex topology and the strain field arising from the presence of partial edge dislocation at the line junctions.

Large scale atomistic calculations and linear elastic fracture mechanics have also been employed to study fracture in Ni and low Re content $Ni_{1-x}Re_x$ alloys. To achieve this, the newly Ni, Re, and Ni-Re developed 2NN-MEAM potentials have been used. Mode I fracture through crack propagation in the $\langle 112 \rangle / \{111\}$ fcc slip system has been considered. These calculations revealed that the crack system with the lowest critical intensity factor, i.e., the $[1\bar{1}2]/(1\bar{1}\bar{1})$, is ductile. Furthermore, they revealed that fracture remains ductile after the addition of a few at.% Re. However, in agreement with the rhenium strengthening effect, Re increases the critical intensity factor, i.e., the strength of the material.

In summary, in the present thesis, a method to systematically parametrize and evaluate MEAM interatomic potentials has been developed. Using the newly developed potentials, an on-atomic-scale understanding of phenomena related to interfaces and line defects as well as fractures has been gathered. The application of the potentials to investigate interfaces and fracture demonstrated the power of atomistic calculations to describe, understand and explain the underlying physics of complex phenomena.

Bibliography

(1) P. R. Cantwell, M. Tang, S. J. Dillon, J. Luo, G. S. Rohrer and M. P. Harmer, *Acta Materialia*, 2014, **62**, 1–48.

(2) R. W. Armstrong, *Materials Transactions*, 2014, **55**, 2–12.

(3) E. Hall, *Proceedings of the Physical Society. Section B*, 1951, **64**, 747.

(4) K. E. Aifantis and A. A. Konstantinidis, *Materials Science and Engineering: B*, 2009, **163**, 139–144.

(5) J. R. Rice and J.-S. Wang, *Materials Science and Engineering: A*, 1989, **107**, 23–40.

(6) M. A. Gibson and C. A. Schuh, *Acta Materialia*, 2015, **95**, 145–155.

(7) W Bludau, A Onton and W Heinke, *Journal of Applied Physics*, 1974, **45**, 1846–1848.

(8) L. Venema et al., *Nature*, 2011, **479**, 309–309.

(9) T. Kumano, T. Haratani and Y. Ushigami, *ISIJ international*, 2002, **42**, 440–448.

(10) R. A. Soref, *Proceedings of the IEEE*, 1993, **81**, 1687–1706.

(11) B. J. Skinner, *Proceedings of the national Academy of Sciences*, 1979, **76**, 4212–4217.

(12) M. A. Green, *Progress in Photovoltaics: Research and Applications*, 2009, **17**, 183–189.

(13) M. A. Green, *Solar energy*, 2003, **74**, 181–192.

(14) D. Sarti and R. Einhaus, *Solar energy materials and solar cells*, 2002, **72**, 27–40.

(15) A Shah, J Meier, A Buechel, U Kroll, J Steinhauser, F Meillaud, H Schade and D Dominé, *Thin solid films*, 2006, **502**, 292–299.

(16) C. H. Liebscher, A. Stoffers, M. Alam, L. Lymperakis, O. Cojocaru-Mirédin, B. Gault, J. Neugebauer, G. Dehm, C. Scheu and D. Raabe, *Physical review letters*, 2018, **121**, 015702.

(17) L. Liu, S. Nakano and K. Kakimoto, *Journal of Crystal Growth*, 2008, **310**, 2192–2197.

(18) A. Stoffers, O. Cojocaru-Mirédin, W. Seifert, S. Zaefferer, S. Riepe and D. Raabe, *Progress in Photovoltaics: Research and Applications*, 2015, **23**, 1742–1753.

(19) Y. Yang, A Yu, B Hsu, W. Hsu, A Yang and C. Lan, *Progress in Photovoltaics: Research and Applications*, 2015, **23**, 340–351.

(20) A. Peaker, V. Markevich, B Hamilton, G Parada, A Dudas, A Pap, E Don, B Lim, J Schmidt, L Yu et al., *physica status solidi (a)*, 2012, **209**, 1884–1893.

(21) B. Ziebarth, M. Mrovec, C. Elsässer and P. Gumbsch, *Physical Review B*, 2015, **91**, 035309.

(22) M. Huang and J. Zhu, *Rare Met.*, 2016, **35**, 127.

(23) M. Born and R. Oppenheimer, *Annalen der Physik*, 1927, **389**, 457–484.

(24) B. T. Sutcliffe and R. G. Woolley, *The Journal of chemical physics*, 2012, **137**, 22A544.

(25) R. M. Martin, *Electronic structure: basic theory and practical methods*, Cambridge university press, 2004.

(26) L. H. Thomas, Mathematical Proceedings of the Cambridge Philosophical Society, 1927, vol. 23, pp. 542–548.

(27) E. Fermi, *Rend. Accad. Naz. Lincei*, 1927, **6**, 32.

(28) W. Kohn and L. J. Sham, *Physical review*, 1965, **140**, A1133.

(29) P. A. Dirac, Mathematical Proceedings of the Cambridge Philosophical Society, 1930, vol. 26, pp. 376–385.

(30) J. P. Perdew and A. Zunger, *Phys. Rev. B*, 1981, **23**, 5048–5079.

(31) E. Wigner, *Phys. Rev.*, 1934, **46**, 1002–1011.

(32) J. P. Perdew, K. Burke and M. Ernzerhof, *Phys. Rev. Lett.*, 1996, **77**, 3865–3868.

(33) M. Fuchs, J. L. F. Da Silva, C. Stampfl, J. Neugebauer and M. Scheffler, *Phys. Rev. B*, 2002, **65**, 245212.

(34) J. Baker, M. Muir and J. Andzelm, *The Journal of chemical physics*, 1995, **102**, 2063–2079.

(35) L. Fan and T. Ziegler, *Journal of the American Chemical Society*, 1992, **114**, 10890–10897.

(36) P. E. Blöchl, *Physical Review B*, 1994, **50**, 17953.

(37) G. Kresse and D Joubert, *Physical Review B*, 1999, **59**, 1758.

(38) S. Groh and M. Alam, *Modelling and Simulation in Materials Science and Engineering*, 2015, **23**, 045008.

(39) M. Alam and S. Groh, *Journal of Physics and Chemistry of Solids*, 2015, **82**, 1–9.

(40) F. H. Stillinger and T. A. Weber, *Physical review B*, 1985, **31**, 5262.

(41) P. Erhart and K. Albe, *Physical Review B*, 2005, **71**, 035211.

(42) M. Baskes, *Physical Review B*, 1992, **46**, 2727.

(43) L. Lymperakis, Ph.D. Thesis, Paderborn University, 2005.

(44) K. Albe, K. Nordlund and R. S. Averback, *Phys. Rev. B*, 2002, **65**, 195124.

(45) Z Wu and W. Curtin, *Acta Materialia*, 2015, **88**, 1–12.

(46) Z Wu, M. Francis and W. Curtin, *Modelling and Simulation in Materials Science and Engineering*, 2015, **23**, 015004.

(47) S. Groh, *Journal of the mechanical behavior of biomedical materials*, 2015, **42**, 88–99.

(48) K. Kang and W. Cai, *International Journal of Plasticity*, 2010, **26**, 1387–1401.

(49) K. Kang and W. Cai, *Philosophical Magazine*, 2007, **87**, 2169–2189.

(50) M. S. Daw and M. I. Baskes, *Physical review letters*, 1983, **50**, 1285.

(51) M. S. Daw and M. I. Baskes, *Physical Review B*, 1984, **29**, 6443.

(52) B.-J. Lee and M. Baskes, *Physical Review B*, 2000, **62**, 8564.

(53) B.-J. Lee, M. Baskes, H. Kim and Y. K. Cho, *Physical Review B*, 2001, **64**, 184102.

(54) B. Jelinek, S. Groh, M. F. Horstemeyer, J. Houze, S.-G. Kim, G. J. Wagner, A. Moitra and M. I. Baskes, *Physical Review B*, 2012, **85**, 245102.

(55) J. H. Rose, J. R. Smith, F. Guinea and J. Ferrante, *Phys. Rev. B*, 1984, **29**, 2963–2969.

(56) M. Baskes, *Materials Chemistry and Physics*, 1997, **50**, 152–158.

(57) M. Alam, L. Lymperakis and J. Neugebauer, *Phys. Rev. Materials*, 2020, **4**, 083604.

(58) S. Ogata, J. Li and S. Yip, *Science*, 2002, **298**, 807–811.

(59) C.-Z. Wang, J. Li, K.-M. Ho and S. Yip, *Applied physics letters*, 2006, **89**, 051910.

(60) J. Crawford and P. Jacobs, *Journal of Solid State Chemistry*, 1999, **144**, 423–429.

(61) P. M. Anderson, J. P. Hirth and J. Lothe, *Theory of dislocations*, Cambridge University Press, 2017.

(62) V. Bulatov and W. Cai, *Computer simulations of dislocations*, Oxford University Press, 2006, vol. 3.

(63) A. H. Cottrell, *Progress in Metal Physics*, 1953, **4**, 205–264.

(64) A. P. Sutton, *Interfaces in crystalline materials*, Clarendon Press, 1995.

(65) C. Freysoldt, B. Grabowski, T. Hickel, J. Neugebauer, G. Kresse, A. Janotti and C. G. Van de Walle, *Reviews of modern physics*, 2014, **86**, 253.

(66) J. P. Hirth, *Metallurgical Transactions*, 1972, **3**, 3047–3067.

(67) L. Lymperakis, J. Neugebauer, M. Albrecht, T. Remmele and H. P. Strunk, *Phys. Rev. Lett.*, 2004, **93**, 196401.

(68) M. Reiche, M. Kittler, H. Übensee, E. Pippel, A. Haehnel and S. Birner, *Applied Physics A*, 2016, **122**, 389.

(69) P. Ebert, L Ivanova, S Borisova, H Eisele, A Laubsch and M Dähne, *Applied physics letters*, 2009, **94**, 062104.

(70) R. Fan, J. Magargee, P. Hu and J. Cao, *Materials Science and Engineering: A*, 2013, **574**, 218–225.

(71) O. Hunderi, *Physical Review B*, 1973, **7**, 3419.

(72) P. Lejček, S. Hofmann and A. Krajnikov, *Materials Science and Engineering: A*, 1997, **234**, 283–286.

(73) G. Duscher, M. F. Chisholm, U. Alber and M. Rühle, *Nature materials*, 2004, **3**, 621–626.

(74) L Lymperakis, M Friák and J Neugebauer, *The European Physical Journal Special Topics*, 2009, **177**, 41–57.

(75) T Buonassisi, A. Istratov, M. Pickett, M. Marcus, T. Ciszek and E. Weber, *Applied Physics Letters*, 2006, **89**, 042102.

(76) A. K. Da Silva, R. D. Kamachali, D. Ponge, B. Gault, J. Neugebauer and D. Raabe, *Acta Materialia*, 2019, **168**, 109–120.

(77) F. Nabarro, *Philosophical Magazine A*, 1997, **75**, 703–711.

(78) B Joos and M. Duesbery, *Physical Review Letters*, 1997, **78**, 266.

(79) Y. Tang, E. M. Bringa and M. A. Meyers, *Materials Science and Engineering: A*, 2013, **580**, 414–426.

(80) T. Buonassisi, O. F. Vyvenko, A. A. Istratov, E. R. Weber, G. Hahn, D. Sontag, J. P. Rakotoniaina, O. Breitenstein, J. Isenberg and R. Schindler, *Journal of Applied Physics*, 2004, **95**, 1556–1561.

(81) K. Scheerschmidt and M. Werner, *physica status solidi (a)*, 2005, **202**, 2368–2375.

(82) J. D. Murphy, R. McGuire, K Bothe, V. Voronkov and R. Falster, *Solar energy materials and solar cells*, 2014, **120**, 402–411.

(83) F. Schindler, A. Fell, R. Müller, J. Benick, A. Richter, F. Feldmann, P. Krenckel, S. Riepe, M. C. Schubert and S. W. Glunz, *Solar Energy Materials and Solar Cells*, 2018, **185**, 198–204.

(84) H Sawada and H Ichinose, *Scripta materialia*, 2001, **44**, 2327–2330.

(85) J. P. Hirth and J. Lothe, *Theory of dislocations*, John Wiley & Sons, 1982.

(86) W. T. Read and W Shockley, *Physical review*, 1950, **78**, 275.

(87) K. P. McKenna and A. L. Shluger, *Phys. Rev. B*, 2009, **79**, 224116.

(88) M. Guziewski, A. D. Banadaki, S. Patala and S. P. Coleman, *Computational Materials Science*, 2020, **182**, 109771.

(89) L. Lymperakis, H. Abu-Farsakh, O. Marquardt, T. Hickel and J. Neugebauer, *physica status solidi (b)*, 2011, **248**, 1837–1852.

(90) J. Tersoff, *Phys. Rev. B*, 1989, **39**, 5566–5568.

(91) B.-J. Lee and S.-H. Choi, *Modelling and Simulation in Materials Science and Engineering*, 2004, **12**, 621.

(92) N. Du, Y. Qi, P. E. Krajewski and A. F. Bower, *Metallurgical and Materials Transactions A*, 2011, **42**, 651–659.

(93) A. Seki, O. Hellman and S. Tanaka, *Scripta materialia*, 1996, **34**, 1867–1870.

(94) S. Ryu and W. Cai, *Modelling and Simulation in Materials Science and Engineering*, 2008, **16**, 085005.

(95) G. Kresse and J. Furthmüller, *Computational Materials Science*, 1996, **6**, 15–50.

(96) K. Jackson and M. R. Pederson, *Physical Review B*, 1990, **42**, 3276.

(97) J. P. Perdew, K. Burke and M. Ernzerhof, *Physical review letters*, 1996, **77**, 3865.

(98) S. Plimpton, *Journal of computational physics*, 1995, **117**, 1–19.

(99) A. I. Duff, L. Lymperakis and J. Neugebauer, *Phys. Rev. B*, 2014, **89**, 085307.

(100) B. Grabowski, T. Hickel and J. Neugebauer, *Phys. Rev. B*, 2007, **76**, 024309.

(101) D. C. Wallace, *American Journal of Physics*, 1972, **40**, 1718–1719.

(102) C. Herring, *Phys. Rev.*, 1951, **82**, 87–93.

(103) Y. Okada and Y. Tokumaru, *Journal of applied physics*, 1984, **56**, 314–320.

(104) T Soma and H. Kagaya, *Institution of Electrical Engineers, London, New York*, 1988, **33**.

(105) B.-J. Lee, M. Baskes, H. Kim and Y. Koo Cho, *Phys. Rev. B*, 2001, **64**, 184102.

(106) *NIST Interatomic Potentials Repository*, `http://www.ctcms.nist.gov/potentials`.

(107) L. Pastewka, A. Klemenz, P. Gumbsch and M. Moseler, *Physical Review B*, 2013, **87**, 205410.

(108) J. F. Justo, M. Z. Bazant, E. Kaxiras, V. Bulatov and S. Yip, *Physical review B*, 1998, **58**, 2539.

(109) W. M. Haynes, *CRC handbook of chemistry and physics*, CRC press, 2014.

(110) R. Jaccodine, *Journal of The Electrochemical Society*, 1963, **110**, 524–527.

(111) B. Farid and R. W. Godby, *Phys. Rev. B*, 1991, **43**, 14248–14250.

(112) B. Joós, Q. Ren and M. S. Duesbery, *Phys. Rev. B*, 1994, **50**, 5890–5898.

(113) V. V. Bulatov and E. Kaxiras, *Physical Review Letters*, 1997, **78**, 4221.

(114) G. Lu, N. Kioussis, V. V. Bulatov and E. Kaxiras, *Phys. Rev. B*, 2000, **62**, 3099–3108.

(115) J. A. Zimmerman, H. Gao and F. F. Abraham, *Modelling and Simulation in Materials Science and Engineering*, 2000, **8**, 103.

(116) S. Ryu, C. R. Weinberger, M. I. Baskes and W. Cai, *Modelling and Simulation in Materials Science and Engineering*, 2009, **17**, 075008.

(117) N. Sakaguchi, H. Ichinose and S. Watanabe, *Materials transactions*, 2007, **48**, 2585–2589.

(118) J. Hamilton, D. J. Siegel, I. Daruka and F. Léonard, *Physical review letters*, 2003, **90**, 246102.

(119) A. Rajabzadeh, F. Mompiou, S Lartigue-Korinek, N. Combe, M. Legros and D. Molodov, *Acta Materialia*, 2014, **77**, 223–235.

(120) S. Hofmann and P. Leiĉek, *Interface Science*, 1996, **3**, 241–267.

(121) J. Buban, K Matsunaga, J Chen, N Shibata, W. Ching, T Yamamoto and Y Ikuhara, *Science*, 2006, **311**, 212–215.

(122) S. Ma, K. M. Asl, C. Tansarawiput, P. R. Cantwell, M. Qi, M. P. Harmer and J. Luo, *Scripta Materialia*, 2012, **66**, 203–206.

(123) M. P. Harmer, *Science*, 2011, **332**, 182–183.

(124) X. Wu, Y.-W. You, X.-S. Kong, J.-L. Chen, G.-N. Luo, G.-H. Lu, C. Liu and Z. Wang, *Acta Materialia*, 2016, **120**, 315–326.

(125) A Kimura and H. Birnbaum, *Acta Metallurgica*, 1988, **36**, 757–766.

(126) K. Leitner, D. Scheiber, S. Jakob, S. Primig, H. Clemens, E. Povoden-Karadeniz and L. Romaner, *Materials & Design*, 2018, **142**, 36–43.

(127) J.-L. Maurice and C Colliex, *Applied physics letters*, 1989, **55**, 241–243.

(128) S. Joonwichien, I. Takahashi, K. Kutsukake and N. Usami, *Progress in Photovoltaics: Research and Applications*, 2016, **24**, 1615–1625.

(129) J. Schön, T. Niewelt, D. Mu, S. Maus, A. Wolf, J. D. Murphy and M. C. Schubert, *IEEE Journal of Photovoltaics*, 2021, **11**, 289–297.

(130) O. A. Al-Ani, J. Goss, N. Cowern, P. R. Briddon, M. Al-Hadidi, R. Al-Hamadany and M. Rayson, Solid State Phenomena, 2016, vol. 242, pp. 224–229.

(131) P. Käshammer and T. Sinno, *Journal of Applied Physics*, 2015, **118**, 095301.

(132) W. Kwapil, M. Kasemann, P. Gundel, M. C. Schubert, W. Warta, P. Bronsveld and G. Coletti, *Journal of Applied Physics*, 2009, **106**, 063530.

(133) L. Chen, X. Yu, P. Chen, P. Wang, X. Gu, J. Lu and D. Yang, *Solar energy materials and solar cells*, 2011, **95**, 3148–3151.

(134) D. Zhao and Y. Li, *Acta Materialia*, 2019, **168**, 52–62.

(135) G Kresse and J Furthmüller, *Phys. Rev. B*, 1996, **54**, 169.

(136) M. S. Daw and M. I. Baskes, *Phys. Rev. B*, 1984, **29**, 6443–6453.

(137) J. Furthmüller, J. Hafner and G. Kresse, *Phys. Rev. B*, 1994, **50**, 15606–15622.

(138) H. Matsunami, *Diamond and Related Materials*, 1993, **2**, 1043–1050.

(139) J. C. Newman Jr, *NASA STI/Recon Technical Report N*, 1992, **92**, 30964.

(140) M. Kuna, *Finite elements in fracture mechanics*, Springer, 2013, vol. 10.

(141) P. Andric and W. Curtin, *Journal of the Mechanics and Physics of Solids*, 2017, **106**, 315–337.

(142) J. R. Rice, *Journal of the Mechanics and Physics of Solids*, 1992, **40**, 239–271.

(143) J. R. Rice, *Journal of applied mechanics*, 1968, **35**, 379–386.

(144) K. B. Broberg, in *Cracks and Fracture*, ed. K. B. Broberg, Academic Press, San Diego, 1999, pp. 1–4.

(145) W. A. Curtin, *Journal of Materials Research*, 1990, **5**, 1549–1560.

(146) K. S. Cheung and S. Yip, *Physical review letters*, 1990, **65**, 2804.

(147) K. S. Cheung and S. Yip, *Modelling and Simulation in Materials Science and Engineering*, 1994, **2**, 865.

(148) N Bernstein and D. Hess, *Physical review letters*, 2003, **91**, 025501.

(149) N. Bernstein, J. R. Kermode and G. Csanyi, *Reports on Progress in Physics*, 2009, **72**, 026501.

(150) P. Caron and T. Khan, *Aerospace Science and Technology*, 1999, **3**, 513–523.

(151) P Caron, *Superalloys*, 2000, **2000**, 737–746.

(152) S. B. Maisel, N. Schindzielorz, A. Mottura, R. C. Reed and S. Müller, *Phys. Rev. B*, 2014, **90**, 094110.

(153) W.-S. Ko, B. Grabowski and J. Neugebauer, *Phys. Rev. B*, 2015, **92**, 134107.

(154) Y. Mishin, D. Farkas, M. J. Mehl and D. A. Papaconstantopoulos, *Phys. Rev. B*, 1999, **59**, 3393–3407.

(155) B.-J. Lee, J.-H. Shim and M. I. Baskes, *Phys. Rev. B*, 2003, **68**, 144112.

(156) S. A. Etesami and E. Asadi, *Journal of Physics and Chemistry of Solids*, 2018, **112**, 61–72.

(157) J. E. Angelo, N. R. Moody and M. I. Baskes, *Modelling and Simulation in Materials Science and Engineering*, 1995, **3**, 289.

(158) E. Bitzek, J. R. Kermode and P. Gumbsch, *International Journal of Fracture*, 2015, **191**, 13–30.

(159) P. Gumbsch and R. M. Cannon, *Mrs Bulletin*, 2000, **25**, 15–20.

(160) R Pérez and P Gumbsch, *Acta Materialia*, 2000, **48**, 4517–4530.

(161) R. Pérez and P. Gumbsch, *Physical review letters*, 2000, **84**, 5347.

(162) J. R. Kermode, A. Gleizer, G. Kovel, L. Pastewka, G. Csányi, D. Sherman and A. De Vita, *Physical review letters*, 2015, **115**, 135501.

(163) J. R. Kermode, Ph.D. Thesis, University of Cambridge, 2008.

(164) G. Csányi, T Albaret, G Moras, M. Payne and A. De Vita, *Journal of Physics: Condensed Matter*, 2005, **17**, R691.

(165) F. F. Abraham, R. Walkup, H. Gao, M. Duchaineau, T. D. De La Rubia and M. Seager, *Proceedings of the National Academy of Sciences*, 2002, **99**, 5777–5782.

(166) R. Ahmad, Z. Wu, S. Groh and W. Curtin, *Scripta Materialia*, 2018, **155**, 114–118.

(167) G Bonny, A Bakaev, D Terentyev and Y. A. Mastrikov, *Journal of Applied Physics*, 2017, **121**, 165107.

(168) M. Baskes and R. Johnson, *Modelling and Simulation in Materials Science and Engineering*, 1994, **2**, 147.

(169) W.-S. Ko and B.-J. Lee, *Philosophical Magazine*, 2014, **94**, 1745–1753.

(170) G. R. Irwin, *Journal of Applied Mechanics*, 1957, **24**, 361–4.

(171) J. H. Rose, J. Ferrante and J. R. Smith, *Physical Review Letters*, 1981, **47**, 675.

(172) J. H. Rose, J. R. Smith, F. Guinea and J. Ferrante, *Physical Review B*, 1984, **29**, 2963.

(173) A. Needleman, *Journal of Applied Mechanics*, 1987, **54**, 525–531.

(174) H. Cleveringa, E Van der Giessen and A Needleman, *Journal of the Mechanics and Physics of Solids*, 2000, **48**, 1133–1157.

(175) A. Stukowski, *Modelling and Simulation in Materials Science and Engineering*, 2009, **18**, 015012.

(176) L. Vitos, A. Ruban, H. L. Skriver and J Kollar, *Surface science*, 1998, **411**, 186–202.

(177) H. Okamoto, *Journal of Phase Equilibria and Diffusion*, 2012, **33**, 346–346.

(178) C. Kittel, P. McEuen and P. McEuen, *Introduction to solid state physics*, Wiley New York, 1996, vol. 8.

(179) M. de Jong, D. L. Olmsted, A. van de Walle and M. Asta, *Physical Review B*, 2012, **86**, 224101.

(180) O. Beckstein, J. Klepeis, G. Hart and O Pankratov, *Physical Review B*, 2001, **63**, 134112.

(181) J. R. Morris, C. Z. Wang, K. M. Ho and C. T. Chan, *Phys. Rev. B*, 1994, **49**, 3109–3115.